

Computational Mechanics of Fracture and Fatigue in Composite Laminates by Means of XFEM and CZM



The
University
Of
Sheffield.

Behrooz Tafazzolimoghaddam
Department of Mechanical Engineering
University of Sheffield

A thesis submitted for the degree of
Doctor of Philosophy

October 2017

Declaration

I, Behrooz Tafazzolimoghaddam, declare that I have produced this thesis entitled, "Computational Mechanics of Fracture and Fatigue in Composite Laminates by Means of XFEM and CZM" without the assistance of third parties and without making use of aids other than those specified. The thesis work was conducted from November 2013 to November 2017 under the supervision of Dr. José Luis Curiel-Sosa at the University of Sheffield.

Sheffield, October 2017

Acknowledgements

Completion of this project would not have been possible without guidance and help of many people who always offered their priceless support and help. I would like to thank my supervisor Dr. José Luis Curiel-Sosa for accepting me as his PhD student and for his excellent support throughout the study in one of the best universities in the world. This university has earned its reputation thanks to the hard working and lovely staff whom I would like to express my great appreciation for their support. Sincere thanks to Mr. Joseph Ibbett for his collaboration in this study. Special thanks to my family, my mother Akhtar, my brother Esmaeil and my sister Afsaneh for their support and patience during all these years of studying. At the end, I would like to acknowledge my late father Abbas whom without his support none of the achievement I had would have been possible. His memory will always be with me.

Abstract

This thesis is on the computational fracture analysis of static and fatigue fracture in advanced composite materials using Extended Finite Element Method (XFEM). Both in analytical and numerical approaches, the techniques and procedures need adjustments to take account for numerous effects brought by the heterogeneous and orthotropic nature of the advanced composite materials. The first part of this study is on the calculation of Energy Release Rate (ERR) for cracks in composite structures. J-Integrals are widely used in computational methods for the ERR evaluation however, they do not show consistency in structured materials when the crack is close to the material interfaces. Furthermore, when J-Integrals are implemented in XFEM, the enrichment functions of the crack-tip and the interfaces create even more complications. The outcome of the first study clarified that the linear elastic fracture mechanic (LEFM) approach on its own suffers from the effects caused by the crack-tip singularity and the stress field definition at the crack-tip. Cohesive Zone Model (CZM) is selected as an alternative to prevent some of the complications caused by the material heterogeneity and the singularity at the crack-tip. In-spite CZM is a damage based approach, it can be linked to the LEFM which is particularly useful for fatigue modelling.

In the second part, the implementation of CZM in XFEM for quasi-static and fatigue modelling is presented. Unlike previous FE implementations of CZM [14, 136], the current approach does not include the undamaged material in the traction separation law to avoid enriching undamaged elements. For the high-cyclic fatigue model, a thermodynamically consistent approach links the Paris law crack growth rate to the damage evolution. A new numerical approach is proposed for the implementation of the CZM for quasi-static and fatigue fracture modelling in XFEM. The outcomes

are then compared to the results of other experimental and numerical studies. The fatigue test results comply to the Paris law predictions however, linking Paris law with the damage evolution in the cohesive zone is prone to produce errors since different parts of the cohesive zone undergo different degradation rates.

Contents

1	Introduction	1
1.1	Motivations	1
1.2	Aims and Objectives	4
1.3	Fibre Reinforced Composites	5
1.4	Mechanics of Composite Materials	5
1.5	Fracture of composite structures	8
1.6	Failure analysis of materials: Theoretical background	9
1.6.1	Continuous Approaches: Damage Mechanics Approach for Cohesive Zone Model	10
1.6.2	Discontinuous approaches (Fracture Mechanics)	11
1.7	Computational methods for failure analysis	14
1.7.1	Boundary Element Method (BEM)	14
1.7.2	Meshless Methods	15
1.7.3	Finite Element Method (FEM)	15
1.7.4	Enriched approximations	15
1.7.4.1	Space Discretization and Enrichment Functions	18
1.7.4.2	Fatigue Modelling in XFEM	20
1.8	Current State of the Art and Proposed Research on Composite Fatigue Fracture Modelling	22
1.9	Outline of the project	23
1.10	Conclusion	24
2	Energy release rates calculation for transversal crack in standard FEM and XFEM	27
2.1	Introduction	27

2.2	Background	27
2.2.1	Virtual Crack Closure Technique (VCCT)	28
2.2.2	J-Integrals	30
2.2.3	Mixed mode J-Integrals	32
2.3	Material and geometries	34
2.4	FEM analysis of the problem (ABAQUS)	35
2.5	Three dimensional analysis for generalized plane strain in FEM	37
2.6	XFEM analysis of the problem	41
2.6.1	Problem formulation and discretization	42
2.6.2	Selection of the nodes to enrich	44
2.6.3	Results of XFEM analysis	44
2.7	The crack-tip asymptotic field effect	45
2.8	Conclusion	47
3	Cohesive zone model for delamination analysis in XFEM	49
3.1	Introduction	49
3.2	Background	50
3.3	Energy balance in CZ	51
3.4	CZM for mixed mode delamination	53
3.4.1	Constitutive Law for the CZ	54
3.4.2	Governing equations of a cracked body and variational formulation	58
3.4.2.1	Discretization	58
3.4.3	Crack propagation and growth direction criterion	62
3.5	Numerical implementation	63
3.5.1	Integration scheme	66
3.5.2	On the nodal cohesive force implementation	69
3.5.3	Energy release rate calculation for the cohesive zone	70
3.6	Numerical tests and the results	71
3.6.1	Mode I test and the cohesive zone length	72
3.6.2	Mode II test	76
3.6.3	Mixed mode case	78

3.6.4	Simulation of double cantilever beam delamination (displacement-controlled)	79
3.7	Conclusion	84
4	Cyclic cohesive zone model in XFEM for high-cyclic delamination simulation	85
4.1	Introduction	85
4.2	Background	85
4.3	Cohesive Zone Model	87
4.3.1	Cyclic damage law	88
4.4	Numerical Implementation	89
4.5	Tests	90
4.6	Results	92
4.7	Conclusion	99
5	Conclusion	101
5.1	Contributions	101
5.2	Conclusions	102
5.3	Suggestions for future studies	104
A	Simulation of microcracks in 3D printed parts built by selective laser sintering (SLS) using XFEM	107
A.1	introduction	107
A.2	Background	107
A.2.1	Degree of Particle Melt (DPM)	108
A.2.2	Part orientation factor	108
A.3	Numerical implementation	109
A.4	Tests	109
A.4.1	The effect of inclusion proximity on the crack behaviour	109
A.4.2	The crack behaviour between two adjacent inclusions	112
A.4.3	Simulation of the cross section of SLS print	113
A.5	Conclusion	115
	Bibliography	118

List of Figures

1.1	Two major cracking modes in composites are transversal cracks and delamination	3
1.2	Continuous unidirectional (left) versus chopped fibre reinforcement. . .	5
1.3	The fibres are aligned with the first local axis	7
1.4	Unidirectional FRCs are transversely isotropic	8
1.5	Damage distribution in fibrous composites. Fibre bridging in brittle composites (left), interface debonding propagation and finally fibre breakage (right)	9
1.6	Infinite plate with centre crack of length $2a$ under uniform traction . .	12
1.7	Different modes of crack opening displacement	12
1.8	J- Integrals can be calculated on any closed path around the crack tip	13
1.9	Quarter point element at the crack-tip	16
1.10	Level set method defines a complex geometry by intersecting a plane with a known volume	17
1.11	The value of Φ and Ψ at every node (and Gauss point) will define their location regarding the discontinuity	18
2.1	Crack Closure Technique uses forces from first step solution (left) and the displacement calculated after the crack extension (right) in the second step at node i	29
2.2	Virtual Crack Closure Technique uses forces from the crack tip node i and the displacements from node k	30
2.3	Contour integral in a two dimensional cracked body	30
2.4	Contour integral in a two dimensional cracked body	32
2.5	Transverse crack in $[0/90]_s$ laminate	35
2.6	Boundary conditions	36

2.7	Several J-integrals were used around the crack tip for ERR calculation	37
2.8	J-integral result from 3D FEM solver under $\epsilon_{33} = -0.000381$	38
2.9	The mesh near the interface has to be refined in order to create enough elements in the 90° ply such that the J-Integral path does not enter the 0° ply	38
2.10	σ_x and σ_y distribution for $a = 0.50\text{ mm}$	39
2.11	Normal stress at the interface for $L = 2\text{ mm}$.	40
2.12	Normal stress at the interface ahead of the crack for $L = 2\text{ mm}$ (zoom)	40
2.13	J-integral result from XFEM solver and BEM results	41
2.14	A body in equilibrium state	42
2.15	Comparison of results from ABAQUS and MATLAB XFEM code. Element length for XFEM cases were 0.01mm (55 elements in thickness direction of each ply)	45
2.16	Variation of the J-integral due change in the location of the mid-side node. The contours are depicted in Fig. 2.7	46
3.1	Hillerborg cohesive zone model	50
3.2	Cohesive zone models take variety of shapes.	51
3.3	Cohesive zones with no undamaged zone. This model only applies to the material that has entered the degradation process. (left) and model with undamaged zone before yielding at λ_y (right). The material acts elastically in the region between zero and λ_y	52
3.4	The restoration of the cohesive force as a result of changing loading mode.	53
3.5	Local crack coordinate. Φ defines whether the material is before normal to the crack tip or after.	55
3.6	Softening law for the cohesive forces	56
3.7	The equivalent mixed mode traction-separation law	57
3.8	Body Ω containing discontinuity Γ_c	59
3.9	Flowchart for the quasi-static solver for the load controlled test under applied moment-load M . The solver finds the equilibrium state at which the numerical crack-tip stress is equal τ_0 .	65

3.10	The triangulation of the enriched elements and the modification of the shape functions to count for the crack location in the element(right) .	66
3.11	Construction of the N_3 shape function for the third node (top left node) of the crack-tip element. Υ is the discontinuous function for crack opening	68
3.12	The modified displacement field shape function (left) and a displacement field for a trial nodal displacement applied at nodes (right) . . .	68
3.13	The stress distribution before (left) and after crack-tip enrichment correction. In this example, the cohesive zone is not fully developed and the traction at the physical crack-tip is non-zero.	69
3.14	Moments M are used to create constant (G) for all crack lengths . . .	72
3.15	Damage distribution along crack line in the fully developed cohesive zone. There are 16 element in the cohesive zone and $l_e = 0.0526\text{ mm}$.	73
3.16	Normal stress evolution in the cohesive zone	75
3.18	σ_y distribution under mode I opening load at $G_I = G_{Ic} = 0.26\text{kJ/m}^2$ and initial $a = 4\text{ mm}$ for HTA6376/C, thickness=3.1 mm	75
3.17	Full cohesive zone under mode I opening load at $G_I = G_{max} = 0.26\text{ kJ/m}^2$. The length of the cohesive zone is approximately 0.87 mm.	76
3.19	Crack opening deformation for full cohesive zone	76
3.20	Crack opening deformation for $l_e = 1/17\text{ mm}$	77
3.21	$G_{II} = 0.754\text{ kJ/m}^2$ and $l_e = 1/17\text{ mm}$	77
3.22	σ_{xy} for DCB $G_{II} = 1.07\text{ kJ/m}^2$ (J-Integral) and $l_e = 1/19\text{ mm}$ and $l_{cz} = 5.2\text{ mm}$	77
3.23	σ_{xy} at $G = 0.1\text{kJ/m}^2$ load and $l_e = 1/21\text{mm}$	78
3.24	Deformation for 50% mixed model loading. The results are exaggerated.	78
3.25	σ_{xx} for $G = 0.1\text{kJ/m}^2$ and $l_e = 1/21\text{mm}$	79
3.26	Double Cantilever Beam specimen.	80
3.27	Stress distribution of the delamination crack in DCB specimen for intense mesh $l_e = 0.0909\text{ mm}$	81
3.28	The load displacement test results for different mesh sizes. The experimental results are from Turon et al. [137]	82
3.29	Crack opening for DCB test with high intensity mesh	83

4.1	Envelope load model considers an equivalent static load over a known period of time for each time step of the quasi-static solution	87
4.2	The flowchart for high-cyclic fatigue solver. This code is run after the quasi-static solver has converged initially so that the ERR and cohesive zone length are known for the load M. Here an energetic criterion is used rather than stress at the crack-tip.	91
4.3	Mode I damage plots for 400 cycles with 10 cycles envelope loading. Applied load $G_I = 0.14kJ/m^2 = 0.538G_c$ and $l_e = 1/17mm$ mesh size. The crack has grown 7 elements which is 0.001029mm for each cycle.	93
4.4	Mode I cohesive forces plots for loading $G_I = 0.14kJ/m^2 = 0.538G_c$ and for $l_e = 1/17mm$ mesh size.	94
4.5	Mode I crack growth rate for experimental [10], Paris law and the simulation results.	95
4.6	Mode I damage plots for 14000 cycles with 700 cycles envelope loading. Applied load $G_I/G_c = 0.38$ and for $l_e = 1/21mm$ mesh size	96
4.7	Mode I rate of fatigue damage per 100 cycles. Applied load $G_I/G_c = 0.452$ and for $l_e = 1/25mm$ mesh size.	97
4.8	The results for Mode II simulation, Paris law and experimental data [10]	97
4.9	Mixed mode 50% crack growth rate for $l_e = 1/21 mm$ mesh size	98
4.10	The crack growth rate under constant loading changes due cyclic loading	99
A.1	The crack and the inclusion in the element domain and the level set value for the inclusion (right)	110
A.2	Von-Mises stress (MPa) and crack evolution for inclusion far from the initial crack	111
A.3	Von-Mises stresses (MPa) for un-melted particles at (1.5, 1.5), radius=0.5	111
A.4	Von-Mises stresses (MPs) for Un-melted particles at (1.5, 2.3), radius=0.5. The crack tries to avoid the inclusion with higher Young's modulus	112
A.5	The enrichment of finite element and Von-Mises stresses (MPa) for initial crack (left) and the grown crack after 40 iterations (right)	113
A.6	Crack initiation in SLS printed Nylon-12 specimen based on table A.2 setting	114

A.7 Crack initiation in SLS printed Nylon-12 specimen based on table A.3 setting	114
A.8 Crack progression in SLS printed Nylon-12 using scan variables in table A.2	116
A.9 Crack progression in SLS printed Nylon-12 using scan variables in table A.2.	117

List of Tables

3.1	Material Properties for HTA6376/C [56], E and G values are in GPa .	74
3.2	Material properties for T300/977-2 laminate[53]	80
4.1	Material properties and Paris law constants for HTA/6376C carbon/epoxy[10]	92
A.1	Nylon-12 properties from [134]	109
A.2	Build parameters of SLS printed Nylon-12	113
A.3	Build parameters of SLS printed Nylon-12	113

Nomenclature

α	Mode interaction parameter
β	Mixed mode ratio
δ	Variation of a function
δ_n	Relative displacement normal to the crack
δ_s	Relative displacement parallel to the crack
δ	Relative displacement vector at cohesive zone
ϵ	Strain tensor
ϵ_{ij}	Strain components
$\epsilon_{ij}^{(1)}$	Actual strain components
$\epsilon_{ij}^{(2)}$	Auxiliary strain components
$\dot{\epsilon}$	Strain rate
η	Local curvilinear coordinate system
θ	Crack angle with respect to global coordinate system
λ	Equivalent one dimensional opening displacement for mixed mode opening
λ_c	Critical equivalent one dimensional opening displacement at failure
λ_y	Equivalent one dimensional displacement for damage initiation
ν, ν_{ij}	Poisson's ratios for isotropic and orthotropic materials
ζ	Local curvilinear (mapping) coordinate system
ζ^*	Modified local coordinate for partially cut element
σ	Stress tensor
$\bar{\sigma}$	Stress tensor in local coordinate system
σ_0	Applied normal traction
σ_{ij}	Stress components
$\sigma_{ij}^{(1)}$	Numerically calculated stress component
$\sigma_{ij}^{(2)}$	Auxiliary stress component
$\dot{\sigma}$	Stress rate
τ	Traction tensor at crack surfaces
$\dot{\tau}$	Traction rate
τ_0	Equivalent one dimensional cohesive zone maximum traction
τ_n	Normal traction at cohesive zone

τ_s	Shear traction at cohesive zone
$\Phi(\mathbf{x})$	Level set function for the crack-tip normal
$\Psi(\mathbf{x})$	Level set function for the crack
w	weight function
Γ	Boundary/contour
Γ_c	Crack surfaces
Γ_t	Traction (natural) boundary
Γ_u	Displacement (essential) boundary
Ω	Domain
a	crack
\mathbf{a}_i	Enriched degrees of freedom (crack)
A	Area
A_D	Damaged surface area
\mathbf{b}_i	Crack-tip enriched degrees of freedom
\mathbf{B}	Matrix of shape function derivatives
\mathbf{B}^a	Matrix of shape function derivatives for crack enrichment
\mathbf{B}^α	Matrix of shape function derivatives for crack-tip enrichments
\mathbf{B}^c	Matrix of shape function derivatives for interface/inclusion enrichment
\mathbf{B}^u	Matrix of shape function derivatives for standard degrees of freedom
C	Contour
d_i	Nodal damage value
D	Damage
\mathbf{D}	Material modulus matrix
E, E_i	Isotropic and orthotropic Young's modulus
E^*	Equivalent Young's modulus
\mathbf{f}	Nodal force vector
\mathbf{f}^u	Nodal force vector for standard degrees of freedom
\mathbf{f}_i^a	Nodal force vector for enriched degrees of freedom
\mathbf{f}^b	Body force vector
\mathbf{f}_u^{ext}	External force vector
\mathbf{f}_u^{int}	Internal nodal force vector
\mathbf{f}_a^{int}	Internal nodal force vector for cohesive force

F	Crack-tip enrichment functions
G	Shear Modulus
G	Fracture energy release rate
G_I, G_{II}	Mode I and II energy release rates
G_c	Critical energy release rate
G_{cI}, G_{cII}	Critical mode I and II energy release rates
H	Heaviside function
I	Interaction matrix
J	J-Integral
$J^{(1)}, J^{(2)}$	Actual and auxiliary J-Integrals
\mathbf{K}	Stiffness matrix
\mathbf{K}_{ij}^{rs}	Stiffness matrix components
K	Stress intensity factor
K_c	Critical stress intensity factor
K_I, K_{II}	Mode I, II stress intensity factors
L	Specimen characteristic length for transversal crack test
l_e	Characteristic element length
l_{cz}	Cohesive zone length
m	Number of enrichment types
M	Moment-load
\mathbf{n}	Normal vector
\mathbf{N}_j	Matrix of shape functions
N_j	Shape function
$P(x)$	Enrichment function
q	Arbitrary smoothing function
Q_i	Nodal value for arbitrary smoothing function
r	Radial distance to the crack-tip
\mathbf{R}	Rotation matrix
\mathbf{S}	Compliance Matrix
$\bar{\mathbf{S}}$	Compliance Matrix in local coordinate system
\mathbf{t}	Surface traction at traction boundary
\mathbf{T}	Tangential modulus matrix for the cohesive zone
\mathbf{u}	Displacement vector

\mathbf{u}^h	Approximated displacement vector
$\hat{\mathbf{u}}$	Continuous displacement approximation vector
\mathbf{u}^{enr}	Enhanced displacement approximation vector
$\dot{\mathbf{u}}$	Velocity vector
$\mathbf{u}_i^{(1)}, \mathbf{u}_i^{(2)}$	Actual and auxiliary displacement vectors
U_p	Surface energy
W	Strain energy
x	Position vector
X_i, Y_i	x and y component of node i force

BEM	Boundary Element Method
FRC	Fibre Reinforced Composites
CZM	Cohesive Zone Model
CM	Computational Mechanics
DCB	Double Cantilever Beam
DOF	Degrees Of Freedom
ERR	Energy Release Rate
FE	Finite Element
FEA	Finite Element Analysis
GFEM	Generalized Finite Element Method
LEFM	Linear Elastic Fracture Mechanics
LSM	Level Set Method
PU	Partition of Unity
PUFEM	Partition of Unity Finite Element Method
SIF	Stress Intensity Factor
XFEM	eXtended Finite Element Method

Chapter 1

Introduction

1.1 Motivations

Computational Mechanics (CM) is one of the most important tools in study and characterization of engineering systems and phenomena governed by the laws of mechanics. In the past few decades, CM has had a significant influence on manufacturing, transportation, communication and several other industries by transforming the design and simulation of advanced technologies [101]. Linear-elastic stress analysis is a good example where structural analysis is carried out effectively by means of computational methods. However, for many non-linear analysis, such as fracture and failure analysis, the numerical approaches are still an ongoing research topic. This deficiency is more evident in composites where the internal structure causes further non-linearities in the analysis.

An important category of composite materials is Fibre Reinforced Composites (FRC). FRCs are used extensively in aerospace, transportation, automotive and civil infrastructures due to their superior mechanical and chemical properties. In fact, advanced composites are the material of choice when combination of high strength and low weight is needed [90]. FRC use in the modern commercial aircraft fuselage and wing structures is a good examples of such applications. By using FRC and other composites instead of Aluminium in Boeing 787 airframe, the weight of the aircraft was reduced by twenty percent and resulted in significant reduction in fuel consumption [1].

For many FRC applications, failure is not an option. These advanced composite parts usually require careful examination and simulation in order to check it's re-

sponse to extreme working condition and possible material failure. So far, in spite of the advances in the computational analysis of stress and fracture, engineers are still relying extensively on experimental data for sensitive applications. For example, a large airframe would require more than ten thousand tests for the safety certification [33].

An FRC consist of carbon fibres in a matrix of a less strong material such as epoxy resin. The fibres can be used in different arrangements and lengths depending on the desired properties. These structures are susceptible to many production and service defects under loading. Fracture is the most probable failure cause for these materials which can drastically affect the part load carrying capacity. The internal structure of FRCs is prone to diverse fracture processes such as matrix cracking, matrix-fibre debonding, fibre breakage and delamination. Analytical solutions can only deal with simple setups and for more complex situations the equations are computationally solved over an assembly of the discretized material domain using numerical methods such as Finite Element Analysis (FEA). In the case of FRCs however, the criteria are not as developed and industries are still relying on expensive experimental approaches. Some of the factors in computational fracture mechanics that has led to this shortage in composite fracture analysis are:

- The intricate internal structure of composites results in complex failure mechanisms in different scales. Debonding, delamination and fibre breakage are well-known failure mechanisms in FRCs.
- Many computational techniques in the fracture analysis are borrowed from the conventional material approaches which sometimes are not suitable for composite materials, such as in fatigue analysis [58].
- It is only a few decades that the power of computers have had a significant improvement and became capable of handling complex numerical simulations.

In order to study the fracture process of composites, it is essential to consider the effect of the internal structure on the fracture processes. In this regard, depending on the scale of the observation, various structural details are observed. By considering the changes that are caused by the heterogeneity of fibre-matrix mixture, the simulation

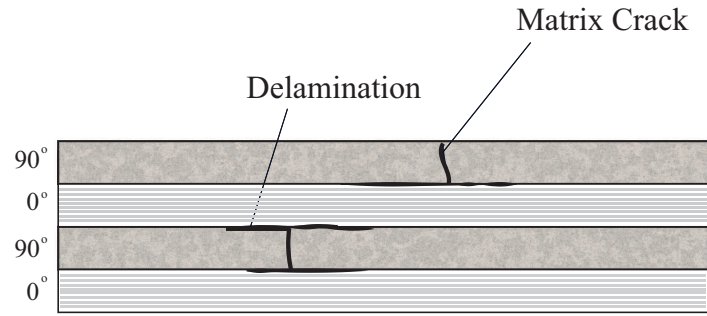


Figure 1.1: Two major cracking modes in composites are transversal cracks and delamination

is being carried out at micro-scale. By zooming out and considering the composite to be homogeneous and orthotropic linear elastic, the mechanical properties are represented in an average sense and the observation is considered at macro-scale. In this case, the fibre/matrix debonding or fibre pullout is not considered explicitly. One more category exists between the two mentioned scales that is called mesoscale. In mesoscale the smallest representative volume of the composite structure, or laminae, is considered as the smallest scale of observation. There are simulation tools for all of the scales or with a combination of them. In this work, the focus is on the matrix cracking and delamination and both of them fall into the meso and macro-scale analysis category.

Main theoretical approaches for crack analysis consider the crack either a strong discontinuity that creates internal boundaries in the material field (fracture mechanics) or continuum based approaches which treats the crack as a reduction of the material's strength/stiffness or damaged [95]. These approaches have been exploited extensively in the computational mechanics of fracture. However, there are still challenges in applying them to various fracture processes in composites. It is not easy to neglect the effect of the internal structure of composites on the fracture process and a computational tool is needed that can simulate cracks while including some level of structural details in the solution. For example, the techniques that use the analytical solutions for the crack-tip stress/displacement fields (such as crack tip enrichments in XFEM) face difficulty when the crack approaches an interface between two orthotropic materials where analytical solutions are either not available or complicated. Extended Finite Element Method (XFEM) was chosen for this project as it offers

the capacity to include such structural complexities with high level of mesh independence. Rather a new extension to the classical Finite Element Method (FEM), XFEM has great potentials for further development in the computational modelling of composite fracture.

In the end, it seems obvious that with such diverse applications of advanced composite materials in modern designs, powerful numerical tools are in high demand to avoid costly and time consuming experimental approaches. This demand is even more evident in failure and fracture analysis of composite structures which has motivated the author to undertake this study.

1.2 Aims and Objectives

This study aims to investigate the numerical tools and techniques used for crack evaluation in composite structures and to develop new numerical techniques for a more accurate fracture and fatigue analysis. The objectives of the present project are defined accordingly in order to develop and equip XFEM with more robust tools in order to simulate fracture process in composite structures under static and fatigue loading. These simulations rely heavily on accurate calculation of the fracture mechanics parameters such as the Energy Release Rate. The objectives of the present project can be summarized as:

- Investigation of the current numerical techniques for crack analysis in FEM and XFEM by studying how the FM parameters are evaluated. In particular, J-Integrals are investigated to find out how the material heterogeneous and orthotropic structure affect the results.
- Testing the J-Integral performance in XFEM platform.
- Finding appropriate physical model(s) based on the outcome of the first objectives and developing an effective mathematical model for fracture/fatigue of composites in XFEM.
- Develop code/subroutines in order to implement the model in XFEM and verifying the results.

1.3 Fibre Reinforced Composites

FRCs consist of two phases; fibres and matrix. The fibres have higher stiffness and act as reinforcement where the matrix is made of a material with lower strength and stiffness such as polymers and its job is to hold the fibres together. In this study, the emphasis is on polymer matrix. FRCs are divided into several subgroups based on the way the fibres are encased in the matrix. The fibres can be embedded in continuous, chopped or woven forms. In this work, the focus is on the FRCs with continuous and unidirectional fibres (Fig. 1.2). The fibres increase the strength of

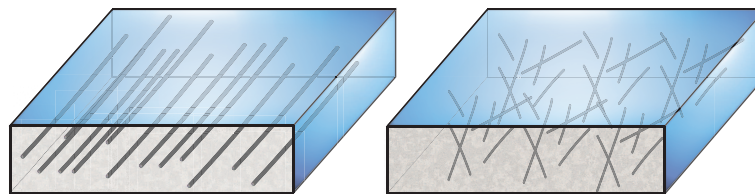


Figure 1.2: Continuous unidirectional (left) versus chopped fibre reinforcement.

the material in their direction. This results in the loss of isotropy with different stiffness tangent and normal to the fibre direction. Figure 1.2. shows the smallest representative volume of a composite structure known as laminae. Laminae can be used solely or stacked together with more laminae to form a "laminated" [72]. By stacking laminae on top of each other, higher stiffness in desired directions (in case of laminae is not isotropic) can be achieved.

1.4 Mechanics of Composite Materials

The mechanical properties of FRCs depend on the mechanical properties of its ingredients, fibre orientation, and the volumetric fibre/matrix ratio. Composites can be studied either from micromechanical or macromechanical viewpoints. In micromechanics the interactions between ingredients of the composite structure are studied while in macromechanics the effect of the ingredients properties only considered in an average sense and independent of location. In other words, the material can be

considered homogeneous if the scale of observation is much larger than the fibre diameter [79] (it is reminded that when lamina is the smallest observed representative volume, the study is in mesoscale, however, since each lamina is numerically represented separately, the macroscale formulation can be applied to individual laminae by considering them homogenized). In the present work macromechanical formulations are considered. The mathematical model for the composite material is built assuming elastic behaviour. Generalized Hooke's law is applied:

$$\bar{\sigma} = \bar{\mathbf{C}} : \bar{\epsilon} \quad (1.1)$$

$\bar{\sigma}$ is the stress tensor and the strain tensor is depicted by $\bar{\epsilon}$. $\bar{\mathbf{C}}$ is a fourth-order elasticity tensor with Cartesian components \bar{C}_{ijkl} representing 81 entities. By considering the stress and strain tensors symmetries and the symmetry imposed by the strain energy function, the $\bar{\mathbf{C}}$ elastic constants reduces to 21 elastic modulus. These 21 constants form the general elasticity tensor for homogeneous material [122]. More components of these tensors are eliminated when material symmetries are taken into account. The material can have planes of symmetry which means the properties do not change in perpendicular direction to that plane. This is where local and global coordinates need to be defined separately. These directions match the microstructure of the material (i.e. fibre orientation). The coordinate system based on the orientation of the material's elastic properties is regarded as local coordinate system $\{1, 2, 3\}$. Materials with three perpendicular planes of symmetry are called orthotropic and they have three different elastic modulus (E_i , $i = 1, 2, 3$) along normals to the symmetry planes. By eliminating the symmetric elements these three directions, the compliance tensor can be built by 9 independent stiffness constants:

$$\bar{S}_{ij} = \bar{C}_{ij}^{-1} = \begin{bmatrix} \frac{1}{E_1} & -\frac{\nu_{21}}{E_2} & -\frac{\nu_{31}}{E_3} & 0 & 0 & 0 \\ -\frac{\nu_{12}}{E_1} & \frac{1}{E_2} & -\frac{\nu_{32}}{E_3} & 0 & 0 & 0 \\ -\frac{\nu_{13}}{E_1} & -\frac{\nu_{23}}{E_2} & -\frac{1}{E_3} & 0 & 0 & 0 \\ \cdot & \cdot & \cdot & \frac{1}{G_{23}} & 0 & 0 \\ \cdot & \cdot & \cdot & \cdot & \frac{1}{G_{13}} & 0 \\ \cdot & \cdot & \cdot & \cdot & \cdot & \frac{1}{G_{12}} \end{bmatrix}$$

C_{ij} and S_{ij} are elastic tensor and compliance matrix with contracted notations, ν_{ij} are the Poisson's ratios and G_{ij} corresponds to the shear modulus in i, j -planes. For FRCs, direction one is aligned with the fibres where direction 2 and 3 are the first

in-plane transverse and the second out of plane transverse directions respectively (Fig.1.3). Unidirectional FRC laminae have another symmetric property in the plane

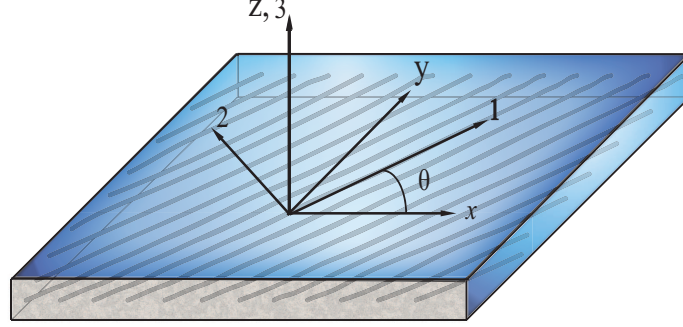


Figure 1.3: The fibres are aligned with the first local axis

perpendicular to the fibres (in 2-3 plane). In this surface, the elastic modulus remains constant for all rotation about the first axis. This condition is regarded as transversely isotropic (Fig. 1.4). Considering the symmetry about the first axis, the compliance matrix for transverse isotropic material (in local coordinates) becomes:

$$\bar{S}_{ij} = \begin{bmatrix} \frac{1}{E_1} & -\frac{\nu_{21}}{E_2} & -\frac{\nu_{31}}{E_3} & 0 & 0 & 0 \\ -\frac{\nu_{12}}{E_1} & \frac{1}{E_2} & -\frac{\nu_{32}}{E_3} & 0 & 0 & 0 \\ -\frac{\nu_{13}}{E_1} & -\frac{\nu_{23}}{E_2} & -\frac{1}{E_3} & 0 & 0 & 0 \\ \cdot & \cdot & \cdot & \frac{1}{G_{23}} & 0 & 0 \\ \cdot & \cdot & \cdot & \cdot & \frac{1}{G_{13}} & 0 \\ \cdot & \cdot & \cdot & \cdot & \cdot & 2\left(\frac{1}{E_1} - \frac{\nu_{21}}{E_2}\right) \end{bmatrix}$$

To be able to use the elasticity tensor it has to rotate and adjust to the global coordinate system $\{x, y, z\}$ for each particular problem. This is simply done by using transformation R :

$$\mathbf{R} = \begin{bmatrix} \cos^2\theta & \sin^2\theta & 0 & 0 & 0 & 2\sin\theta\cos\theta \\ \sin^2\theta & \cos^2\theta & 0 & 0 & 0 & -2\sin\theta\cos\theta \\ 0 & 0 & 1 & 0 & 0 & 0 \\ 0 & 0 & 0 & \cos\theta & -\sin\theta & 0 \\ 0 & 0 & 0 & \sin\theta & \cos\theta & 0 \\ -\sin\theta\cos\theta & \sin\theta\cos\theta & 0 & 0 & 0 & \cos^2\theta - \sin^2\theta \end{bmatrix}$$

θ is the angle between x-axis and the fibre direction (axis-1). The elasticity tensor in the global coordinate system is:

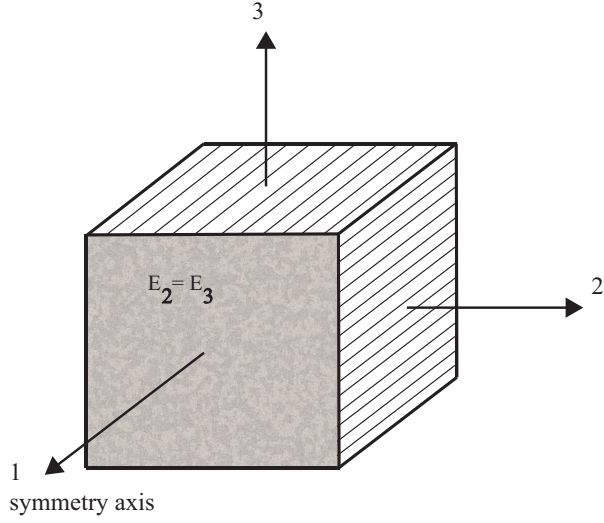


Figure 1.4: Unidirectional FRCs are transversely isotropic

$$\mathbf{S} = \mathbf{R}^{-1} \bar{\mathbf{S}} \mathbf{R} \quad (1.2)$$

Also for the stress tensor in the global coordinates:

$$\bar{\boldsymbol{\sigma}} = \mathbf{R} \boldsymbol{\sigma} \quad \text{where} \quad \boldsymbol{\sigma} = \{\sigma_x, \sigma_y, \sigma_z, \sigma_{yz}, \sigma_{zx}, \sigma_{xy}\}^T \quad (1.3)$$

with the constitutive relation as $\boldsymbol{\epsilon} = \mathbf{S} : \boldsymbol{\sigma}$.

1.5 Fracture of composite structures

The layered, non-homogeneous and orthotropic body of FRC can experience different fracture mechanisms such as:

- Matrix cracking. This type of crack is usually the first fracture mechanism that takes place and can help occurrence of other modes of fracture
- Fibre matrix debonding is when the adhesion between matrix and fibre is broken, leading to the reduction of the material strength.
- Fibre breakage, which is usually the final fracture mode in FRCs. Since the fibres are the ingredients that carry the load, fibre breakage normally causes significant reduction of the load carrying capacity and even total failure.

- Delamination. One of the most common fracture modes and severe one as well. Delamination happens when the interface between the two laminae fails for example due to high stress concentration close to the interface, or production faults.

Fatigue theories for Composites

Most of the studies on composite fatigue are based on the previous studies on metal fatigue fracture. Composites are heterogeneous anisotropic materials and the damage does not appear in a localized manner as it is in homogeneous materials (Fig.1.5) but rather it is the accumulation of damage [58]. Speaking of composite fracture, there are two categories of theories for the fatigue life prediction; one uses macroscopic failure criteria and does not consider the mechanisms involved in the failure such as stress-cycle (S-N) curves and the second group of theories are based on the stiffness and strength degradation due to damage accumulation [108]. However, FM approaches for a distinct localized crack are still used for composites provided that the right scale of observation and appropriate homogenization assumptions are made. In this study, fracture mechanic approach is used in conjunction with a damage based model through the framework of Cohesive Zone Model (CZM).

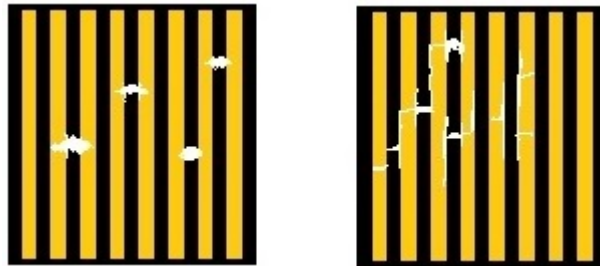


Figure 1.5: Damage distribution in fibrous composites. Fibre bridging in brittle composites (left), interface debonding propagation and finally fibre breakage (right)

1.6 Failure analysis of materials: Theoretical background

There are three main approaches for analysing fracture: continuum-based plasticity, discontinuous approach (fracture mechanics) and damage mechanics which have all

been used frequently in computational methods [95]. Fracture mechanics deals with strong discontinuities and define the crack explicitly where in plasticity and damage mechanics the displacement field keeps its continuity. In some cases, it is possible to combine the theories from both continuum and discrete approaches with some modifications and use fracture mechanics for weak discontinuity problems. In the present project, a damage based cohesive law is used for fatigue fracture analysis in XFEM which is a discontinuous method. In this section, fracture and damage mechanics are briefly discussed while plasticity is omitted as this project does not deal with plastic deformations.

1.6.1 Continuous Approaches: Damage Mechanics Approach for Cohesive Zone Model

An early definition of damage variable was first introduced by Kachanov in 1958 [74]. The damage definition ranges from scalar form for isotropic material and extends to second or fourth order variables for non-isotropic materials [126]. Damage describes the deterioration of stiffness and strength of a material due to the formation of microvoids and microcracks under load. These microcracks are discontinuities in a medium although it is considered continuous from large-scale viewpoint [83]. For this purpose, a Representative Volume Element (RVE) can be defined which is large enough to represent the homogenized variables for the material properties. The damage density is proportional to the micro-cracks in the RVE. The stiffness of the model reduces if the damage increase. The constitutive relation for stress and strain for a damaged material is written as:

$$\boldsymbol{\sigma} = (1 - D)\mathbf{C}\boldsymbol{\epsilon} \quad (1.4)$$

The value of damage D changes from zero for intact material to one for the case when the material has totally lost its strength. One approach for using Damage Mechanics formulation in a localized manner is through the application of the Cohesive Zone Model. Cohesive zones are formed near the crack-tip where the material undergoes softening or degradation. The pioneers of this approach [40, 61, 15] developed the model based on the assumption of an existing strong discontinuity as it is described by the fracture mechanics while a cohesive zone exists in the front of the crack-tip. This way allows removal of the singularity such that the stresses in the material do

not exceed the maximum stress the material can sustain. Regarding damage models, a traction-separation law relates the cohesive traction to the displacement in the CZ. CZM has been used in numerous FEA codes [4, 6, 28, 53] and partition of unity based models [143, 155, 98, 93]. It should be noted that although many of these implementations are done using discontinuous numerical approaches (i.e. XFEM, interface modelling), from the theoretical point of view, the model still falls under continuous analysis category. Cohesive zone damage models are local damage models but they can offer a level of mesh independence if the mesh is refined sufficiently [137].

1.6.2 Discontinuous approaches (Fracture Mechanics)

The fracture mechanics approach characterises an existing crack by means of an energy-based criterion. Griffith [55] discovered that internal cracks and flaws have an important role in defining the material's strength which is significantly smaller than its strength in theory. He characterised the crack based on the total change in the energy during the crack propagation. A crack can grow if there is enough energy in the structure to defeat the crack surface energy of the material [7]. Irwin [69] extended the Griffith theory and introduced the energy release rate (ERR) and stress intensity factor definitions. Westergaard [144] developed a solution for the stress distribution around the crack tip using Airy function and formulated the stress singularity around the crack tip for three different mode stress intensity factors (for $r \ll a$) [144]:

$$\sigma_x = \sigma_0 \sqrt{\frac{a}{2r}} \cos \frac{\theta}{2} \left(1 - \sin \frac{\theta}{2} \sin \frac{3\theta}{2} \right) + \dots \quad (1.5)$$

$$\sigma_y = \sigma_0 \sqrt{\frac{a}{2r}} \cos \frac{\theta}{2} \left(1 + \sin \frac{\theta}{2} \sin \frac{3\theta}{2} \right) + \dots \quad (1.6)$$

$$\sigma_{xy} = \sigma_0 \sqrt{\frac{a}{2r}} \sin \frac{\theta}{2} \cos \frac{\theta}{2} \cos \frac{3\theta}{2} + \dots \quad (1.7)$$

Or in general form in 2D:

$$\sigma_{ij} = \frac{1}{\sqrt{r}} \{ K_I f_{ij}^I(\theta) + K_{II} f_{ij}^{II}(\theta) \} \quad (1.8)$$

r, θ and x, y axis are depicted in Fig. 1.6. The stress intensity factors are defined as:

$$K_I = \lim_{r, \theta \rightarrow 0} \sigma_{yy} \sqrt{2\pi r} \quad (1.9)$$

$$K_{II} = \lim_{r, \theta \rightarrow 0} \sigma_{xy} \sqrt{2\pi r} \quad (1.10)$$

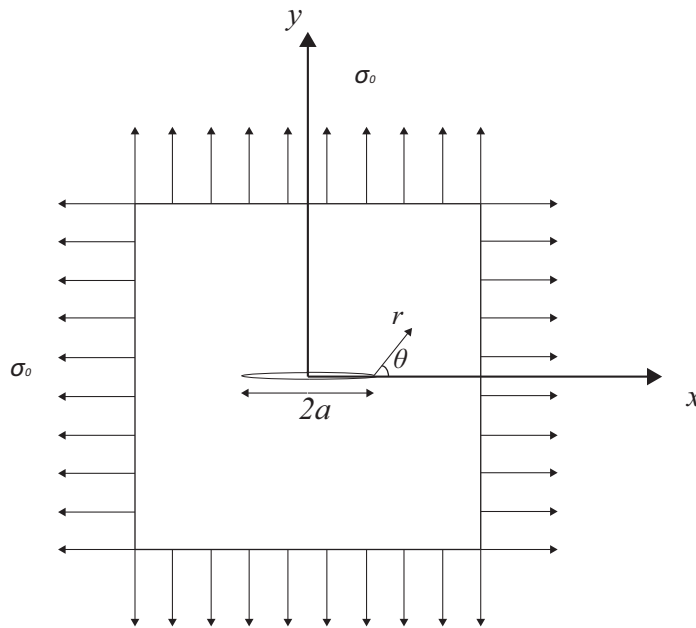


Figure 1.6: Infinite plate with centre crack of length $2a$ under uniform traction

This solution is for a crack extended by $2a$ at the centre of an infinite plate under uniform biaxial stress σ_0 for small values of r (Fig. 1.6). K_I, K_{II} are the SIFs for mode I and II crack openings (Fig. 1.7). SIF can be described as a measure of the stress singularity severity. Irwin [69] proved that the magnitude of the elastic stress field near a crack-tip is controlled by the SIF as $K \propto \sigma_0 \sqrt{\pi r}$. The crack will propagate when K reaches a critical value K_c . The critical value for each mode of crack opening is defined individually however for mixed mode crack opening, a mixed mode criterion with a combination of intensity factors are needed.

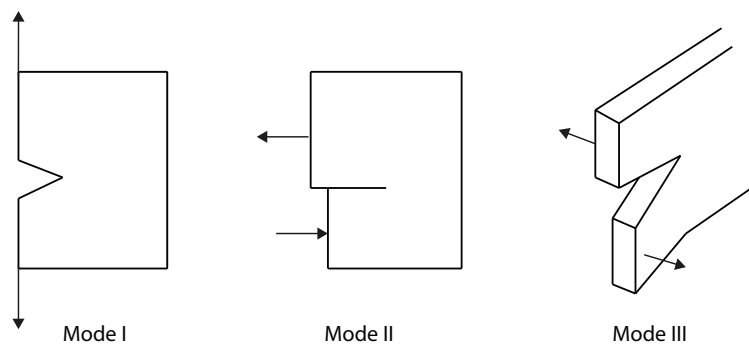


Figure 1.7: Different modes of crack opening displacement

The next major development in fracture mechanics was the advent of J- Integrals

[115, 118] which made it possible to measure the ERR by means of a path-independent contour integral. In the beginning, J- Integrals were developed to deal with plastic effects at the crack tip. When the crack-tip behaves in a plastic way, the stress field from elastic solution cannot characterize the crack and linear models are no longer valid. However, it is possible to reduce the J- Integral formulation for the LEFM cases. J- Integral formula for two dimensional analysis reads:

$$J = \int_c (W dy - \mathbf{T} \cdot \frac{\partial \mathbf{u}}{\partial x} ds) \quad (1.11)$$

where

$$W = W(\boldsymbol{\epsilon}) = \int_0^{\boldsymbol{\epsilon}} \sigma_{ij} d\epsilon_{ij} \quad (1.12)$$

W shows strain energy per unit volume [27]. C is a contour enclosing the crack-tip, \mathbf{T} shows the traction tensor with $T_i = \sigma_{ij} n_j$ and ds is an infinitely small element of C . For composites, the fracture mechanics has to be adapted for different scenarios such

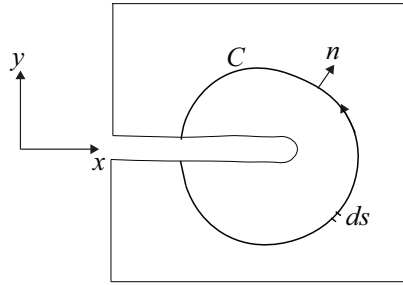


Figure 1.8: J- Integrals can be calculated on any closed path around the crack tip

as a crack in the orthotropic materials [100, 125, 11, 87] or a crack at the interface of orthotropic bimaterial [145, 42, 119, 60] where similarly ERR and SIF are used for evaluation of the crack status. Distinctive characteristics of the discontinuous approaches are the strong discontinuity in the displacement field and the crack-tip singularity.

Fatigue in Fracture Mechanics

In the 1960s, Paris et al. [105, 106] proposed a fatigue theory based on FM approach assuming the similitude concept. In this approach, the crack-tip condition is described by a single FM parameter (SIF or ERR) and might not be correct for variable amplitude loading. Unlike S-N curve method, an energy based parameter is used

instead of stress. The growth of the crack under cyclic loading is formulated based on the following parameters:

$$\frac{da}{dN} = f(\Delta K, \mathcal{R}, N, \text{Temperature}, \text{loadhistory}) \quad (1.13)$$

\mathcal{R} is the load ratio for maximum and minimum stress intensity factor (K) and N represents the number of cycles. Some researchers used J- Integrals for the fatigue of materials with large yielding since large plastic deformation contradicts the similitude assumption*¹[7]. The Paris law has been extensively applied for composite fatigue although most of them are relatively brittle materials [141, 99].

1.7 Computational methods for failure analysis

The theoretical approaches described in the previous section are used in a variety of numerical methods. Although one theoretical framework might be more compatible with a particular numerical method, there is not always a definitive way to choose one approach over the other and sometimes even a combination of them are used. A quick description of well known numerical methods is provided in this section as well as the reasons why XFEM was selected for the study of fracture in FRCs.

1.7.1 Boundary Element Method (BEM)

BEM for structural analysis was first developed by Russian scientists Muskhelishvili, Mikhlin and Kupradze (as cited in [5]) for solving linear partial differential equations in integral equation form. The application of BEM in the calculation of stress intensity factor in orthotropic materials was studied by Doblar et al. [34] and Snyder and Cruse [128] were among the first researchers that applied BEM to the cracks in anisotropic materials. Quasi-static and dynamic solutions for crack propagation in BEM in orthotropic material was proposed by Sollero et.al [129] and Gracia-Sanchez et. al [51].

Blázquez et. al [25] used BEM for stress analysis of delamination crack in $[0/90]_s$ symmetric laminates and according to their results, BEM proved to be more robust for very small crack openings which is difficult for FEM to capture and would require

¹Similitude assumption is the condition in which the crack-tip can be described by one parameter, such as SIF

extremely high mesh density. The same problem is solved in FEM and XFEM in the present study in chapter 2.

1.7.2 Meshless Methods

Meshless methods are a category of numerical analysis that does not need a predefined fixed connectivity and the solution is based on the interaction of each node with all its neighbours. These nodes are used to define the geometry and since there is no connectivity in the nodal discretization, the discontinuities can be easily included in the domain. There are numerous meshless methods for a variety of engineering problems. Element-free Galerkin Method (EFG) [19, 20] Isogeometric analysis [52, 64] and HP cloud [39] are examples amongst many.

1.7.3 Finite Element Method (FEM)

Finite element method is perhaps the most known computational tool in structural analysis that has frequently been used for crack problems. FEM in its simple classical form has to embed the crack in the solution domain by conforming the mesh to the discontinuity. In this case, if the crack propagates, the domain has to be remeshed. Including these discontinuities in the finite element domain is easily possible but Bazant and Planas [17] proved that fracture mechanics solutions have to be embedded in the solution to avoid mesh or size dependency since fracture mechanics is a non-local approach. Quarter point element is one of the most popular techniques for the crack-tip simulation by replacing the midside node of an element by a quarter of the element size toward the crack-tip to create $\frac{1}{\sqrt{r}}$ singularity. This method was developed by Barsoum [16] for simulation of the singularity which was successfully implemented by Fawkes et. al [47].

1.7.4 Enriched approximations

FEM limitations caused by mesh dependency of the discontinuity led to the development of alternative approaches for crack simulation. Generalized Finite Element Method (GFEM) [50] and XFEM [18, 36, 37] are such approaches that embraces the partition of unity phenomenon [12, 54, 91] which can describe the crack independent of the mesh. XFEM and GFEM are based on similar formulation except that XFEM

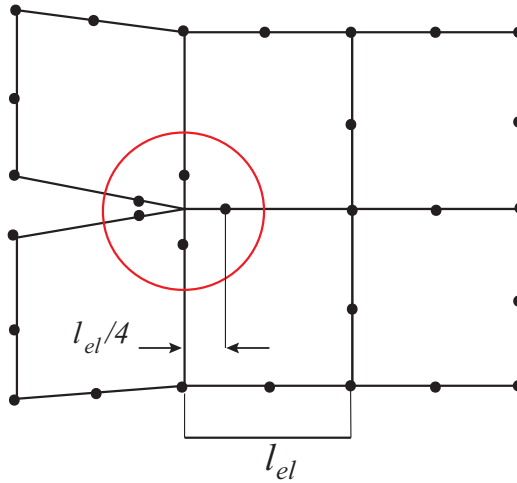


Figure 1.9: Quarter point element at the crack-tip

modifications are only applied to the nodes in the vicinity of the crack and not to the whole domain, unlike GFEM.

Partition of Unity

Partition of unity concept was proposed by Melenk and Babuška [91] which they originally used for solving differential equations numerically. They called it the partition of unity finite element method (PUFEM) which is a meshless approach. Partition of unity can be described as a set of functions P_n in a topological domain with the following property:

$$\sum_{k=0}^n P_n(x) = 1 \quad (1.14)$$

Finite element shape functions for an isoperimetric element is a set of partition of unity functions as they add up to 1 which also satisfies the completeness condition for the solution. Completeness is referred to the ability of a series of functions to sufficiently approximate a given smooth function. The partition of unity offers a scheme for development of shape functions that provide conforming space of any local approximation [91]. Besides the inherited robustness from FEM, XFEM and GFEM can include the singularity of the crack-tip and easily accommodate several strong and weak discontinuities regardless of the mesh structure. The inclusion of the discontinuities and the crack-tip singularity (or any stress/displacement field solution i.e plastic zone) is done through the addition of special shape functions known as

enrichment. These characteristics make XFEM an ideal candidate for the modelling of orthotropic and heterogeneous materials such as layered composites. The inner structure of composites and cracks are numerically implemented using the Level Set Method (LSM).

Level Set Method

Level set method (LSM) tells the solver which elements need enrichment [49]. Osher and Sethian [102] developed LSM for the interface and boundary dynamic motion tracking. This method can define shapes (i.e. a crack or an inclusion) that are not easily defined by mathematical functions by means of a cross-section of a three dimensional surface. The level set Ψ is equal zero on the intersection line (the boundary of

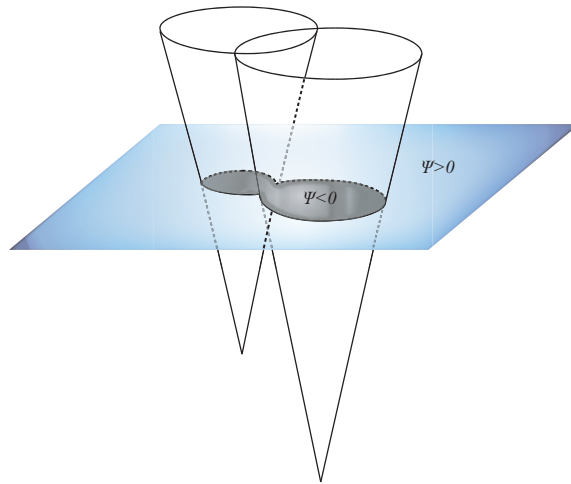


Figure 1.10: Level set method defines a complex geometry by intersecting a plane with a known volume

the geometry), negative inside (or below) the boundary and positive on the opposing side (Fig. 1.10). For a crack in the finite element domain, the level sets are defined as:

- $\Psi(x)$ level set which is the normal signed distance to the crack surface
- $\Phi(x)$ level set which is the signed distance to the line perpendicular to the crack at the crack-tip.

All the nodes of elements are assigned a Φ and Ψ value. If the element contains both positive and negative values of Ψ it is crossed by a crack. Φ , on the other hand, tells if the node is before or after the normal line to the crack tip (Fig. 1.11).

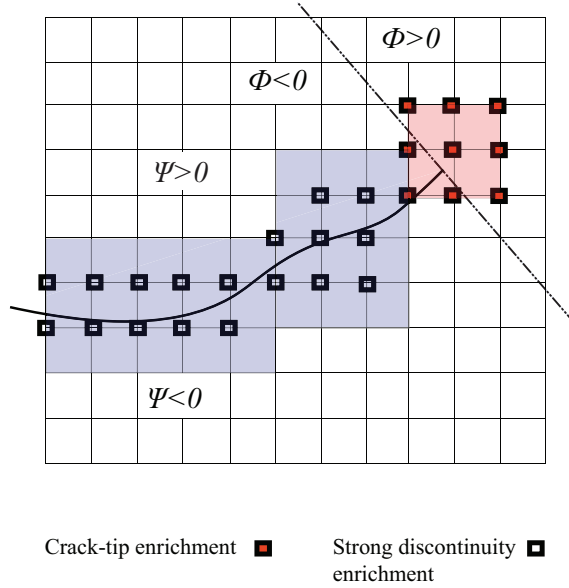


Figure 1.11: The value of Φ and Ψ at every node (and Gauss point) will define their location regarding the discontinuity

1.7.4.1 Space Discretization and Enrichment Functions

In order to approximate the displacement when the discontinuity -weak or strong- and the singular crack-tips are present, the order of completeness of the approximation functions has to increase. By including information from analytical solutions (such as an asymptotic crack-tip solution), more accurate approximations can be built. In quarter point element method the midside node is moved toward the crack tip in order to resemble $r^{-\frac{1}{2}}$ behaviour. Similarly, enrichment functions include the $r^{-\frac{1}{2}}$ term in the asymptotic solution (1.8) but this time by adding displacement terms to the standard FEM approximations. The displacement of a body crossed by a discontinuity Γ_c at any point is approximated as:

$$\mathbf{u}^h = \hat{\mathbf{u}} + \mathbf{u}^{enr} \quad (1.15)$$

The approximation \mathbf{u}^h is a combination of the standard continuous approximation $\hat{\mathbf{u}}$ and the enhanced part (\mathbf{u}^{enr}) whether it is for the crack-tip displacement approximation, inclusion or any other possible displacement filed from a priori solution [96]. Standard shape functions $N_i(x)$ approximate the continuous displacement field as:

$$\hat{\mathbf{u}}(\mathbf{x}) = \sum_{i \in n^{stin}} N_i(\mathbf{x}) \mathbf{u}_i \quad (1.16)$$

n^{std} is the number of nodes in the domain and \mathbf{u}_i is the vector of standard degrees of freedom for each node. For the enriched elements (Fig. 1.11), a partition of unity compliant shape function is built to present crack-tip or a discontinuity:

$$\mathbf{u}^{ern} = P(\mathbf{x})\llbracket\mathbf{u}(\mathbf{x})\rrbracket = \sum_{i \in n^{cut}} N_i(\mathbf{x})P_i(\mathbf{x})\mathbf{a}_i \quad (1.17)$$

\mathbf{a}_i is the vector of extra degrees of freedom and $N_i(x)$ stands for standard shape functions. P is chosen accordingly for the type of the discontinuity it represents and $\llbracket\mathbf{u}(\mathbf{x})\rrbracket$ gives the displacement components of the enhanced displacement field. For the crack opening, functions built by Heaviside or Sign functions can be used to reproduce the jump in the displacement:

$$P(\mathbf{x}) = Sgn(\mathbf{x}) = \begin{cases} 1 & \text{for } x \geq 0 \\ -1 & \text{for } x < 0 \end{cases} \quad (1.18)$$

Using a discontinuous functions such as sign function in the approximation field does not provide the interpolation property and $\mathbf{u}_i \neq \mathbf{u}(\mathbf{x}_i)$. To solve this problem a shifted enrichment function is built by using the same functions instead:

$$P(\mathbf{x}) = Sgn_{GP}(\mathbf{x}) - Sgn_i(\mathbf{x}) \quad (1.19)$$

Sgn_{GP} is the value of the sign function at Gauss point and Sgn_i is the value of the same function at each node. In this way the enrichment function vanishes at each node and the interpolation property is preserved. The crack-tip functions need similar adjustments when added to the approximation.

$$\mathbf{u}^{tip}(\mathbf{x}) = \sum_{j \in n^{tip}} N_j(\mathbf{x})P(\mathbf{x})\mathbf{b}_k \quad (1.20)$$

\mathbf{b}_j is the vector of the extra degrees of freedom for the crack-tip element nodes (n^{tip}). The function $P(\mathbf{x})$ is produced by using base functions from a priori solution. For the asymptotic field of the crack-tip in an isotropic material, the following base functions can be used [48]:

$$P^T(\mathbf{x}) = \left[1, x, y, \sqrt{r}\cos\left(\frac{\theta}{2}\right), \sqrt{r}\sin\left(\frac{\theta}{2}\right), \sqrt{r}\cos\left(\frac{\theta}{2}\right)\sin(\theta), \sqrt{r}\sin\left(\frac{\theta}{2}\right)\cos(\theta) \right] \quad (1.21)$$

θ and r are measured according to the location of the crack-tip (Fig. 1.6). There are other enrichment functions for elastic-plastic crack-tip [41], bimaterial crack-tip [133], crack-tip in orthotropic material [8], interface crack-tip between two orthotropic materials [9], and for cohesive zone [93] based on the asymptotic solution of cohesive crack-tip by Palanas and Elices [110]. In this project, the effect of the asymptotic crack-tip field enrichments (1.21) is investigated for the energy release rate calculation of the transversal crack in a $[0/90]_s$ composite laminate.

When there is an inclusion in the material, the displacement field encounters a weak discontinuity which presents itself as a strong discontinuity in the strain field. Sukumar et al. [131] first developed the material interface enrichment by multiplying the nodal level set value (Ψ) to the shape functions. This method was improved by Moës et al. [94] by creating a partition of unity shape function as:

$$P(\mathbf{x}) = \sum_i N_i(\mathbf{x}) \left| \Psi_i \right| - \left| \Psi_i \sum_i N_i(\mathbf{x}) \right| \quad (1.22)$$

as a result, by building a shape function that vanishes at the nodes, there is no need for shifting the enrichments. The displacement approximation including the standard and enriched parts for m different types of enrichments can be written as:

$$\mathbf{u}^h(\mathbf{x}) = \sum_{i=1}^{n_{stn}} N_i(\mathbf{x}) \mathbf{u}_i + \sum_{j=1}^m \sum_{k=1}^{n_{enr}} N_k(\mathbf{x}) P^j(\mathbf{x}) \mathbf{a}_k^j \quad (1.23)$$

Each enriched element only has one type of enrichment in this study. For the cohesive zone modle, no crack-tip enrichment is used and Eq. 1.23 is only used for strong discontinuity of the crack or for bimaterial interfaces. This is due to the fact that analytical solutions for the stress field around a cohesive crack are not available for more complex cases such as orthotropic materials. In fact, in many cases, the crack-tip enrichments causes more complication when other weak or strong discontinuities exist near the crack-tip.

1.7.4.2 Fatigue Modelling in XFEM

Since the advent of XFEM there have been many implementations of it for the fatigue crack growth. Sukumar et al. [132] proposed a planar 3D fatigue crack growth in XFEM. In their paper, Paris law is used to calculate the rate of crack growth. Chopp and Sukumar [30] proposed a numerical technique for multiple coplanar fatigue cracks

in XFEM in the same year. Mixed-mode cyclic crack growth for quasi-brittle materials was studied by Yangjian and Yuan [148, 149]. They combined a cyclic cohesive model with XFEM to model the fatigue crack nucleation and propagation. Kim et al. [78] used XFEM to predict the fatigue life while probabilistic equivalent initial flaw model (EIFM) was used to create distributed damage sites. Singh et al. [127] modelled the fatigue life of homogeneous plate containing multiple discontinuities in XFEM. The discontinuities (voids, cracks, inclusions) are having random size and position in the plate. In their work as well, Paris law for the fatigue crack growth is used.

Mixed mode loading analysis for fatigue crack growth was recently modelled by Varfolomeev et al. [139] for two planar specimens and they also experimentally tested their results for the bending and tension specimens. In their work, XFEM was particularly used to track the crack growth rate for Paris law regime crack growth. The effect of reinforcement particles on the fatigue resistance was studied by Ye et al. [151]. They also used Paris law to calculate the crack propagation rate in XFEM. Fretting fatigue crack growth was studied by Baietto et al. [13] using a mixed-mode Paris law. For bi-layered material interface, fatigue crack growth at the interface was modelled by Bhattacharya et al. [24] where the cyclic mode I load and thermal load were considered.

Most of the fatigue modellings in XFEM are based on Paris law for fatigue. Damage based fatigue modelling implementations of XFEM are limited to low-cycle fatigue. Xu and Yuan [148] used XFEM for low-cycle fatigue for mixed mode loading and they used a damage evolution law based on a cyclic cohesive zone model proposed by Roe and Siegmund [121]. Again, Xu and Yuan [148] solved the same problem using S-N curve and Goodman diagram in the framework of CZM and implemented it in XFEM while both static and cyclic loading damage accumulation parameters were considered. Li and Yuan [85] improved the model proposed in [148] and considered the loading ratio effect to achieve higher accuracy.

Although there are available damage based fatigue cohesive zone models for high-cycle loading, to the knowledge of the author, there is no high-cyclic XFEM implementation of CZM. For composites, CZM offers a great potential by removing the singularity (especially at the interfaces) of the crack-tip and avoiding the oscillator stress field and can offer more accurate results for calculating the fracture mechanics and damage mechanics parameters for fatigue.

1.8 Current State of the Art and Proposed Research on Composite Fatigue Fracture Modelling

The complex internal structure of composite materials brings great analytical and computational hurdles, especially for failure analysis. XFEM is capable of embedding many of these structural details and discontinuities at the same time without having to deal with mesh dependency. Interfaces, inclusion and cracks can easily be defined in XFEM for a layered composite laminate with non-isotropic properties. However, this method also suffers from some of the classic problems in computational fracture mechanics such as the crack-tip singularity issues predicted by the LEFM. Besides, the fracture mechanics parameters (i.e ERR) needs to be accurately calculated and the current techniques such as the J-Integrals show inconsistency in both XFEM and FEM implementations when it comes to the composite materials.

To avoid these difficulties, it is possible to combine damage mechanic approach with LEFM such that the problematic predictions of LEFM are avoided. In that case, there would be no need for complex approximation functions for the crack-tip as the stress levels are limited to the material maximum permitted stresses. Damage mechanics in the framework of the cohesive zone model is easily implemented in FEM or XFEM and above that, it can utilize fracture mechanic parameters. In author's opinion, this is very important since the majority of experimental tests for fatigue heavily rely on FM approaches. . For instance in fatigue modelling, the amount of available experimental data on the crack growth rate is overwhelming while in damage mechanics there are not many experimental data on the damage evolution under cyclic loading. Recently there were attempts to link the two methods [14, 136, 120] and the result was models that have the stability and flexibility of the cohesive zone models and at the same time, capable of using fracture mechanics parameters in the form of a Paris law variant.

The majority of the numerical implementations for the cyclic cohesive zone models are done using interface and cohesive element models. These techniques do not have

the mesh independence of XFEM and the crack paths are pre-defined. So far, to the knowledge of the author, the cohesive zone model for high-cyclic fatigue has not been implemented in XFEM.

1.9 Outline of the project

This project can be divided into three main subjects; first, the utilization of FEM and XFEM solvers for simulation of non-homogeneous material fracture in LEFM is investigated. This part mostly deals with the effect of the inclusions on the fracture mechanics parameters and the crack growth path. The second part is the application of damage mechanics and the cohesive zone concept in order to address the issues arose with the LEFM simulations for composites and finally, the third part is on linking the cohesive zone model with a variant of Paris law using a thermodynamically based approach for fatigue simulation.

In chapter two, the calculation of the energy release rate for a $[0/90]_s$ carbon epoxy laminate (Hexply8552) is carried out in FEM (ABAQUS) and XFEM (using an updated MATLAB code). First, the analysis is done in ABAQUS for Generalized Plane Strain (GPS) condition in three dimensions since two dimensional model with GPS elements does not allow the use of J-Integrals. The same study is carried out for plane strain condition once with ABAQUS and once with the XFEM code. This test aims to validate the code modifications to calculate orthotropic stiffness matrix. This chapter provides detailed discretization of the displacement domain for XFEM solver.

In chapter three, an XFEM cohesive zone model implementation in MATLAB is presented. A linear traction separation law and a thermodynamically based damage definition are provided. The traction separation law describes the cohesive tractions as a function of an equivalent displacement calculated from mode I and mode II opening displacements. A Newton-Raphson solver is used for the calculation of the cohesive zone since it involves non-linearities (although the domain outside the CZ is governed by linear elasticity). In the end, the code is verified by several DCB tests under force and displacement controlled loading. Also, a new subroutine is developed for the calculation of the J-Integral.

Finally, in chapter four, a high-cyclic CZM is presented which links the damage cyclic evolution to a Paris law variant. The Newton-Raphson iterative solver described in chapter three is solved at each time step while the damage is updated for an envelope of load cycles. At the end, DCB delamination tests are carried out for validation of the results.

After the conclusions and a summary of the work, in appendix one, a summary of a published work on the dynamics of crack growth in a 3D printed part is presented. This study includes the utilization of the inclusion enrichments for simulation of the un-melted particles in the Nylon parts built by SLS technique. The results highlights demonstrates the powerfulness of XFEM level set method in defining the inclusions.

1.10 Conclusion

In the introduction chapter, theories and computational techniques used for composite fracture analysis were briefly covered. The literature review on the subject highlighted the shortcomings and challenges of these approaches regarding the materials with non-homogeneous and orthotropic structure. The outcome of this chapter can be summarized in 4 points:

- The theoretical approaches for composite material studies are a continuance of the classical approaches used for isotropic and homogeneous materials, which sometimes does not fully match the reality of fracture in composites. Particularly in fatigue, the same style of formulations that was used for metals are widely applied to the composites.
- LEFM extreme predictions such as the crack-tip singularity do not settle well with computational mechanics of the composite structures. Pure LEFM approach requires involving analytical solutions numerically [17]. This is not always possible since many crack-interface combinations do not have an analytical solution and even if there is a solution, there is a great chance of complications.
- Combining approaches from damage mechanics and LEFM can help avoid some of the hurdles of the crack analysis in composites. In this regard, CZM offers a platform to include a non-linear damage based sector numerically at the crack-tip area and avoid the singular definition while at the same time it can be easily

linked to LEFM parameters. In composites, this will save a lot of complications regarding discontinuities and cracks interference.

- The abundance of strong and weak discontinuities in fractured composite materials demands a robust numerical platform. XFEM provides a powerful tool in this case by reducing the mesh dependency for discontinuity inclusion to a great extent.

XFEM has great potential for simulation of the complex structure of composite materials. This project aims to harvest this potential by developing a numerical tool to model static and fatigue crack growth efficiently.

Chapter 2

Energy release rates calculation for transversal crack in standard FEM and XFEM

2.1 Introduction

In this chapter, the energy release rate evaluation for a transversal crack is investigated using both FE and XFEM. J-Integrals are implemented in the form of area contour integrals and the aim is to find out how they interact with the internal structure of the composites. The energy release rate is used extensively in this project for quasi-static and fatigue modelling and it is important to evaluate the consistency of the method used for its calculation.

2.2 Background

When layered composite materials are subjected to loading, matrix cracks are the first type of crack that appears in the structure. This process starts with fibre-matrix debonding and micro-cracking. Increasing the load causes the micro-cracks to coalesce and grow into a transversal macro-crack[104, 22]. In a $[0/90]_s$ fibre reinforced laminate under unidirectional loading, the transversal crack often appears in the 90° ply and propagation of it can create high stress zones ahead of the crack-tip and trigger other forms of failure such as delamination or fibre fracture [113]. There has been numerous studies on the onset of delamination as a result of transversal cracks [86, 142, 154].

Fracture mechanics has been extensively used for the analysis of various forms of

composite cracking. In these attempts, FM parameters such as energy release rate (ERR) have been applied by many researchers for characterisation of different failure modes such as aerospace laminate fracture under interlaminar or compressive shear [32], individual mode energy release rate for delamination [156] and interface cracks in adhesive-bonded aerospace composite joints [29], to name a few.

There are well-known methods used extensively in simulations for the ERR evaluation including the virtual crack closure technique (VCCT) [80], finite crack extension method [38], virtual crack extension method [59, 67], J-integrals [119] and equivalent domain integral method for separation of crack opening modes ERR [112]. In this work, J-Integrals and VCCT methods are discussed briefly since the J-Integral results are compared with the result of VCCT from a static BEM simulation by París et al. [104].

2.2.1 Virtual Crack Closure Technique (VCCT)

VCCT is a mutation of the crack closure technique which is based on Irwin's crack closure integrals [70, 26]. In crack closure method, the released energy during the crack extension Δa is equal to the energy it takes to close a crack with the size equal to Δa . This technique requires a two-step solution as it uses the values for forces from step one before the crack has extended and displacement from step two. The required energy to close the crack mouth between points i and j in Fig. 2.1 is calculated as:

$$\Delta E = \frac{1}{2}[X_{1i} \cdot \Delta u_{2i} + Y_{1i} \cdot \Delta v_{2i}] \quad (2.1)$$

X_{1i} and Y_{1i} are the shear and opening forces at node i in step 1 and Δu_{2i} and Δv_{2i} are shear and normal openings of node i in step 2 as shown in Fig. 2.1 as well. In order to avoid two-step solution, modified (virtual) crack closure technique was developed based on the assumption that small extensions of the crack do not significantly change the crack-tip state [80]. This means the displacements from the node before the crack-tip can be used for the calculation (Fig. 2.2). In this case, the ERR is calculated as:

$$\Delta E = \frac{1}{2}[X_j \cdot \Delta u_k + Y_j \cdot \Delta v_k] \quad (2.2)$$

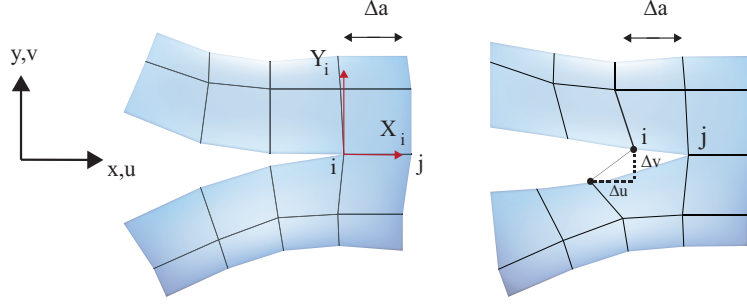


Figure 2.1: Crack Closure Technique uses forces from first step solution (left) and the displacement calculated after the crack extension (right) in the second step at node i

And the rate of change in the energy due crack extension or ERR is calculated as:

$$G = \frac{\Delta E}{\Delta a} \quad (2.3)$$

A benefit of VCCT is the ability to calculate the ERR separately for different opening modes:

$$G_I = \frac{1}{2\Delta a}(Y_j\Delta v_k) \quad (2.4)$$

$$G_{II} = \frac{1}{2\Delta a}(X_j\Delta u_k) \quad (2.5)$$

This method is used widely in fracture simulation. Xie et al [146] used VCCT in finite element method for ERR evaluation. Zou et al [156] implemented VCCT using the laminate theory to express the ERR in terms of stress-jumps and relative displacements for modes I, II, and III. They calculated ERR and at the same time the stress singularity at the crack tip was present in the form of stress jumps across the delamination but no oscillations in stress were reported in their result. Conversely, VCCT with LEFM results in oscillatory stresses field at the front of the crack-tip, which may cause divergence [111]. Paris et al. [104] implemented VCCT in static BEM which is more compatible with this technique as the boundaries of the problem are directly related to the problem features such as fracture parameters. They calculated the ERR for transversal cracks with and without considering delamination for different crack lengths.

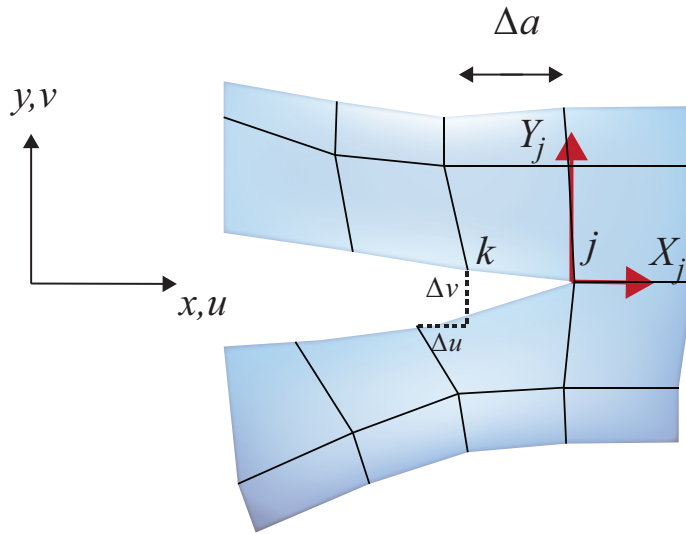


Figure 2.2: Virtual Crack Closure Technique uses forces from the crack tip node i and the displacements from node k

2.2.2 J-Integrals

J. R. Rice [116] formulated Eshelby's [45] contour integral to calculate the energy release rate associated with the crack propagation. For an edge crack in a non-linear elastic body the J-integral is equal to the rate of change in the potential energy (U_p) stored in the body:

$$J = -\frac{dU_p}{da} \quad (2.6)$$

da is an infinitesimal growth of the crack. By definition, the J-integral equals the

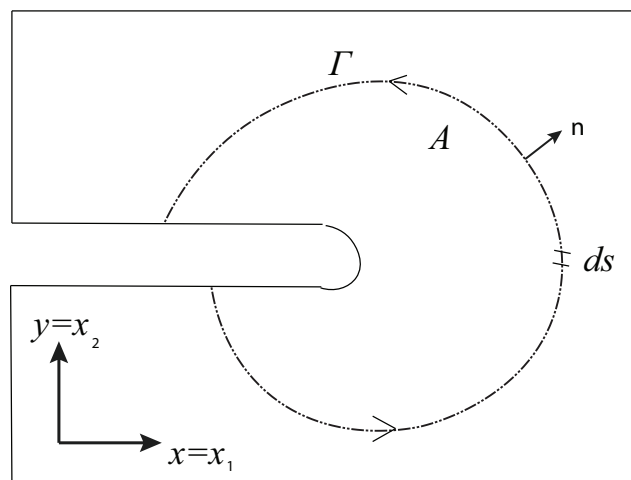


Figure 2.3: Contour integral in a two dimensional cracked body

ERR if the material is linear elastic [82]. If the material behaves in a linear elastic manner the J-integral is equal to the energy release rate. A two dimensional model for the contour integral is illustrated in Fig. 2.3. The first J-integral formula [116] was proposed in the following form:

$$J = \int_{\Gamma} (W dx_2 - \sigma_2 \cdot \frac{\partial u_2}{\partial x_1} ds) \quad (2.7)$$

W is the elastic strain energy, ds represent an infinitesimally small length of the contour Γ and σ are stress components on the integration contour. A more general form of J-integral is expressed as:

$$J_i = \int_{\Gamma} (W \delta_{1i} n_j - \sigma_{jk} n_j \frac{\partial u_k}{\partial x_i}) d\Gamma \quad (2.8)$$

where i denotes the direction along the crack line in the global coordinate system. Here it assumed that the crack is aligned with first axis (x direction). The strain energy density reads:

$$W = \int_0^{\epsilon_{ik}} \sigma_{ij} d\epsilon_{ij} \quad (2.9)$$

For the numerical implementation of the J-integrals, a domain integral (Fig. 2.4) is preferred and can provide highly accurate results [123]. Moran and Shih [97] proposed a detailed formulation for general material which was applied to many crack problems [84, 124]. Consider an area A enclosed by C_2 (Fig. 2.4). m is the outward normal of C . $m = -n$ on C_1 and $n = m$ on C_2 . As a result, $C = C_1 - C_2 + C^+ + C^-$. The crack surfaces have no tractions on C^+ and C^- . Eq. 2.8 can be written as:

$$J = \oint_C (W \delta_{1i} - \sigma_{jk} \frac{\partial u_k}{\partial x_i}) m_j q_i dC \quad (2.10)$$

q_i are weighing functions used for obtaining required domain representation for J-Integral. For a two dimensional case with the crack aligned with first axis (x_1), $q_2 = 0$ and q_1 takes the unity value on C_2 (Fig. 2.4) and 0 on C_1 . Between the two contour, q_1 possess a value between 0 and 1 and is a smooth function of x_1 and x_2 . Applying the *divergence theorem* the closed contour of are A around the crack-tip can be integrated as:

$$J = \int_A [\sigma_{ij} \frac{\partial u_i}{\partial x_1} - W \delta_{1i}] \frac{\partial q_1}{\partial x_j} dA \quad (2.11)$$

Eq. 2.11 is evaluated numerically by defining q_i and its derivatives on each node

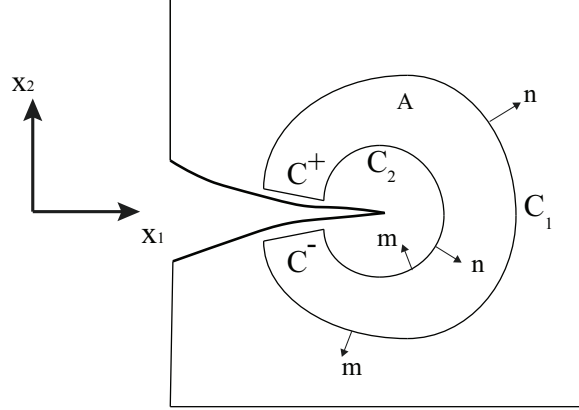


Figure 2.4: Contour integral in a two dimensional cracked body

and using the standard isoperimetrical shape function to approximate them inside the elements for a four-node quadrilateral element:

$$q_1 = \sum_{I=1}^4 N_I Q_{1I} \quad (2.12)$$

$$\frac{\partial q_1}{\partial x_i} = \sum_{I=1}^4 \sum_{k=1}^2 \frac{\partial N_I}{\partial \zeta_k} \frac{\partial \zeta_k}{\partial x_i} Q_{1I} \quad (2.13)$$

Q_{1I} is the nodal value of q_1 for node I and N_I are quadrilateral shape functions. J-integral is evaluated as:

$$J = \sum_{\text{elements in } A} \sum_1^4 \left\{ \left[\sigma_{ij} \frac{\partial \mathbf{u}_i}{\partial x_1} - W \delta_{ij} \right] \frac{\partial \mathbf{q}_1}{\partial x_i} \det \left(\frac{\partial x_k}{\partial \zeta_k} \right) \right\} w_p \quad (2.14)$$

ζ_k for $k = 1, 2$ are location coordinates according to the natural coordinates in the element and w_p are used as weights for integration over the element area. According to Shih and Asaro [123] the values of J are not sensitive to different types of smooth functions used for q . This function sometimes is interpreted as a virtual displacement of a material point due to unit virtual crack extension in that direction (x_1 for q_1).

2.2.3 Mixed mode J-Integrals

Mixed mode ERR and SIFs (K_I, K_{II}) can be calculated using Eq. 2.8 by superimposing an auxiliary stress and displacement field with the numerical solution results. This approach is basically trying the computed results from numerical solution in a

known crack-tip solution which has the formulations needed to relate the SIFs, displacements, geometry and stresses [59]. These auxiliary fields can be derived from solutions for asymptotic solutions for crack-tip such as Westergaard [144], Williams [145] or [133, 42, 44, 119] for a bi-material crack. Using superscript (1) for the numerical (actual) solution values and (2) for the auxiliary solutions, J-integral for the superimposed fields can be built:

$$J_1^{(1+2)} = \int_{\Gamma} \left[\frac{1}{2} (\sigma_{ij}^{(1)} + \sigma_{ij}^{(2)}) (\epsilon_{ij}^{(1)} + \epsilon_{ij}^{(2)}) \delta_{1j} - (\sigma_{ij}^{(1)} + \sigma_{ij}^{(2)}) \frac{\partial (u_i^{(1)} + u_i^{(2)})}{\partial x_1} \right] n_j d\Gamma \quad (2.15)$$

δ_{1j} stands for the Kronecker delta. The components of the J-integral in 2.15 can be separated according to the fields they represent:

$$J_1^{(1+2)} = J_1^{(1)} + J_1^{(2)} + I^{(1,2)} \quad (2.16)$$

$I^{(1,2)}$ is the interaction term:

$$I^{(1,2)} = \int_{\Gamma} \left[W^{(1,2)} \delta_{1j} - \sigma_{ij}^{(1)} \frac{\partial u_i^{(2)}}{\partial x_1} - \sigma_{ij}^{(2)} \frac{\partial u_i^{(1)}}{\partial x_1} \right] n_j d\Gamma \quad (2.17)$$

J-integral is related to the stress intensity factors:

$$J = \frac{K_I^2}{E^*} + \frac{K_{II}^2}{E^*} \quad (2.18)$$

where

$$E^* = \begin{cases} E & \text{plane stress} \\ \frac{E}{1-\nu^2} & \text{plane strain} \end{cases} \quad (2.19)$$

E is Young's modulus and for the laminate interface, the matrix elastic modulus is used. Eq. 2.18 for the superimposed case is written as:

$$J_1^{(1+2)} = \frac{(K_I^{(1)} + K_I^{(2)})^2}{E^*} + \frac{(K_{II}^{(1)} + K_{II}^{(2)})^2}{E^*} \quad (2.20)$$

expanding (2.20) holds:

$$J_1^{(1+2)} = J_1^{(1)} + J_1^{(2)} + \frac{2(K_I^{(1)} K_I^{(2)} + K_{II}^{(1)} K_{II}^{(2)})}{E^*} \quad (2.21)$$

now considering (2.16), the interaction term can be written as:

$$I^{(1,2)} = \frac{2(K_I^{(1)} K_I^{(2)} + K_{II}^{(1)} K_{II}^{(2)})}{E^*} \quad (2.22)$$

SIF for mode one is calculated by considering $K_I^{(2)} = 1$ and $K_{II}^{(2)} = 0$:

$$K_I^{(1)} = \frac{I^{(1,ModeI)} E^*}{2} \quad (2.23)$$

mode two SIF is calculated by putting $K_{II}^{(2)} = 1$ and $K_I^{(2)} = 0$

$$K_{II}^{(1)} = \frac{I^{(1,ModeII)} E^*}{2} \quad (2.24)$$

In order to solve $I^{(1,2)}$ numerically, an area integral is employed similar to the approach used for Eq. 2.14 this time solving the following integral over area A :

$$I^{(1,2)} = \int_A \left[\sigma_{ij}^{(1)} \frac{\partial u_i^2}{\partial x_1} \sigma_{ij}^{(2)} \frac{\partial u_i^1}{\partial x_i} - W^{(1,2)} \delta_{1j} \right] \frac{\partial q}{\partial x_i} dA \quad (2.25)$$

This approach needs a priori solution for the crack-tip stresses. The solutions for the case where the crack approaches the interface of a bimaterial orthotropic laminate -which is the case of the current chapter tests- do not have a straightforward solution and using J-Integrals for the cases where the contours intersect with bimaterial interfaces are not accurate.

2.3 Material and geometries

The material of interest in this study is a $[0/90]_s$ CFRP HexPly8552 [2] laminate with the mechanical properties presented in Table 2.3. HexPly8552 is an epoxy resin laminate containing unidirectional glass fibres mostly used in aerospace structures. The geometry of the specimen is depicted in Fig. 2.5.

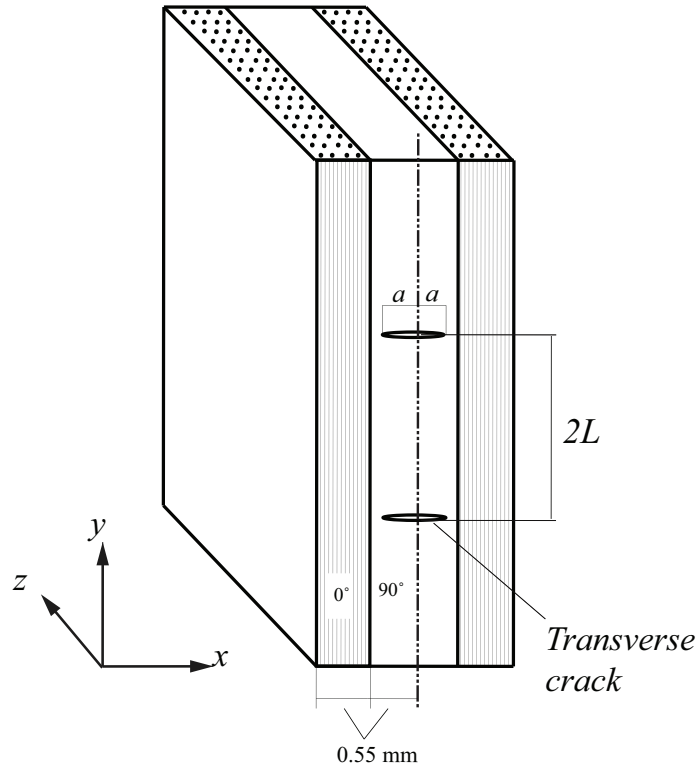


Figure 2.5: Transverse crack in $[0/90]_s$ laminate

Table 2.3 Material Properties for Hexply8552, E and G values are in GPa

Property	E_{11}	E_{22}	E_{33}	G_{12}	G_{23}	G_{13}	ν_{12}	ν_{13}	ν_{23}
value	1413	9.58	9.85	5	3.5	5	0.3	0.3	0.32

The tensile strength for fibre direction is 2207 MPa and the transversal strength is 81 MPa. The boundary conditions are described in Fig. 2.6. In the following sections, the simulation in FEM and XFEM are described separately along with the numerical procedures used for discontinuity inclusion and J-integral calculation.

2.4 FEM analysis of the problem (ABAQUS)

The specimen was created in ABAQUS standard in 2D and 3D mode and plane strain, as well as generalized plane strain (GPS) assumptions, were considered. ABAQUS offers J-integrals for plane strain condition but it is not possible to use them with GPS elements. Using the symmetry condition, half of the model in both vertical and horizontal direction is drawn. The crack was created as a free line segment at the lower edge of the material. Different crack lengths between 0 and 0.55 mm

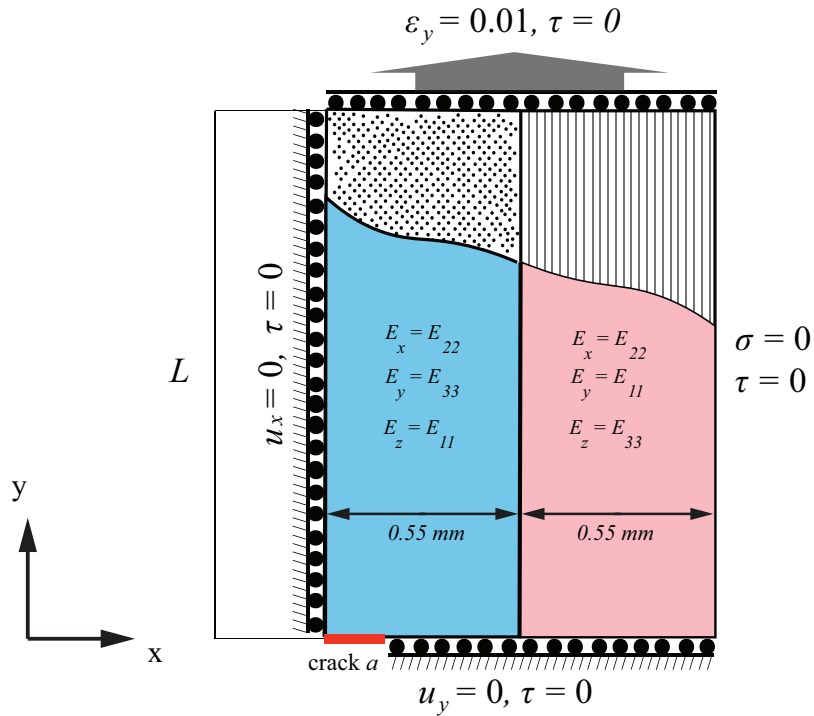


Figure 2.6: Boundary conditions

were tried in order to record mode I ERR evolution for vertical displacement loading $\epsilon = 0.01$. The initial crack length is 0.1 mm. This test was tried for four different crack separation lengths ($2L$). The model consists of two rectangles representing 0° and 90° plies. These two sides are created by means of partition tool in ABAQUS which defines the interface on the element's edge and as perfectly bonded. Material properties are defined separately for each partition as illustrated in Fig. 2.6. The materials properties were defined in all three dimensions and rotated to match the fibre orientation.

The ERR for plane strain case was calculated using four contours around the crack tip as shown in Fig. 2.7, considering the symmetric definition for the J-integral. The results for BEM is only available for GPS case and the plane strain results are used only for XFEM code verifications.

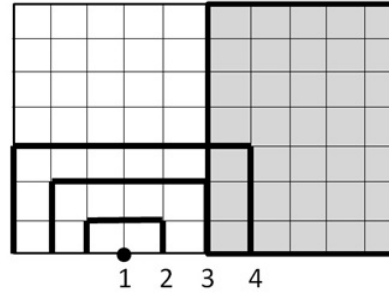


Figure 2.7: Several J-integrals were used around the crack tip for ERR calculation

ABAQUS has GPS element but the J-integral output is unavailable for this type of element and the author decided not to pursue this problem in two dimensional mode as it does not involve the J-integrals which is the subject of the study.

2.5 Three dimensional analysis for generalized plane strain in FEM

To evaluate the problem with J-integrals considering GPS, a three dimensional test was carried out in ABAQUS. In this case, the software limitation on J-integral use for GPS was avoided by including the in-plane strain as a displacement boundary condition. The crack is defined as a two dimensional free surface partition at the bottom side of the model. Material properties are the same as Table 2.3. To create strain in the thickness direction, a uniform strain of $\epsilon_{33} = -0.000381$ was applied on one side (the surface facing z axis) and zero displacement was enforced on the face on the opposite side. The results of the J-integral analysis are presented in Fig. 2.8. The results from 3D FEM closely follows the BEM results for the in-plane strain considered in the test with a very small overestimate. This difference is almost zero for when $L = 1 \text{ mm}$. This difference is influenced by the material properties definition for the shear modulus value. It should also be noted that the test for the cracks very close to the interface was only done to 0.53 since very fine mesh was needed to create contours that do not enter the second ply otherwise the results would be wrong. The value zero at $a = 0.55 \text{ mm}$ is only hypothetical and is not a result of the analysis. The ERR is assumed to drop to zero since it reaches a material with much higher fracture toughness.

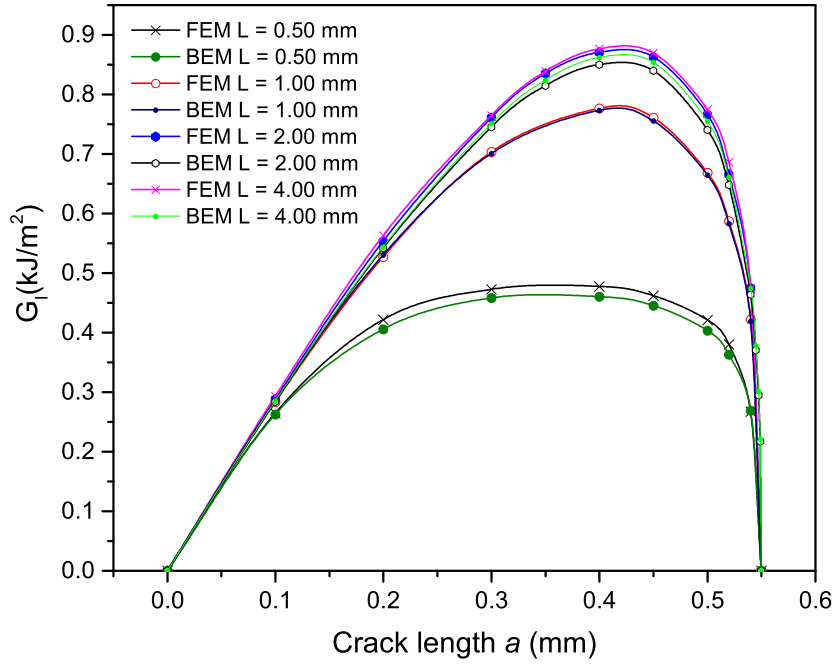


Figure 2.8: J-integral result from 3D FEM solver under $\epsilon_{33} = -0.000381$

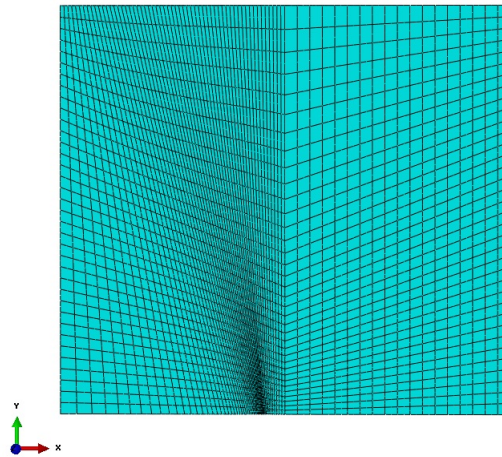


Figure 2.9: The mesh near the interface has to be refined in order to create enough elements in the 90° ply such that the J-Integral path does not enter the 0° ply

Fig. 2.9 illustrates the mesh refinement structure around the crack-tip for such condition. The energy release rate distribution for specimens larger than $L = 2\text{ mm}$ are almost similar which means the consecutive transversal cracks that are located

with a distance equal or larger than 2 mm will not interact with each other for this specimen. According to the present results, the energy release rate goes toward zero when the crack approaches the interface which means it will stop propagating. This is because the crack approaches the 0° ply which has large stiffness in the perpendicular direction to the crack line. The transverse crack might freeze at this point but other mechanisms of fracture can be triggered by the transversal crack [25]. For example, the stresses caused by this crack normal to the interface can lead to delamination before the crack reaches the interface.

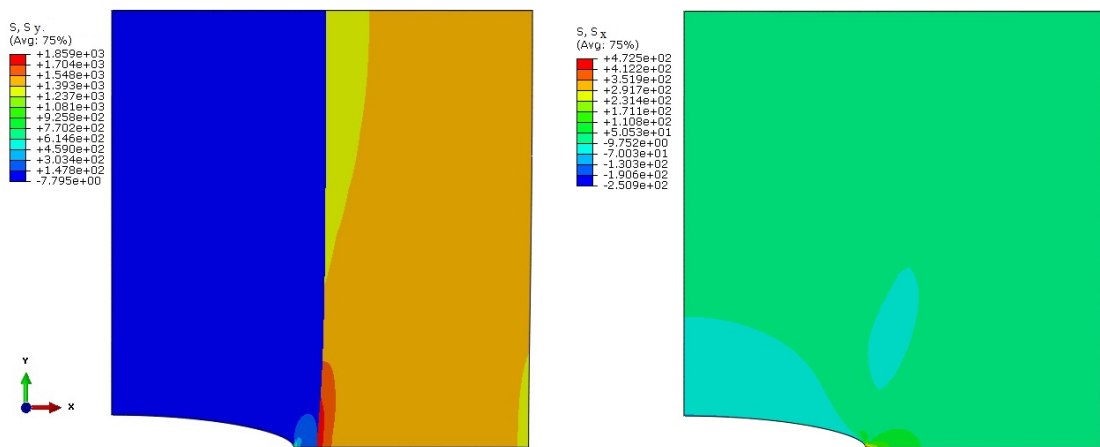


Figure 2.10: σ_x and σ_y distribution for $a = 0.50\text{ mm}$

Figure 2.10 shows the stress distribution on the laminate cross sections. σ_x around the crack-tip reaches magnitudes much higher than the what material can stand. The normal stress at the interface increases as the crack-tip approaches the interface. Since the energy release rate drops to zero at the interface, presumably the crack has frozen before it reaches the interface. Depending on the interface stress levels at this point, delamination is a possibility. The current setting only considers one crack in the domain and further analysis of the crack considering delamination was not carried out.

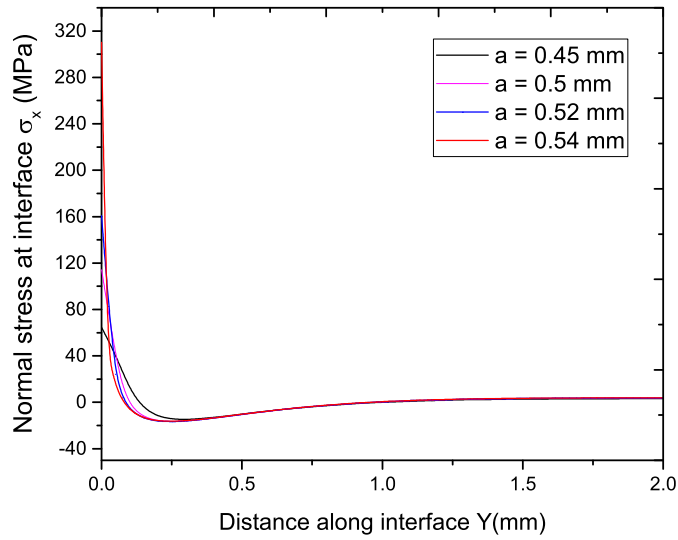


Figure 2.11: Normal stress at the interface for $L = 2 \text{ mm}$.

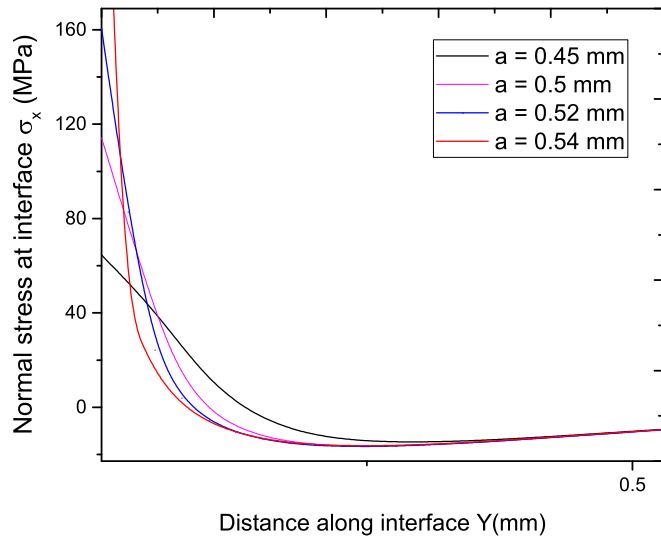


Figure 2.12: Normal stress at the interface ahead of the crack for $L = 2 \text{ mm}$ (zoom)

For a better representation of the stress state at the interface, normal and shear stresses are plotted in Figs. 2.11, 2.12 and Fig. 2.13. In the case of normal stress σ_{xx} , it can be observed that the stresses increase significantly over a very small crack

growth when the crack-tip is very close to the interface. Again it should be reminded that the energy release rate drops significantly near the interface and theoretically the crack would have had arrested before reaching these points. The results of these plots are taken from a path defined on the interface of the model in ABAQUS and are in good agreement with the results of [104]. However, some oscillations were observed in the shear stress plot 2.13. These oscillations are due to the finite element approximation error at the element edges.

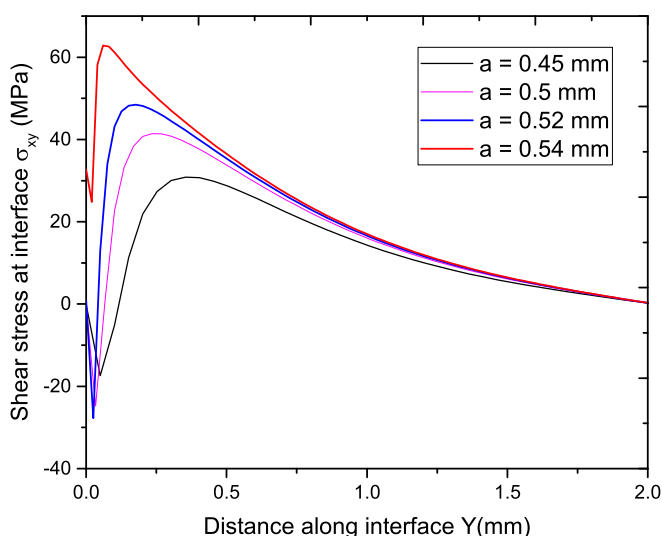


Figure 2.13: J-integral result from XFEM solver and BEM results

2.6 XFEM analysis of the problem

The test for the transversal crack in the $[0/90]_s$ was repeated in XFEM code (MATLAB). This analysis was carried out in 2D plane strain condition and the results are compared with ABAQUS results in order to verify the code's outputs and the energy release rate calculated from the J-integrals. This code is an XFEM solver with isotropic stiffness matrix written by M. Pais [103] and has the capability to model strong and weak discontinuities as well as inclusions. At this stage, the stiffness matrix subroutine of the code was upgraded to handle heterogeneous materials and this analysis is used to verify the new stiffness matrix. In the next section, the formulation

and discretization of the displacement field with inclusions, crack discontinuity and the crack-tip enrichments are described.

2.6.1 Problem formulation and discretization

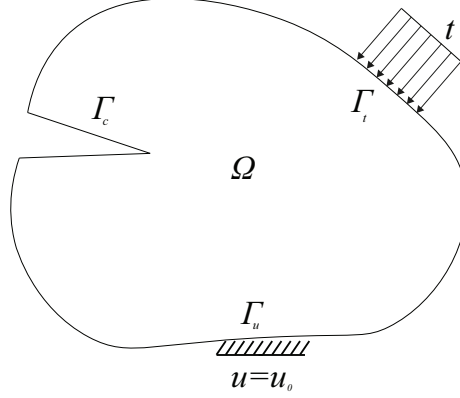


Figure 2.14: A body in equilibrium state

Consider body Ω confined in boundary Γ that contains discontinuities (Fig. 2.14). The governing equations are :

$$\nabla \boldsymbol{\sigma} + \mathbf{f}^b = 0 \quad \text{on } \Omega \quad (2.26)$$

with the following boundary conditions:

$$\boldsymbol{\sigma} \cdot \mathbf{n} = \mathbf{t} \quad \text{on } \Gamma_t \quad (2.27)$$

$$\mathbf{u} = \bar{\mathbf{u}} \quad \text{on } \Gamma_u \quad (2.28)$$

and

$$\boldsymbol{\sigma} \cdot \mathbf{n} = 0 \quad \text{on } \Gamma_c \quad (2.29)$$

The boundary value problem in variational form is:

$$\int_{\Omega} \boldsymbol{\sigma} \cdot \delta \boldsymbol{\epsilon} d\Omega = \int_{\Omega} \mathbf{f}^b \cdot \delta \mathbf{u} d\Omega + \int_{\Gamma} \mathbf{t} \cdot \delta \mathbf{u} d\Omega \quad (2.30)$$

The displacement field for XFEM writes (see 1.7.4.1):

$$\mathbf{u}(\mathbf{x}) = \sum_{i=1}^{n_{stn}} N_i(\mathbf{x}) \mathbf{u}_i + \sum_{j=1}^m \sum_{k=1}^{n_{enr}} N_k(\mathbf{x}) P^j(\mathbf{x}) \mathbf{a}_k^j \quad (2.31)$$

\mathbf{a}^j show the degrees of freedom for each type of enrichment. Here three types of enrichments are considered; $\mathbf{a} = \mathbf{a}^1$ for the crack discontinuity, $\mathbf{b} = \mathbf{a}^2$ for the crack-tip enrichment and $\mathbf{c} = \mathbf{a}^3$ for the inclusion enrichment. By using Eq. 2.31 and its derivatives in Eq. 2.30 along with the constitutive stress-strain law, the equilibrium can be written in discrete system of linear equilibrium equations:

$$\mathbf{K}\mathbf{U} = \mathbf{f} \quad (2.32)$$

\mathbf{K} is the stiffness matrix and \mathbf{U} contains standard and enriched degrees of freedom. \mathbf{f} is the force vector:

$$\mathbf{K}_{ij}^e = \begin{bmatrix} K_{ij}^{\mathbf{u}\mathbf{u}} & K_{ij}^{\mathbf{u}\mathbf{a}} & K_{ij}^{\mathbf{u}\mathbf{b}} & K_{ij}^{\mathbf{u}\mathbf{c}} \\ K_{ij}^{\mathbf{a}\mathbf{u}} & K_{ij}^{\mathbf{a}\mathbf{a}} & K_{ij}^{\mathbf{a}\mathbf{b}} & K_{ij}^{\mathbf{a}\mathbf{c}} \\ K_{ij}^{\mathbf{b}\mathbf{u}} & K_{ij}^{\mathbf{b}\mathbf{a}} & K_{ij}^{\mathbf{b}\mathbf{b}} & K_{ij}^{\mathbf{b}\mathbf{c}} \\ K_{ij}^{\mathbf{c}\mathbf{u}} & K_{ij}^{\mathbf{c}\mathbf{a}} & K_{ij}^{\mathbf{c}\mathbf{b}} & K_{ij}^{\mathbf{c}\mathbf{c}} \end{bmatrix} \quad (2.33)$$

$$\mathbf{U} = \{\mathbf{u} \ \mathbf{a} \ \mathbf{b}1 \ \mathbf{b}2 \ \mathbf{b}3 \ \mathbf{b}4 \ \mathbf{c}\}^T \quad (2.34)$$

$$\mathbf{f}_i^e = \{\mathbf{f}_i^{\mathbf{u}} \ \mathbf{f}_i^{\mathbf{a}} \ \mathbf{f}_i^{\mathbf{b}1} \ \mathbf{f}_i^{\mathbf{b}2} \ \mathbf{f}_i^{\mathbf{b}3} \ \mathbf{f}_i^{\mathbf{b}4} \ \mathbf{f}_i^{\mathbf{c}}\}^T \quad (2.35)$$

The crack jump and inclusion/void enrichments adds two degrees of freedom per node while the crack-tip enrichment uses eight extra degrees of freedom for each node in a two dimensional case. The components of the stiffness matrix are calculated by integrating the following integral over the element using Gauss quadrature rule:

$$\mathbf{K}_{ij}^{\alpha\beta} = \int_{\Omega_e} (\mathbf{B}_i^\alpha)^T \mathbf{D} (\mathbf{B}_i^\beta) d\Omega \quad (\alpha, \beta = \mathbf{u}, \mathbf{a}, \mathbf{b}, \mathbf{c}) \quad (2.36)$$

It should be noted that the crack jump and the weak discontinuity enrichments cannot be used together on the same node [95]. \mathbf{B}_i are the derivative matrix of the shape functions:

$$\mathbf{B}_i^{\mathbf{u}} = \begin{bmatrix} N_{i,x} & 0 \\ 0 & N_{i,y} \\ N_{i,y} & N_{i,x} \end{bmatrix} \quad (2.37)$$

$$\mathbf{B}_i^{\mathbf{a}} = \begin{bmatrix} (N_i, \Upsilon(\zeta, \eta))_{,x} & 0 \\ 0 & (N_i \Upsilon(\zeta, \eta))_{,y} \\ (N_i \Upsilon(\zeta, \eta))_{,y} & (N_i \Upsilon(\zeta, \eta))_{,x} \end{bmatrix} \quad (2.38)$$

Υ is the shifted enrichment function as described in Eq. 1.19. For the crack-tip enrichment, \mathbf{B} needs to be calculated four times (for four base functions of the asymptotic enrichment) over each Gauss point:

$$\mathbf{B}_i^{\mathbf{b}} = [\mathbf{B}_i^{\mathbf{b}1} \ \mathbf{B}_i^{\mathbf{b}2} \ \mathbf{B}_i^{\mathbf{b}3} \ \mathbf{B}_i^{\mathbf{b}4}] \quad (2.39)$$

and

$$\mathbf{B}_i^\alpha = \begin{bmatrix} (N_i F_\alpha)_{,x} & 0 \\ 0 & (N_i F_\alpha)_{,y} \\ (N_i F_\alpha)_{,y} & (N_i F_\alpha)_{,x} \end{bmatrix} \quad \alpha = 1, 2, 3, 4 \quad (2.40)$$

F_α are functions of r (distance to the crack-tip) and the trigonometric functions of the crack angle θ (see Eq. 1.21). Finally for the weak discontinuities, the enrichment function described in Eq. 3.26 is multiplied and differentiated as:

$$\mathbf{B}_i^c = \begin{bmatrix} (N_i \Psi(\zeta, \eta))_{,x} & 0 \\ 0 & (N_i \Psi(\zeta, \eta))_{,y} \\ (N_i \Psi(\zeta, \eta))_{,y} & (N_i \Psi(\zeta, \eta))_{,x} \end{bmatrix} \quad (2.41)$$

and the force vector writes:

$$\mathbf{f}_i^u = \int_{\Gamma_t} N_i \mathbf{t} d\Gamma + \int_{\Omega^e} N_i \mathbf{f}^b d\Omega \quad (2.42)$$

$$\mathbf{f}_i^a = \int_{\Gamma_t} (H_{GP} - H_i) N_i \mathbf{t} d\Gamma + \int_{\Omega^e} N_i (H_{GP} - H_i) \mathbf{f}^b d\Omega \quad (2.43)$$

$$\mathbf{f}_i^{\mathbf{b}\alpha} = \int_{\Gamma_t} N_i (F_\alpha - F_{\alpha_i}) \mathbf{t} d\Gamma + \int_{\Omega^e} N_i (F_\alpha - F_{\alpha_i}) \mathbf{f}^b d\Omega, \quad \alpha = 1, 2, 3, 4 \quad (2.44)$$

$$\mathbf{f}_i^c = \int_{\Gamma_t} N_i P \mathbf{t} d\Gamma + \int_{\Omega^e} N_i P \mathbf{f}^b d\Omega \quad (2.45)$$

$$(2.46)$$

2.6.2 Selection of the nodes to enrich

In XFEM only the nodes near the crack are enriched in order to reduce the computation that would take place if all the domain was enriched. The selection process is easily done by considering a distance to the discontinuity to seclude the elements that are in a distance range shorter than $(\sqrt{2} + 0.05)l_e$ (l_e is the size of the element side) which is slightly longer than the longest distance between two nodes in a 4 node quadrilateral element.

2.6.3 Results of XFEM analysis

The results for the XFEM model with $l_e = 0.01 \text{ mm}$ element size and ABAQUS J-Integral solution are depicted in Fig. 2.15. Here also the initial crack length is 0.1 mm. The ERR from both simulations follow each other closely. Again the results for $a = 0.55 \text{ mm}$ for ABAQUS is a projection of previous results and are not numerically

possible due J-integral limitations. For XFEM, in spite very fine mesh was used, it can be seen that the results diverge when the crack is near the interface. Apparently in XFEM a problem similar to FE analysis exists where the area integral is extended across the interface between the plies. Besides, the enrichments can cause more trouble since they modify the stress/displacement field which is not compatible with the formulations of the J-Integral described in section 2.2.3. The crack-tip enrichment was not used in this test and the impacts of it are described in the following section.

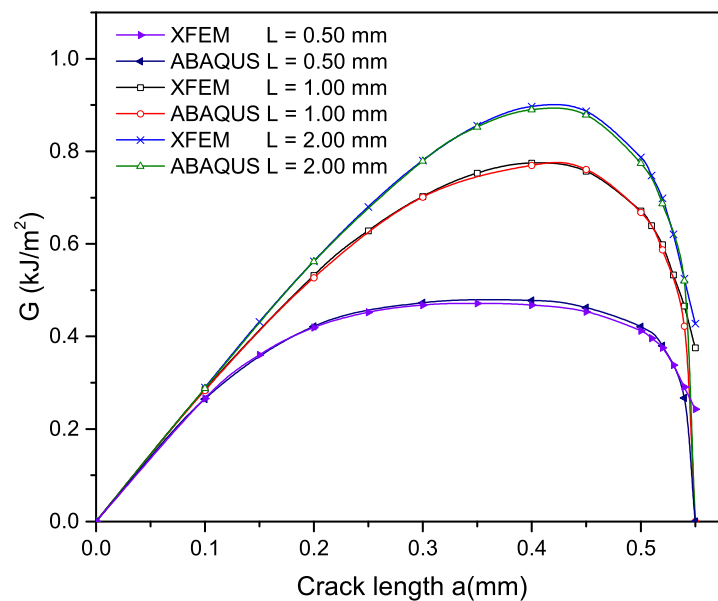


Figure 2.15: Comparison of results from ABAQUS and MATLAB XFEM code. Element length for XFEM cases were 0.01mm (55 elements in thickness direction of each ply)

2.7 The crack-tip asymptotic field effect

In FEM and XFEM, the element that contains the crack tip, as well as the surrounding elements, are not capable of fully capturing the displacement field that contains a singularity if standard first or second order shape functions are used. In order to capture the singularity, the shape function must be able to produce infinity in the strain field. A \sqrt{r} (with r being the distance to the crack-tip) is capable of producing such fields.

There are techniques in FEM and XFEM in order to produce these behaviours. ABAQUS provides crack-tip quarter point element for the singularity in the J-integral settings. In this case, since the crack does not enter the elements and always located on the element border, the crack-tip is always an edge node of an element. The quarter-point element has a mid-side node on each ligament and by shifting this node toward the crack-tip the singularity is produced. The effect of this modification was tested by the author to find the effect of it on the results of the J-Integrals. The test was carried out using four contours.

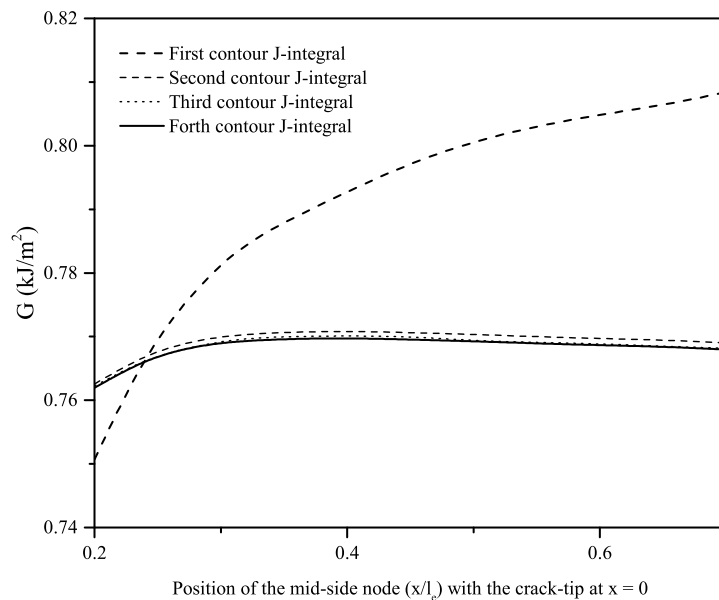


Figure 2.16: Variation of the J-integral due change in the location of the mid-side node. The contours are depicted in Fig. 2.7

As it can be seen in Fig. 2.16, the technique affects the first contour the most, which is the immediate contour around the crack-tip. The result of this contour is closest to the answer when the mid-side node is about a quarter of the element size away from the tip. However, The result of the first contour is not recommended by ABAQUS since it is sensitive to factors such as the mesh size [35]. In conclusion, it seems that this correction is not of much importance when it comes to the J-integrals energy release rate calculations since as it can be seen from the Fig. 2.16,

with or without quarter point element, the first contour is better to be omitted. In the case of XFEM, it is possible to create the necessary shape functions for the singularity by involving functions that again, can produce a singular field. In addition, the trigonometric base functions (1.21) are also borrowed from the asymptotic field solutions [145, 66] to provide correction for the crack opening jump.

Here another test was carried out in order to clarify the effect of the crack-tip enrichment on the energy release rate results. This test was done for the same two dimensional example used throughout this chapter and plane strain assumption applies. Although the J-integral shows little mesh dependency for small cracks inside the transversely isotropic ply, the results show that the crack-tip enrichment actually worsens the energy release rate evaluation for cracks near the interface. For $l_e = 0.05 \text{ mm}$ there are 11 elements in the 90° ply. It was observed that after $a = 0.4 \text{ mm}$ the results for crack-tip with and without enrichment suffer from fluctuation. This problem is more dominant with enriched crack-tip elements. The J-Integral uses elements further than the third layer of elements which means for the cracks further than $a = 0.45 \text{ mm}$ the area integral has overlapped with the second ply which explains the fluctuation. This effect in the enriched case is worse since there is a singular field and larger stress gradients might be present. By increasing the element numbers the results improves for both cases, although the crack-enrichment still demonstrate excessive ERR for the cracks very close to the interface.

2.8 Conclusion

An extensive study on the J-Integrals in FEM and XFEM was carried out in this chapter in order to assess its credibility for the composite material simulation. A path-independent J-Integral that uses arbitrary paths around the crack-tip shows difficulty calculating the energy release rate for non-homogeneous materials which is a disadvantage compared to other methods such as VCCT. The study showed that for area integrals that use a priori solution for the ERR evaluation, the results are accurate until an analytical solution exists and the displacement field is accurately defined. For a crack that approaches an interface, the current implementation of the J-Integral is only reliable as long as it is confined within one material. The MATLAB code was upgraded in order to calculate the orthotropic stiffness matrix

and the results were compared with those of ABAQUS simulation. It became clear that the asymptotic crack-tip enrichment does not improve the ERR results and when it comes to heterogeneous materials, it actually worsens the outcome. For composite structures, a more robust technique is required that is not influenced by the material interfaces.

Chapter 3

Cohesive zone model for delamination analysis in XFEM

3.1 Introduction

In this chapter, the implementation of a thermodynamically based cohesive zone model in XFEM is covered in details. In order to numerically define the cohesive zone in XFEM, cohesive forces and stiffness have to be applied where the discontinuity is created by the XFEM extra degrees of freedom. In this way, instead of having zero crack surface tractions, there are cohesive forces resisting the crack opening at the vicinity of the crack-tip. The cohesive forces act as internal forces but since they are a function of the crack opening displacement, the equilibrium equation is solved iteratively to take account for this non-linearity. A Newton-Raphson solver is developed in MATLAB and the orthotropic stiffness matrix subroutine from chapter two is modified to integrate the cohesive zone stiffness. A subroutine for the calculation of J-Integrals in CZM is created along with the damage and cohesive force subroutines. For the Level Sets, as well as the connectivity and post-processing, the subroutines from XFEM code by M.Pais [103] are used with some modifications.

The developed solver can operate in both load and displacement controlled modes. Several DCB models are used to carry out delamination tests and the results are compared to other researchers numerical and experimental results. One of the benefits of the present CZM model is that the traction-separation law used here only represent the damaged material. Although this is not an issue for delamination modelling, including the undamaged material in the cohesive zone would require enrichment of

undamaged elements in XFEM and assumption that the crack is going to extend in that direction.

3.2 Background

Cohesive zone models are used to model the crack-tip when the material in the crack-tip vicinity acts non-linear. These models are mostly applied when the fracture process zone is not negligible in comparison to the crack length. This is usually observed in composites as quasi-brittle materials. The concept of a crack process zone was introduced by Dugdale [40] in 1960 who considered a plastic zone at the crack-tip with the maximum stresses limited to the material's yield stress. In his model, the stresses in this plastic zone are equal to the yield strength. Hillerborg et al. [61] proposed a model based on Barenblatt [15] cohesive crack in which the stress is not constant and is a function of the crack opening. The stress is equal the yield strength at the crack-tip and gradually decreases from τ_0 to zero at λ_c (Fig. 3.1).

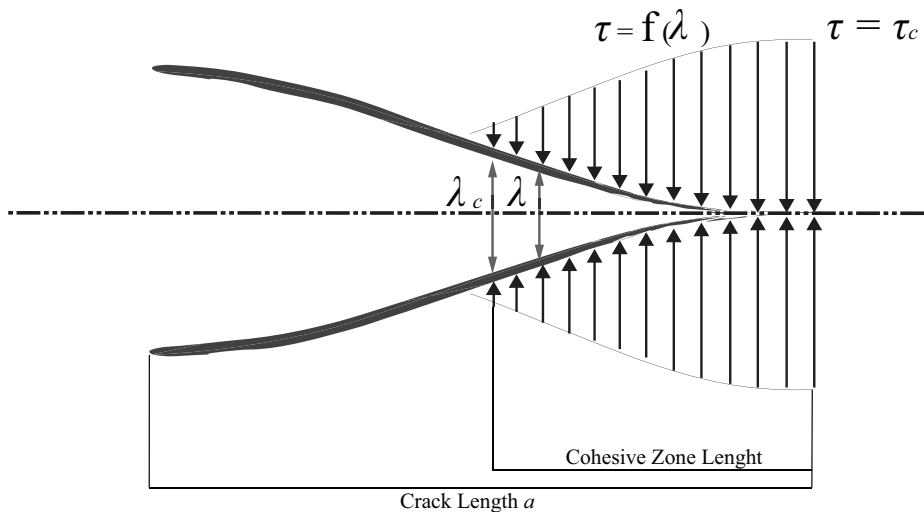


Figure 3.1: Hillerborg cohesive zone model

Numerous types of cohesive zone models have been developed in the past few decades to deal with a variety of fracture problems. Figure 3.2 illustrates some variations of CZM models. In 1990, Needleman developed a model with two curves, one exponential for the normal traction and a polynomial for the shear traction. A trapezoidal model was proposed by Tvergaard and Hutchinson [138] for crack growth in

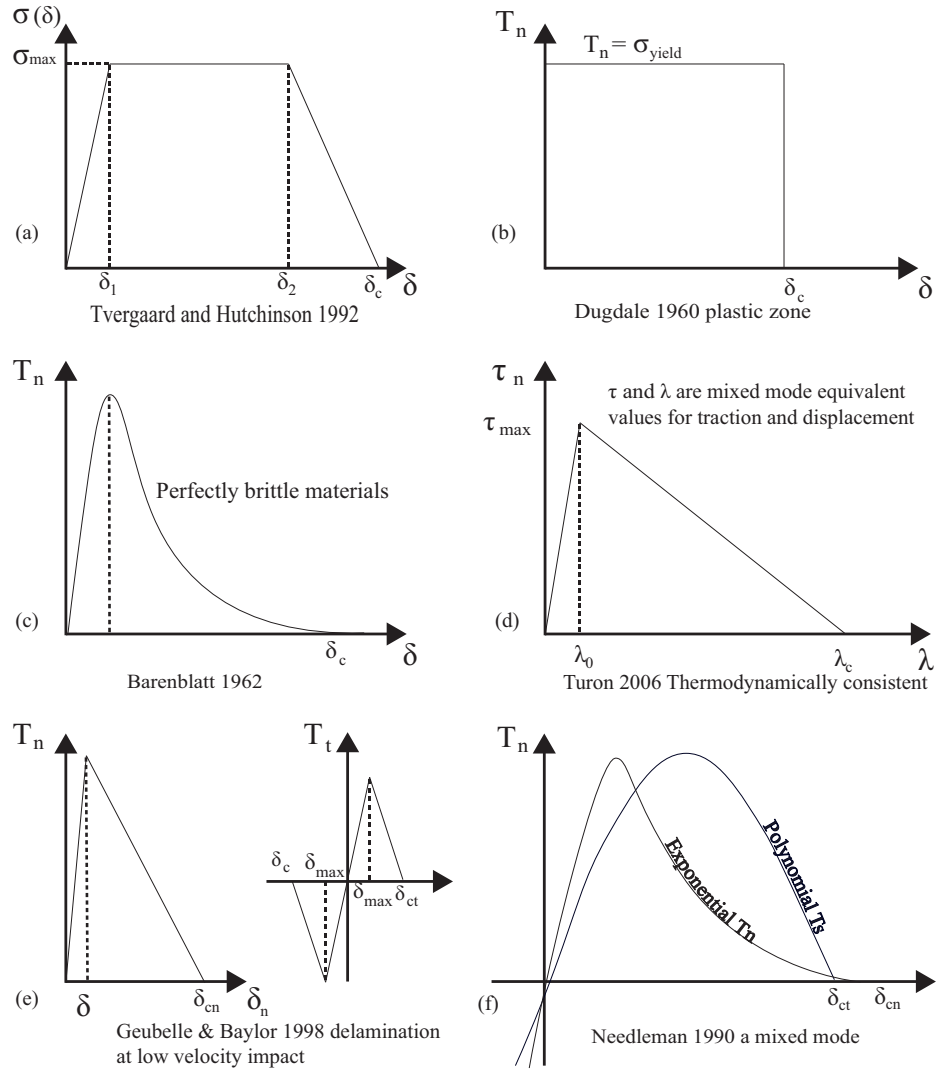


Figure 3.2: Cohesive zone models take variety of shapes.

elasto-plastic material and peeling of adhesive joints. Xu and Needleman [147] developed another exponential set of cohesive laws while separating the two opening modes.

3.3 Energy balance in CZ

The energy absorbed per unit area of the crack from zero to λ crack opening is:

$$G = \int_0^\lambda \tau d\lambda \quad (3.1)$$

This energy is equivalent to the surface area under the traction-separation curve. The formula that defines the relation between the crack opening and the traction is regarded as the Traction-Separation Law (TSL). The maximum energy dissipated by the cohesive zone happens when the CZM is fully developed. That is when the stress starts from τ_0 at the tip and gradually reduces to zero at λ_c . In that case, the energy is equal to the entire area under the traction-separation locus and for the displacements larger than λ_c new traction-free crack surfaces are created. This energy is equal to the critical ERR for the material. Fig. 3.3 illustrates two different TSLs; the one on the left is for the interface that has already entered the degradation process; for the TSL on the right, both undamaged (before λ_y) and damaged materials are governed by the TSL. λ_y is the displacement at yield.

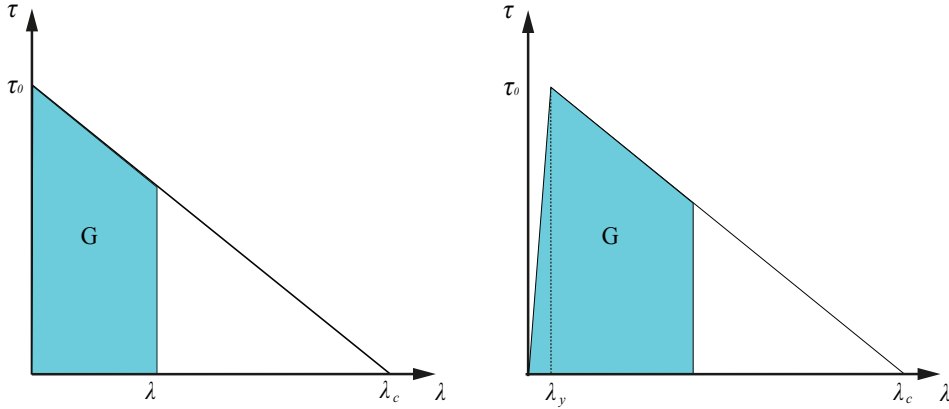


Figure 3.3: Cohesive zones with no undamaged zone. This model only applies to the material that has entered the degradation process. (left) and model with undamaged zone before yielding at λ_y (right). The material acts elastically in the region between zero and λ_y

XFEM implementation for the current study uses the TSL without the undamaged section since the aim is to use the FEA standard stiffness matrix for the undamaged elements. If the cohesive zone elements include the undamaged material, this means that the crack path is already chosen before the damage process started. This small modification will cause significant changes to the numerical implementation regarding the crack growth process.

CZM has been implemented in XFEM for many crack simulations. Wells and Sluys [143] proposed an approach for a cohesive zone model in XFEM by using step function

to create a discontinuity in the displacement field. They used an exponential form of the TSL which also does not include the undamaged part. Moës and Belytschko [93] developed the crack-tip enrichment function based on the asymptotic solution for the cohesive zone. In this case, the base functions for the enrichments include $r^m \sin(\theta/2)$ terms. Zi and Belytschko [155] provided new enrichments based on sign function to avoid problems caused by Heaviside enrichments when it comes to blending into the standard finite element domain. Mariani and Perego [89] developed higher order enrichment functions to produce an improved cubic displacement discontinuity which required 4 extra degrees of freedom per node. Remmers et al. [114] developed cohesive segment method in which the crack was presented as a set of overlapping cohesive segments and made it possible to have cohesive cracks on arbitrary locations and orientations. Higher-order asymptotic field base functions were put to test by Zamani et al. [152] for both linear and non-linear cohesive laws.

One important issue with mixed mode cohesive laws is the energy restoration and that the model should satisfy the Clausius-Duhem inequality [135]. For example, consider the cohesive zone has fully extended under normal displacement at the crack-tip. If suddenly the loading mode switch to mode II, the damage variable will predict higher load for a material that has failed under mode I loading (Fig. 3.4).

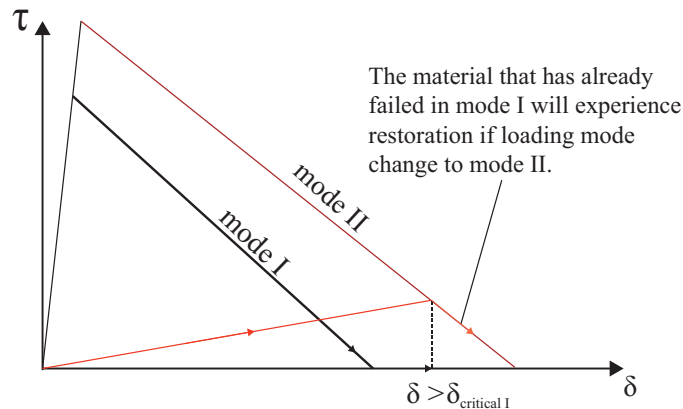


Figure 3.4: The restoration of the cohesive force as a result of changing loading mode.

3.4 CZM for mixed mode delamination

A damage model for mixed mode crack opening is constructed here for the cohesive zone. First, the boundary value problem and the kinematics of the cohesive crack

needs to be defined and then the constitutive formulation for the CZ is provided.

Kinematics of the discontinuous field

The displacement field of a cracked body Ω can be decomposed into continuous and discontinuous parts:

$$\mathbf{u}(x) = \hat{\mathbf{u}} + H_{\Gamma_d} \llbracket \mathbf{u} \rrbracket \quad (3.2)$$

\mathbf{u} and $\hat{\mathbf{u}}$ are both continuous on Ω and H is the Heaviside function. The discontinuous displacements $\llbracket \mathbf{u} \rrbracket \in \Gamma_c$ creates the jump in the displacement domain which is later used for the calculation of cohesive traction forces at that point. By taking the derivative of Eq. 3.2 the strain fields writes [143]:

$$\boldsymbol{\epsilon} = \nabla^s \hat{\mathbf{u}} + H_{\Gamma_c} (\nabla^s \llbracket \mathbf{u} \rrbracket) + (\nabla H_{\Gamma_c} \times \llbracket \mathbf{u} \rrbracket)^s \quad (3.3)$$

$$= \nabla^s \hat{\mathbf{u}} + H_{\Gamma_c} (\nabla^s \llbracket \mathbf{u} \rrbracket) + \delta_{\Gamma_c} (\llbracket \mathbf{u} \rrbracket \times \mathbf{n})^s \quad (3.4)$$

δ_{Γ_d} is the Dirac-delta placed at the discontinuity and the normal vector to the discontinuity is shown by \mathbf{n} . In order to calculate the normal and tangent displacements at the crack surfaces, a transformation from the global displacement to the crack coordinates is required. The crack coordinates are placed on the crack-tip with its first and second axis aligned with the tangent and normal directions of the discontinuity respectively. The global displacements are rotated by the angle the crack makes with the global coordinates (Fig. 3.5) to find the relative displacements at the crack surface:

$$\boldsymbol{\delta} = \mathbf{R}(\theta)(\mathbf{u}_c^+ - \mathbf{u}_c^-) = \mathbf{R}(\theta)(H^+ \llbracket \mathbf{u} \rrbracket^+ - H^- \llbracket \mathbf{u} \rrbracket^-) \quad (3.5)$$

\mathbf{R} is the rotation tensor and $\boldsymbol{\delta}$ is the relative displacement vector:

$$\boldsymbol{\delta} = \begin{bmatrix} \delta_t \\ \delta_n \end{bmatrix} \quad (3.6)$$

δ_t and δ_n are local displacement components tangent and normal to the crack surface.

3.4.1 Constitutive Law for the CZ

The cohesive law relates the cohesive forces to the crack opening displacement $\boldsymbol{\delta}$:

$$\boldsymbol{\tau} = \boldsymbol{\tau}(\boldsymbol{\delta}) \quad (3.7)$$

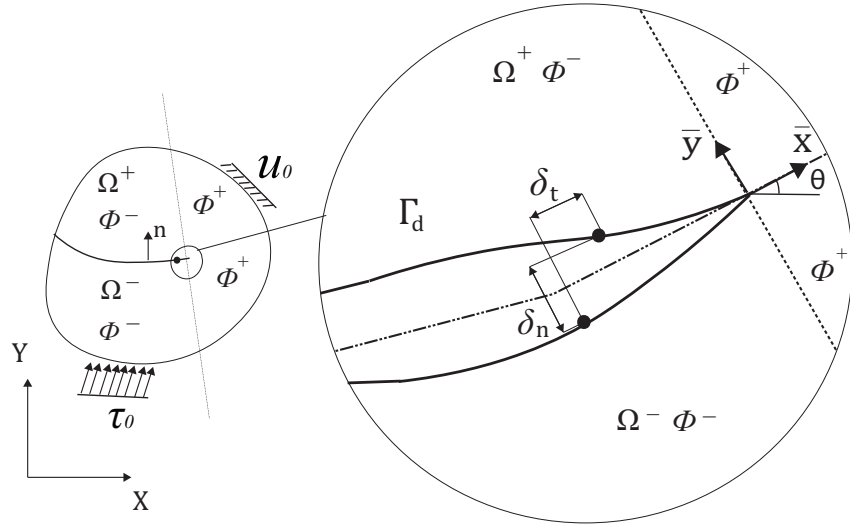


Figure 3.5: Local crack coordinate. Φ defines whether the material is before normal to the crack tip or after.

$\llbracket \mathbf{u} \rrbracket$ is the displacement jump defined in Eq. 3.2. The cohesive formulation presented here is a two dimensional linear model based on the damage mechanics approach. Scalar damage variable D is defined as the ratio of the damaged surfaces areas A_D to the total initial area A [73]:

$$D = \frac{A_D}{A} \quad (3.8)$$

Zero damage represents intact material and $D = 1$ is when the material has completely lost its load-bearing capacity. This ratio is analogous to the ratio of the dissipated energy G_D due to the creation of the damaged area to the critical energy release rate G_c which is the dissipation of energy required for full failure of the material from no damage status Fig. 3.6.

$$D = \frac{G_D}{G_c} \quad (3.9)$$

In order to develop a mixed mode cohesive law, an equivalent displacement [135] is used:

$$\lambda = \sqrt{\langle \delta_n \rangle^2 + (\delta_s)^2} \quad (3.10)$$

$\langle \cdot \rangle$ is the MacAuley brackets that ensure the negative displacement (material inter-section with itself) does not happen [136]. In the traction-separation law (Fig. 3.6) the dissipated energy is depicted in blue. The cohesive force can be calculated from

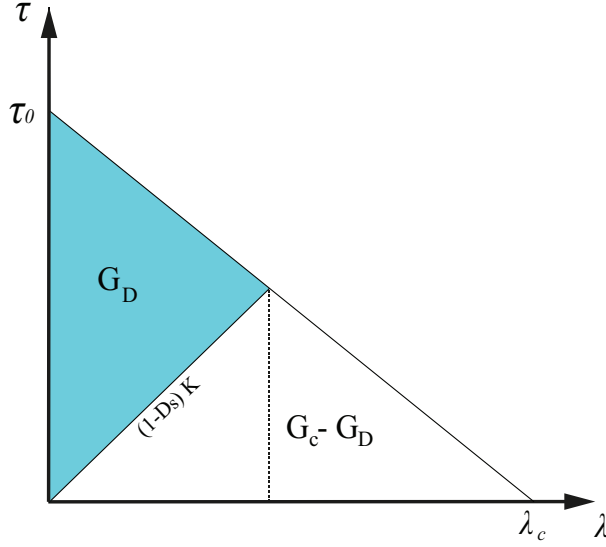


Figure 3.6: Softening law for the cohesive forces

the damage:

$$\tau(\lambda) = \tau_0(1 - D(\lambda)) \quad (3.11)$$

It should be noted that the damage used here is not the same as D_s as depicted in Fig. 3.6. It is possible to use Eq. 3.11 for the calculation of the tangent stiffness which is similar to [93, 143]. In that case, the load reduction follows the softening path that has a negative tangent stiffness matrix and the damage is not used to change the slope of the tangent stiffness in $(1 - D_s)K$ style as in [135]. This will lead to a purely inelastic model at the discontinuity [77]. So in the case of unloading, another tangent stiffness starting from the origin with the slope correspondent to the damage status is required. The relation between D_s and D is:

$$D_s = D \frac{\lambda_c \tau_0}{\lambda^2} \quad (3.12)$$

This type of stiffness is not very stable in FE platform and using D_s and a penalty stiffness K is preferred. The mixed mode quasi-static damage model presented here is defined as an equivalent one dimensional cohesive law in which both tangent and normal displacements contribute to a single damage variable. This link between the damages caused by different opening modes in non-damage based approaches such as [143] is preserved by linking the shear cohesive formula to the normal displacement.

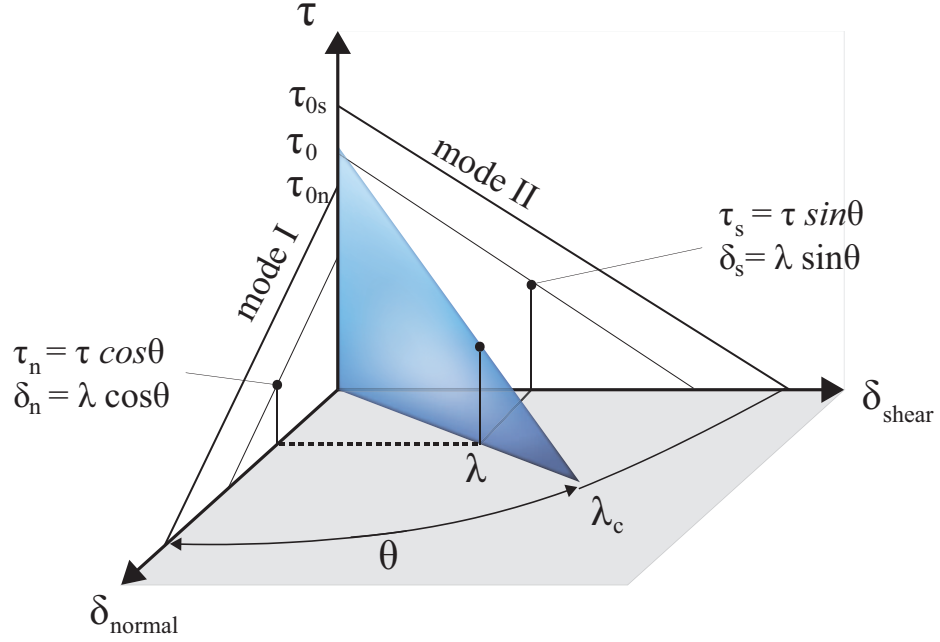


Figure 3.7: The equivalent mixed mode traction-separation law

A three dimensional representation of the 2D cohesive law is presented in Fig. 3.7. The mode mix ratio β is defined as:

$$\beta = \frac{\delta_s}{\delta_s + \delta_n} \quad (3.13)$$

For the equivalent traction separation, the equivalent critical displacement λ_c is calculated as below:

$$\lambda_c = 2 \frac{G_c}{\tau_0} \quad (3.14)$$

G_c is the equivalent critical energy release rate and τ_0 is the maximum equivalent traction. G_c is usually considered as the propagation criterion for the mixed-mode loading. When the energy release rate exceeds this critical value the crack will propagate. For the calculation of the mixed-mode energy release rate Benzeggagh-Kenane criterion [21, 76] is employed for the mix-mode ratio defined in (3.13):

$$G_c = G_{Ic} + (G_{IIc} - G_{Ic})B^\alpha \quad \text{where} \quad B = \frac{\beta^2}{2\beta^2 - 2\beta + 1} \quad (3.15)$$

α has to be found by experiment [14]. Finally the tractions are calculated:

$$\tau_0 = \sqrt{(\tau_{0n})^2 + [(\tau_{0s})^2 - (\tau_{0n}^2)]B^\alpha} \quad (3.16)$$

and

$$\tau_n = \tau_0(1 - D)(\sqrt{1 - B}) = \tau(\sqrt{1 - B}) = \tau \cos(\theta) \quad (3.17)$$

$$\tau_s = \tau_0(1 - D)(\sqrt{B}) = \tau(\sqrt{B}) = \tau \sin(\theta) \quad (3.18)$$

3.4.2 Governing equations of a cracked body and variational formulation

Crack Γ_c is in the domain Ω with displacement and traction boundary conditions \mathbf{u}_0 and \mathbf{t} at Γ_u and Γ_τ (Fig. 3.8). The cohesive zone is depicted as Γ_{coh} and traction forces τ^+ and τ^- act on Γ_{coh} . The equilibrium of body forces and boundary conditions are:

$$\nabla^s \boldsymbol{\sigma} + \mathbf{f}_i^b = 0 \quad \text{on } \Omega \quad (3.19)$$

$$\boldsymbol{\sigma} \cdot \mathbf{n}_{\Gamma_t} = \mathbf{t} \quad \text{on } \Gamma_t \quad (3.20)$$

$$\boldsymbol{\sigma} \cdot \mathbf{n}_{\Gamma_c} = \boldsymbol{\tau}_c \quad \text{on } \Gamma_{coh} \quad (3.21)$$

$$\mathbf{u} = \mathbf{u}_0 \quad \text{on } \Gamma_u \quad (3.22)$$

∇ is the gradient operator and \mathbf{f}_i^b represent body forces. In all the problems in this work the body forces are neglected. The constitutive relation for linear elastic material is $\boldsymbol{\sigma} = \mathbf{C}\boldsymbol{\epsilon}$. The cohesive traction $\boldsymbol{\tau}_c$ is function of displacement as described in section 3.4.1.

3.4.2.1 Discretization

To derive the weak form of the partial differential equation (Eq. 3.19), the equilibrium equation is multiplied by an admissible test function $\delta \mathbf{u}(\mathbf{x}, t)$ and integrated over Ω [77].

$$\int_{\Omega} \delta \mathbf{u}(\mathbf{x}) : \nabla^s \boldsymbol{\sigma} d\Omega = 0 \quad (3.23)$$

\mathbf{u} are admissible displacement variations. It is possible to use the same displacement space described in Eq. 3.2 for the admissible test function:

$$\delta \mathbf{u}(\mathbf{x}) = \delta \hat{\mathbf{u}}(\mathbf{x}) + H_{\Gamma_c} \llbracket \delta \mathbf{u}(\mathbf{x}) \rrbracket \quad (3.24)$$

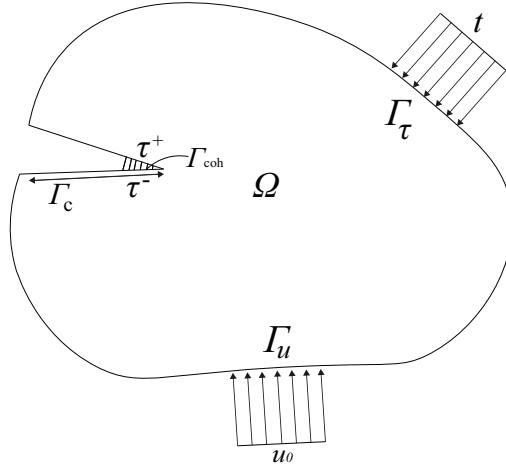


Figure 3.8: Body Ω containing discontinuity Γ_c

$\delta \hat{\mathbf{u}}$ and $[[\delta \mathbf{u}]]$ are standard and enriched test functions.

$$\int_{\Omega} (\delta \hat{\mathbf{u}} + H_{\Gamma_c} [[\delta \mathbf{u}]]) \nabla^s \boldsymbol{\sigma} d\Omega = 0 \quad (3.25)$$

Using Divergence theorem and eliminating the Heaviside function by integrating the integral over Ω^+ , the equation can be re-written as:

$$\int_{\Omega} \nabla^s \delta \hat{\mathbf{u}} : \boldsymbol{\sigma} d\Omega + \int_{\Omega} \nabla [[\delta \mathbf{u}]] : \boldsymbol{\sigma} d\Omega + \int_{\Gamma_c} [[\delta \mathbf{u}]] \cdot \boldsymbol{\tau}_c d\Omega = \int_{\Gamma_t} \delta \hat{\mathbf{u}} \cdot \mathbf{t} d\Gamma + \int_{\Gamma_{\tau^+}} [[\delta \mathbf{u}]] \cdot \mathbf{t} d\Gamma \quad (3.26)$$

The last integral in Eq. 3.26 is only for the methods that consider enrichment for the whole domain such as GFEM. Here, only the elements around the crack are enriched and the external forces do not interact with the enriched degrees of freedom. Tractions $\boldsymbol{\tau}$ are cohesive forces in the cohesive zone which are linked to the enhanced degrees of freedom. The discontinuous displacement field in Eq. 3.2 can be used to discretize the trial displacement field:

$$\delta \mathbf{u}^h(\mathbf{x}) = \sum_{i \in n_{std}} N_i(x) \mathbf{u}_i + \sum_{i \in n_{enr}} N_i(\mathbf{x}) H_i(\mathbf{x}) \mathbf{a}_i \quad (3.27)$$

Or in matrix form:

$$\mathbf{u}(\mathbf{x}) = \mathbf{N}(\mathbf{x}) \mathbf{u} + H_{\Gamma_c} \mathbf{N}(\mathbf{x}) \mathbf{a} \quad (3.28)$$

The number of added degrees of freedom is twice the number of terms in the enhanced basis. It is important to recognize that the displacement approximation from the extra

degrees of freedom is the opening displacement of the crack mouth. The displacement of the extra degree of freedom at the node shows the contribution of that node to the crack opening. In this way, the damage can be defined in a node based manner and be approximated inside the element. The strain field is found by differentiating Eq. 3.28:

$$\boldsymbol{\epsilon} = \nabla^s \mathbf{u}^h = \mathbf{B}\mathbf{u} + H_{\Gamma_c} \mathbf{B}\mathbf{a} \quad (3.29)$$

s super-script denotes the symmetric part of the derivatives of \mathbf{u} . \mathbf{B} is the matrix of the shape function derivatives.

$$\mathbf{B} = \begin{bmatrix} \frac{\partial N_i}{\partial x} & 0 \\ 0 & \frac{\partial N_i}{\partial y} \\ \frac{\partial N_i}{\partial y} & \frac{\partial N_i}{\partial x} \end{bmatrix} \quad \text{for } i = 1, 2, \dots, n \text{ nodes} \quad (3.30)$$

Replacing the displacement derivatives in Eq. 3.26 by 3.29 yields:

$$\int_{\Omega} \mathbf{B}^T \boldsymbol{\sigma} d\Omega = \int_{\Gamma_t} \mathbf{N}^T \mathbf{t} d\Gamma \quad (3.31)$$

$$\int_{\Omega} H_{\Gamma_c} \mathbf{B}^T \boldsymbol{\sigma} d\Omega + \int_{\Gamma_c} \mathbf{N}^T \boldsymbol{\tau} d\Gamma = 0 \quad (3.32)$$

The traction force at the cohesive zone is a function of the displacement which causes non-linearity of the system [92]. To linearise the equations 3.31 and 3.32, a rate form of the constitutive relations is required to iteratively solve the equation. The stress rate $\dot{\boldsymbol{\sigma}}$ is related to strain rate $\dot{\boldsymbol{\epsilon}}$ as follow:

$$\dot{\boldsymbol{\sigma}} = \mathbf{C}\dot{\boldsymbol{\epsilon}} = \mathbf{C}(\mathbf{B}\dot{\mathbf{u}} + H_{\Gamma_c} \mathbf{B}\dot{\mathbf{a}}) \quad (3.33)$$

\mathbf{C} is the tangent stiffness matrix of the material and is rate independent. The stress and strain rate are derivatives of stress and strain in time. The cohesive traction force also needs to be written in rate form:

$$\dot{\boldsymbol{\tau}}_c = \mathbf{T}([\dot{\mathbf{u}}]) = \mathbf{T}\mathbf{N}\dot{\mathbf{a}} \quad (3.34)$$

\mathbf{T} is the tangential modulus matrix of the discontinuity and is calculated by partially differentiating the CZ constitutive relationship:

$$\mathbf{T} = \frac{\partial \boldsymbol{\tau}}{\partial [\dot{\mathbf{u}}]} \quad (3.35)$$

The tangential modulus of the discontinuity on the crack coordinate system at the crack surface needs to be transferred using the rotation matrix. The cohesive forces and the stiffness matrix has to be defined in the local crack coordinate system on the crack discontinuity and has to be rotated to the global coordinate system too:

$$\mathbf{T} = \mathbf{R}^T \mathbf{T}' \mathbf{R} \quad (3.36)$$

\mathbf{R} is the rotation matrix, \mathbf{T}' is calculated from the local values from Eq. 3.17:

$$\mathbf{T}' = \begin{bmatrix} \frac{\partial \tau_s}{\partial \delta_s} & \frac{\partial \tau_s}{\partial \delta_n} \\ \frac{\partial \tau_n}{\partial \delta_s} & \frac{\partial \tau_n}{\partial \delta_n} \end{bmatrix} \quad (3.37)$$

Each mode cohesive law's tangent can be considered for the derivatives in the stiffness matrix:

$$\frac{\partial \tau_s}{\partial \delta_s} = -\frac{\tau_{0s}^2}{2G_{IIc}} \quad (3.38)$$

$$\frac{\partial \tau_n}{\partial \delta_n} = -\frac{\tau_{0n}^2}{2G_{Ic}} \quad (3.39)$$

G_{Ic} and G_{IIc} are the critical values of energy release rate for mode I and mode II crack opening. This tangent was used to provide faster convergence but for unloading, a secant stiffness is defined that passes through the origin. It should be noted that a secant stiffness can be used for both cases but for zero displacement, the current cohesive law predicts infinity and a penalty stiffness is usually used instead.

$$\frac{\partial \tau_s}{\partial \delta_s} = k_s = \tau_{0s} \left(\frac{1}{\delta_s} - \frac{\tau_{0s}}{2G_{IIc}} \right) \quad (3.40)$$

$$\frac{\partial \tau_n}{\partial \delta_n} = k_n = \tau_{0n} \left(\frac{1}{\delta_n} - \frac{\tau_{0n}}{2G_{Ic}} \right) \quad (3.41)$$

By arranging the equations in matrix form, the final formulation for the Newton-Raphson iterative solver writes:

$$\begin{bmatrix} \int_{\Omega} \mathbf{B}^T \mathbf{D} \mathbf{B} d\Omega & \int_{\Omega} H_{\Gamma_c} \mathbf{B}^T \mathbf{D} \mathbf{B} d\Omega \\ \int_{\Omega} H_{\Gamma_c} \mathbf{B}^T \mathbf{D} \mathbf{B} d\Omega & \int_{\Omega} H_{\Gamma_c} \mathbf{B}^T \mathbf{D} \mathbf{B} d\Omega + \int_{\Gamma_d} N^T \mathbf{T} N d\Gamma \end{bmatrix} \begin{bmatrix} d\mathbf{u} \\ d\mathbf{a} \end{bmatrix} = \begin{bmatrix} \mathbf{f}_u^{ext} \\ \mathbf{f}_a^{ext} \end{bmatrix} - \begin{bmatrix} \mathbf{f}_u^{int} \\ \mathbf{f}_a^{int} \end{bmatrix} \quad (3.42)$$

And the internal and external forces are:

$$\mathbf{f}_u^{int} = \int_{\Omega} \mathbf{B}^T \boldsymbol{\sigma} d\Omega \quad (3.43)$$

$$\mathbf{f}_a^{int} = \int_{\Omega} \mathbf{B}^T \boldsymbol{\sigma} d\Omega + \int_{\Gamma_c} \mathbf{N}^T \boldsymbol{\tau} d\Gamma \quad (3.44)$$

$$\mathbf{f}_u^{ext} = \int_{\Gamma_t} \mathbf{N}^T \bar{\mathbf{t}} d\Gamma \quad (3.45)$$

It should be noted that \mathbf{f}_a^{ext} is equal to zero in this formulation. This is because the traction boundary condition Γ_{τ} does not interact with the extra degrees of freedoms \mathbf{a}_i .

3.4.3 Crack propagation and growth direction criterion

The propagation happens in XFEM by continually adding nodes to the enriched zone when the criterion for the propagation has been met. There is two categories of crack growth criteria: stress based criterion and energetic based approach.

Stress based criterion

During the numerical solution, the principal stresses are calculated at all integration points ahead of the crack-tip at the end of every load or crack increment. If the stress exceeds the material yield strength the crack needs to be extended. The extension of the crack can be smaller or larger than the element size and for the quasi-static solver, it can be related to the severity of the stress ahead of the crack-tip to calibrate the crack extension size at the end of each increment for better performance. The extra degrees of freedom on the nodes just ahead of the crack-tip must be zero and that is why in [143] the nodes ahead of the crack-tip are not enriched.

The orientation of the crack in the stress based criterion can be calculated using the stress field. It is not always possible to know the stress at the crack-tip accurately since it is not necessarily placed at the Gauss points or nodes. Instead, an average tensor can be used in a non-local form to find the principal stress orientation which is normal to the expected crack growth. One approach for calculating this average stress was used for cohesive crack by Wells and Sluys [143] by means of the following Gaussian weight function:

$$w(r) = \frac{1}{(2\pi)^{3/2} l^3} \exp\left(-\frac{r^2}{2l^2}\right) \quad (3.46)$$

w is the weight function and l controls how fast the weight function approaches zero away from the crack-tip at distance r . The weighted average of the stresses around the crack-tip is calculated on the Gauss points at distance r from the crack-tip.

SIF based criterion

By definition, the SIF vanishes at the cohesive crack-tip when the equilibrium state is achieved [15]. Normally because the mode II SIF is small compared to mode I, it is usually neglected. Mões and Belytschko solved the problem by finding the external load that results in zero SIF at the numerical crack-tip [93]. The SIF calculated from the bulk of the material and caused by the external forces are countered by the SIF from cohesive forces:

$$K = K_{ext} + K_{coh} = 0 \quad (3.47)$$

K_{coh} is calculated using J-integrals or VCCT and the external stress intensity factor can be calculated from the external work. When SIF criterion is used, the crack propagation direction can also be calculated using the maximum hoop stress law [43]:

$$\theta = 2 \operatorname{atan} \frac{1}{4} \left(K_I^{ext} / K_{II}^{ext} \pm \sqrt{(K_I^{ext} / K_{II}^{ext})^2 + 8} \right) \quad (3.48)$$

The smooth crack closing condition

When the SIF at the crack-tip equals zero, the crack closes smoothly. In this case, only mode one crack opening is considered. This condition happens when the stresses normal to the crack at the crack-tip is equal the tensile strength of the material [77].

3.5 Numerical implementation

The model is implemented in the *in-house* MATLAB code. The cohesive zone is solved using iterative Newton-Raphson scheme. The subroutines for stiffness matrix and the level sets are modified versions of XFEM subroutines by M. Pais [103]. The main solver, J-Integral, damage and cohesive force subroutines are developed by the author. In order to implement CZM, the following modifications were made to the stiffness matrix:

- Inclusion of orthotropic material stiffness matrix.

- Integration of the cohesive stiffness matrix for the cohesive elements.
- defining the numerical and physical crack-tips so that only the elements between the two tips are selected for the CZ.
- Removal of the crack-tip enrichments.
- Developing a new integration scheme at the crack-tip element to allow the element to be partially cut.

The load is fully applied at once in the first iteration and not gradually. Both scenarios of gradual and sudden application of load was tested and the results were similar. In crack-length-controlled approach, which is used here, the cohesive zone length is initially zero. The numerical and physical crack-tips are close to each other in the beginning and have to expand. When the crack is short, the cohesive forces cannot overcome the opening load and the displacement jump increases. This displacement causes damage and reduces the cohesive traction. In this situation, the bulk material ahead of the crack-tip has to sustain the load which results in tractions larger than the maximum material strength ahead of the numerical crack-tip. The crack has to grow and new cohesive traction surfaces are created. This process continues until the cohesive forces balance the external load such that the traction at the tip is equal τ_0 [93]. When the crack-tip stress equals the maximum traction, the opening displacement (and damage) is zero. It is reminded that zero displacement returns the maximum traction in the traction-separation law.

Figure 3.9. demonstrate the flowchart for the quasi-static solver. It should be reminded that if the external load is large enough, the crack can grow after the full cohesive zone is developed. In that case, both physical and numerical crack-tips will move forward. On the other hand, when the load is below the critical value, the cohesive zone will be smaller than the fully developed cohesive zone and the physical crack-tip experiences a damage lower than 1. This approach is employed since this solver is also used for fatigue simulation which requires the crack grow at ERRs lower than the critical values. The ERR is calculated for the external load M when the solver reaches equilibrium and the CZ is extended such that the stress criteria is satisfied. As it is explained in the next chapter, this value of ERR is then used for

the fatigue simulation under constant envelope load (since constant moment creates constant ERR).

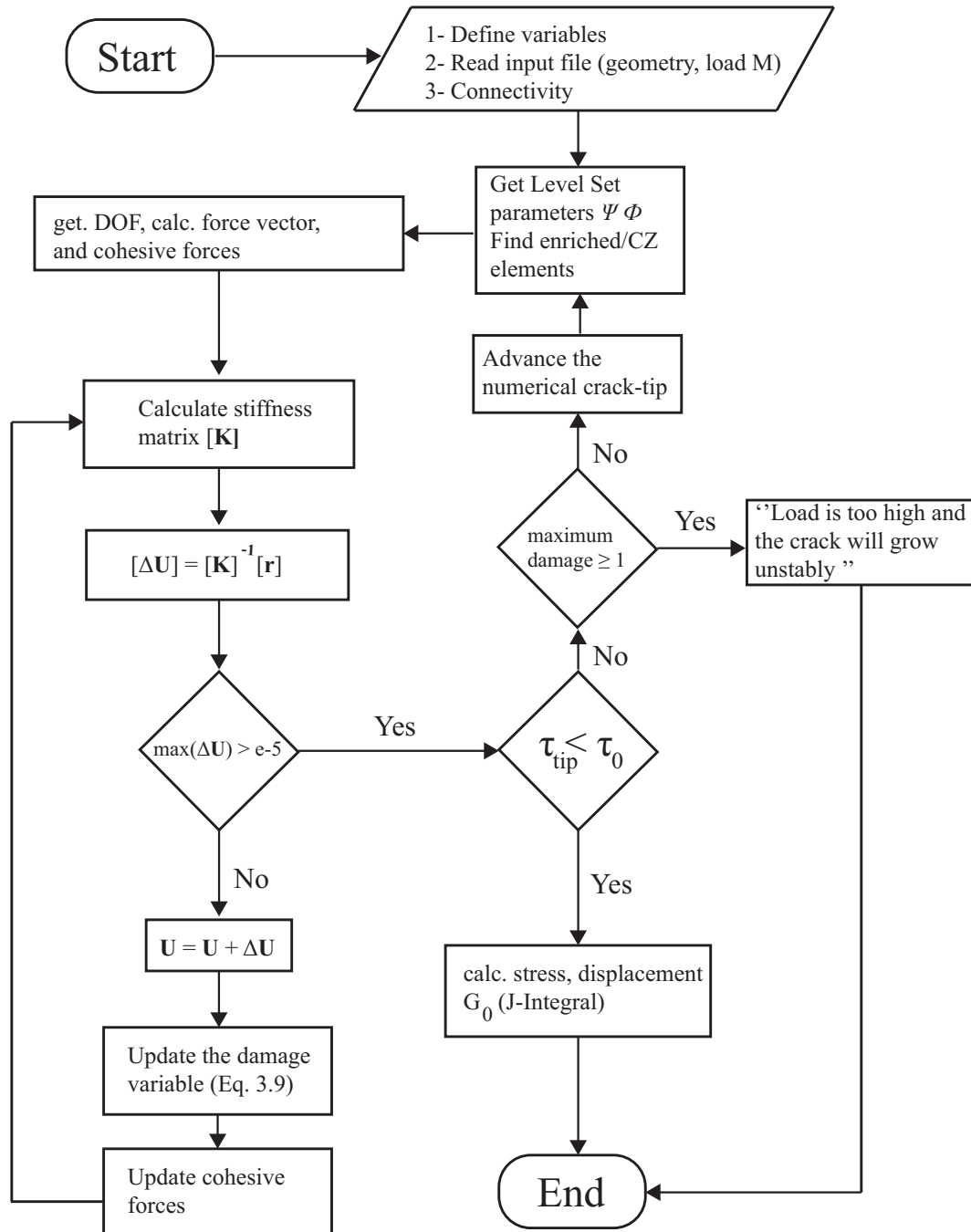


Figure 3.9: Flowchart for the quasi-static solver for the load controlled test under applied moment-load M . The solver finds the equilibrium state at which the numerical crack-tip stress is equal τ_0 .

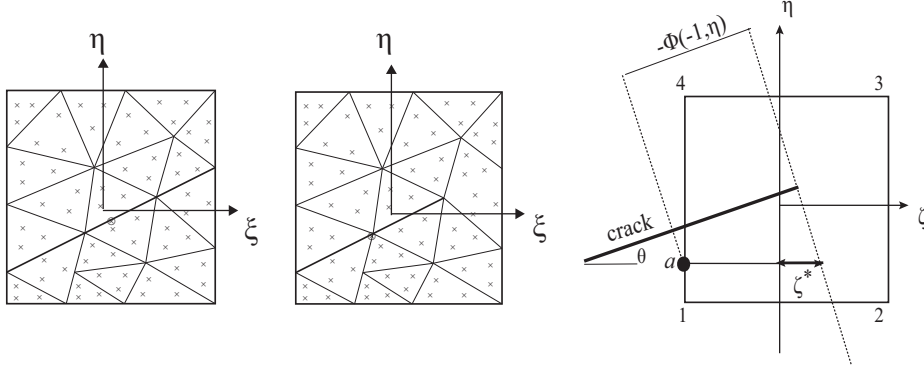


Figure 3.10: The triangulation of the enriched elements and the modification of the shape functions to count for the crack location in the element(right)

3.5.1 Integration scheme

The integration for the cut elements is done by more integration points than standard elements for both sides of the displacement jump. The cut element is further triangulated into sub-domains to be integrated using three-point Gauss quadrature (Fig. 3.10). For the elements in the cohesive zone, one integration point on the discontinuity is used to integrate the cohesive forces. The crack-tip enrichments were removed due to the reasons described in chapter two. As a consequence of removal of the crack-tip enrichments, when the crack discontinuity jump function is used on the tip element, it cuts the whole element.

In this case, the growth of the crack inside an element is not detected. For this reason, the enriched shape functions associated with the nodes at the crack-tip element is modified to only cut the element until the tip. The shape functions should become zero on the crack-tip normal line where $\Phi = 0$ (Φ is the distance to the normal to the crack at the crack-tip). This is done by changing the shape functions that are cut by the crack-tip normal.

$$N_1 = \frac{1}{2}(1 - \eta)\left(\frac{\zeta^* - \zeta}{\zeta^* + 1}\right) \quad , \quad N_4 = \frac{1}{2}(1 + \eta)\left(\frac{\zeta^* - \zeta}{\zeta^* + 1}\right) \quad (3.49)$$

$$N_2 = N_3 = 0 \quad (3.50)$$

$$\zeta^* = \begin{cases} \left(\frac{-\Phi(-1, \eta)}{\cos(\theta)l_e/2} - 1\right) & \text{for } \frac{-\Phi(-1, \eta)}{\cos(\theta)l_e/2} < 2 \\ 1 & \text{otherwise} \end{cases} \quad (3.51)$$

$\Phi(-1, \eta)$ is the distance between point a on side 1-4 of the element to the line normal to the crack at the crack-tip (Fig. 3.10). It is reminded that this is for the case where

θ is smaller than 45° , and for the cracks that exceed this limit, same modification can be done to η part of the shape function in a similar fashion. N_2 and N_3 are zero for the case shown in Fig. 3.11. These shape functions satisfy the partition of unity assumption as well. The displacement field for the crack-tip element is:

$$u = \hat{f}(N_1u_1 + N_2u_2) \quad (3.52)$$

with:

$$\hat{f} = \Upsilon(\Psi(\zeta, \eta)) H(-\Phi(\zeta, \eta)) \quad (3.53)$$

\hat{f} divides the element into three sections; un-enriched ahead of the crack, above the crack and below the crack (Fig. 3.11) where shifted enrichment is used:

$$\Upsilon(x) = Sgn(\Psi_{gp}) - Sgn(\Psi_i) \quad (3.54)$$

Ψ_{gp} is the value of Ψ at Gauss integration points and Ψ_i is the value of Ψ at each node. H represents Heaviside function:

$$H = \begin{cases} +1 & \text{for } x > 0 \\ 0 & \text{for } x < 0 \end{cases} \quad (3.55)$$

It is possible to provide a more accurate approximation for distances very close to the crack-tip by multiplying a $1/r$ term to the shape functions. Usually, these base functions are added through additional degrees of freedom for the crack-tip enrichment but if it is applied directly on the discontinuous function, it leads to loss of partition of unity characteristic [36] and will not vanish at the element boundaries. The shape functions were built in MATLAB for illustration and as it can be seen in Fig. 3.12, instead of cutting the whole element, the enrichment only creates a jump partially in the element and the additional displacement field is zero on the entire element. After applying the modification to the code, the stress fields are corrected as depicted in Fig. 3.13. When the crack-tip correction is not in place, the entire element containing the crack-tip is cut and since there is no cohesive force applied ahead of the crack-tip, this part of the element act as if it contains traction free surface. Even for small meshes, the oscillation at the crack-tip can cause problem in calculation of the energy release rate and maximum stress at the crack-tip.

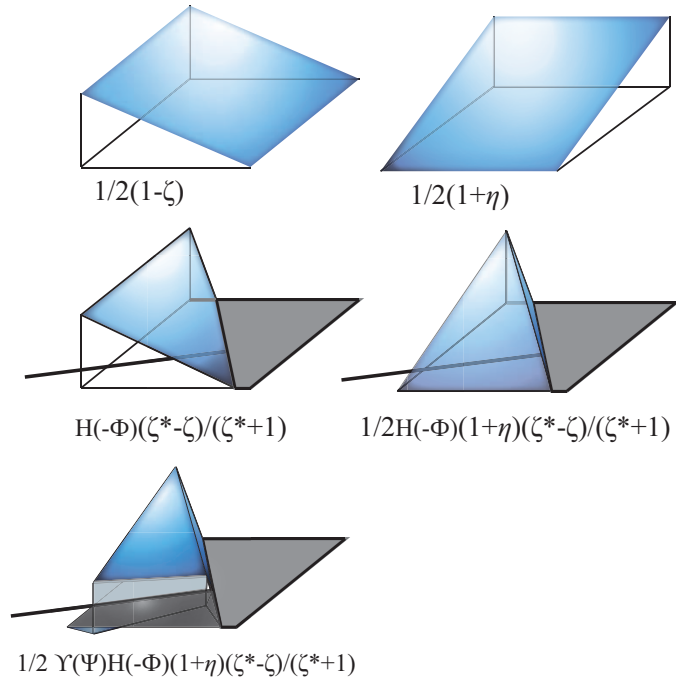


Figure 3.11: Construction of the N_3 shape function for the third node (top left node) of the crack-tip element. Υ is the discontinuous function for crack opening

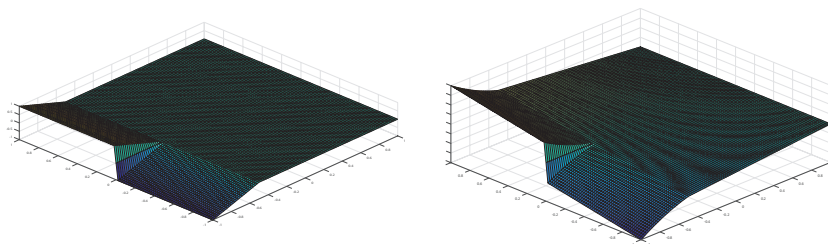


Figure 3.12: The modified displacement field shape function (left) and a displacement field for a trial nodal displacement applied at nodes (right)

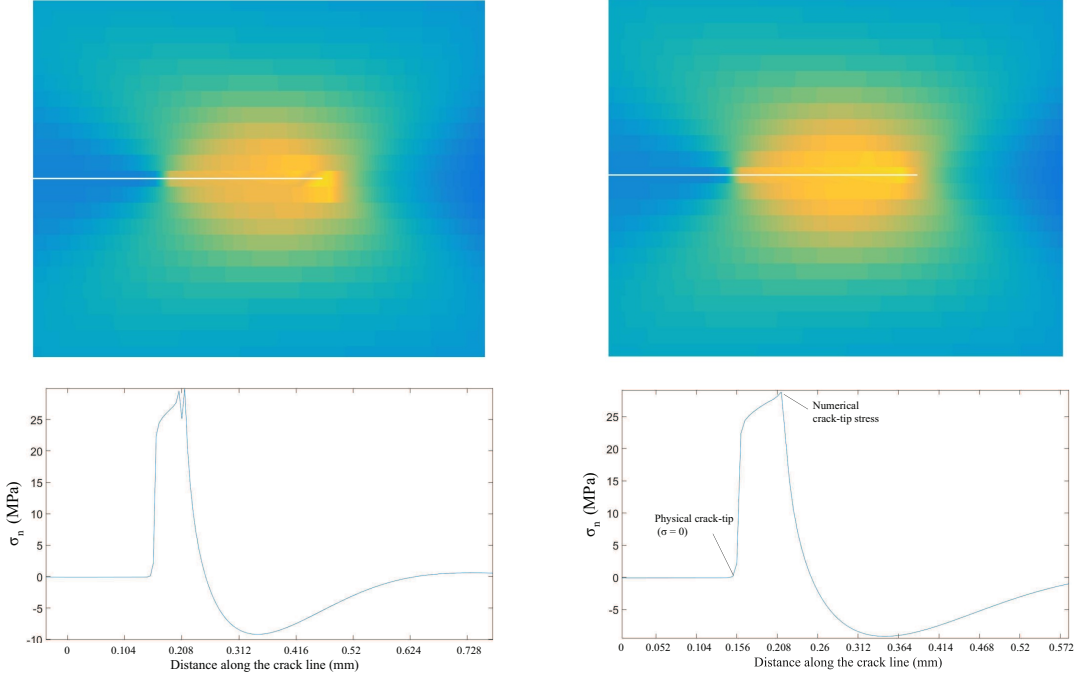


Figure 3.13: The stress distribution before (left) and after crack-tip enrichment correction. In this example, the cohesive zone is not fully developed and the traction at the physical crack-tip is non-zero.

3.5.2 On the nodal cohesive force implementation

The nodes of the cracked element have two extra degrees of freedom. The displacement of these extra variables are the contributions of each node to the *crack opening*. The total crack opening at the crack surface is:

$$\boldsymbol{\delta} = \llbracket \mathbf{u} \rrbracket^+ - \llbracket \mathbf{u} \rrbracket^- = \sum_1^n \llbracket \mathbf{u}_i \rrbracket N_i \Upsilon^+ - \sum_1^n \llbracket \mathbf{u}_i \rrbracket N_i \Upsilon^- \quad (3.56)$$

Υ function is defined in Eq. 3.54. The value of Ψ_{GP} is positive on the upper side of the crack and negative on the lower side. For example, for $\llbracket \mathbf{u} \rrbracket^-$ the enrichment function Υ is calculated as:

$$\Upsilon = Sgn(\Psi_{GP}) - Sgn(\Psi_{node1}) = -1 - (-1) = 0 \quad (3.57)$$

Repeating the calculations for all nodes and for each side, the opening displacement is calculated as:

$$\boldsymbol{\delta} = 2 \sum_1^n \llbracket \mathbf{u}_i \rrbracket N_i \quad (3.58)$$

Since this crack opening is related to the damage on the crack surfaces, a nodal value for the damage (d_i) can be defined such that:

$$D = \sum_{i=1}^n d_i N_i(\zeta_\Gamma, \eta_\Gamma) \quad (3.59)$$

d_i are the nodal values for the damage. This means that each node contributes to the damage on the crack surface the same amount it contributes to the opening. For the nodal forces, each node's contribution to the crack surface traction is decreased by the damage variable of that node. This means that the closer the crack is to the node, the larger the displacement and consequently the larger damage variable at that node. This means smaller nodal force due to the degradation.

$$f_i^n = \tau_0(1 - d_i)\sqrt{1 - B} \quad (3.60)$$

$$f_i^s = \tau_0(1 - d_i)\sqrt{B} \quad (3.61)$$

B is defined by Eq. 3.17. The cohesive force on the integration point on the crack is:

$$\mathbf{f}_c = \sum_1^n \mathbf{f}_i N_i(\zeta_\Gamma, \eta_\Gamma) \quad (3.62)$$

The damage variable used here is an energy based damage. These forces and displacements are related to the part of the stiffness matrix that was integrated only on the crack line in Eq. 3.42 so these nodal forces do not affect other integration points inside the element.

3.5.3 Energy release rate calculation for the cohesive zone

The energy release rate calculation is one of the most important part of the developed code since it has a fundamental role in the fatigue calculation (which is the final goal of this project). The energy release rate is calculated using modified J-Integral for CZM. Since the J-integrals are path independent, the contour of the cohesive zone Γ_{cz} can be used for integration. This is a very important future of this approach since the material outside this contour is not involved in the calculations and can be a general orthotropic material with various properties on each side of the crack. The J-integral is evaluated along the crack extension direction in the cohesive zone. Since

the displacement in load direction (normal to the crack) is negligible, the contribution of the strain energy W vanishes [23] and the integral becomes:

$$J = \int_{\Gamma_{cz}} \sigma_{ij} \frac{\partial \delta_x}{\partial x} dx \quad (3.63)$$

with δ and σ_{ij} being the crack opening displacement and the traction at the cohesive zone respectively. The J-Integral can be decomposed into mode I and mode II integrals by splitting the traction and displacement into the two following integrals [63]:

$$J_I = - \int_{\Gamma_{cz}} \sigma_y \frac{\partial \delta_y}{\partial x} dx \quad (3.64)$$

$$J_{II} = - \int_{\Gamma_{cz}} \sigma_{xy} \frac{\partial \delta_x}{\partial x} dx \quad (3.65)$$

$$(3.66)$$

for the numerical implementation, the above integrals are calculated and summed over the integration points on the crack line. The values of opening displacement and tractions are approximated on the integration points using the elements shape functions N_i .

$$J_I = \sum_{e_{cz}} \sum_j \left(\frac{l_e}{2} \left(\frac{\partial \delta_y}{\partial x} \right) \sigma_y w_j \right) \quad (3.67)$$

$$J_{II} = \sum_{e_{cz}} \sum_j \left(\frac{l_e}{2} \left(\frac{\partial \delta_x}{\partial x} \right) \sigma_{xy} w_j \right) \quad (3.68)$$

j is the integration point number and w_j is the integration weight.

3.6 Numerical tests and the results

In this section, two tests are done for the verification of the results. One of the tests is delamination of a DCB specimen under mode I, mode II and 50% mixed mode loading for constant G (since moments applied at the crack lips, Fig. 3.14). In this test, the cohesive zone length, stresses and the energy release rate are compared to the analytical solutions and other researchers' works. Another test is carried out for a DCB specimen this time for displacement controlled loading to extract load-displacement curve for the specimen. For this test, the solver has to be modified to run in displacement-controlled mode.

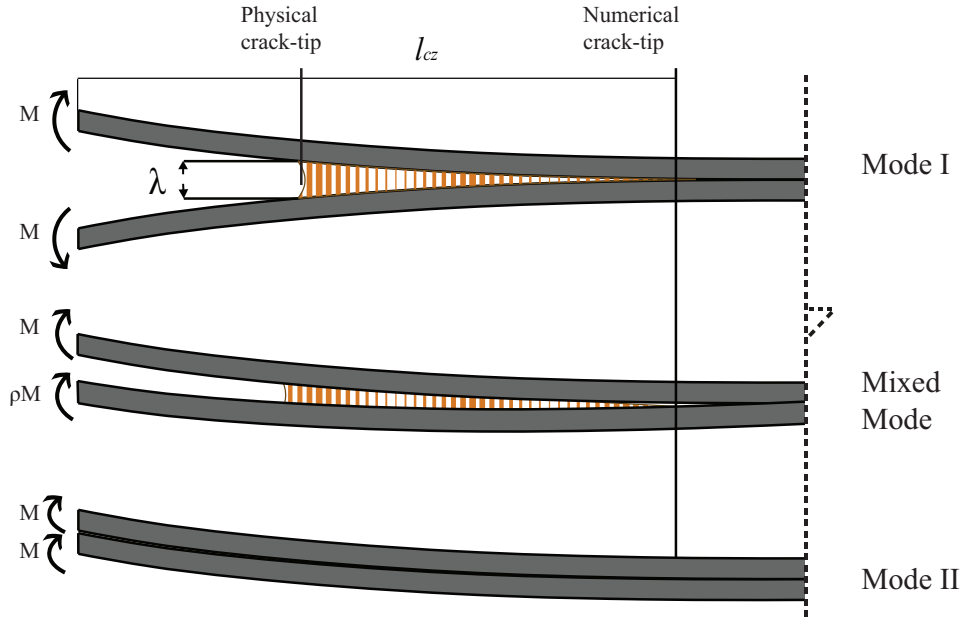


Figure 3.14: Moments M are used to create constant (G) for all crack lengths

3.6.1 Mode I test and the cohesive zone length

For the first test, a DCB specimen similar to Fig. 3.14 is used. Both plies have fibres in x direction $E_x = E_{11}$. The CZ length in composites can be regarded as a material and structural property [150]. By cohesive zone length (l_{cz}), the length of the fully developed cohesive zone is considered. For fatigue, depending on the model used, l_{cz} can vary from zero to full size (just before the physical crack-tip is about to propagate statically) based on the magnitude of the load. Most of the proposed models for cohesive zones provide an estimate for the cohesive zone length. For Irwin model [71], the cohesive zone length is the size of the area ahead of the crack-tip in a ductile material that has deformed plastically. Similarly Dugdale [40] used yield stress ahead of the crack tip to define the cohesive zone length. Other approaches include soft elastic material cohesive zone estimation [65] and cohesive zone under dynamic effects [117, 46], to name some. These techniques calculate the cohesive zone length as a function of the critical energy release rate G_c , elastic modulus, and the maximum strength τ_0 . The cohesive length is between 0.2-1 times the value of $E \frac{G_c}{\tau_0}$ depending on the cohesive zone model [137] used which shows there is a large variation between the calculated lengths for different models and the results are approximations to the order of magnitude. For a slender model for DCB test, the characteristic length of

the cohesive zone for infinite bodies can be calculated as[150]:

$$l_{cz} = \left[E \frac{G_c}{\tau_0^2} \right]^{1/4} t^{3/4} \quad (3.69)$$

t is the thickness of the laminae. Using Eq. 3.69, the cohesive zone length is calculated

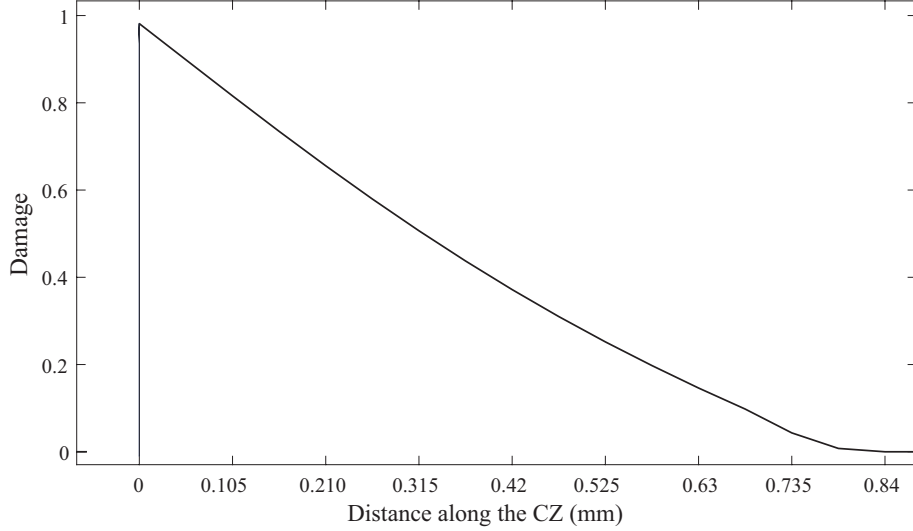


Figure 3.15: Damage distribution along crack line in the fully developed cohesive zone. There are 16 element in the cohesive zone and $l_e = 0.0526 \text{ mm}$

for a double cantilever beam specimen with $E_1 = 150000 \text{ MPa}$, $E_2 = 11000 \text{ MPa}$, $G_c = 0.35 \text{ kJ/m}^2$, $\tau_0 = 60 \text{ MPa}$, and $t = 1.98 \text{ mm}$ (material properties are for T300/977 – 2 carbon-fibre-reinforced epoxy laminate [53]). Module of elasticity is calculated based as $E = \frac{1}{1-\nu^2} \frac{2E_1E_2}{E_1+E_2}$.

$$l_{cz} = \left[21300 \frac{0.35}{60^2} \right]^{1/4} (1.55)^{3/4} = 2.003 \text{ mm} \quad (3.70)$$

The results from the numerical solution for the mentioned setting using $l_e = 0.058 \text{ mm}$ is 0.82 mm which is equal to the length of 14 elements in the cohesive zone. For more intense mesh the cohesive zone length is predicted slightly larger (0.84 mm for $l_e = 0.0526 \text{ mm}$ Fig. 3.15) but it must be remembered that full cohesive zone with exactly zero traction at the physical tip and τ_0 at the numerical tip, in numerical sense, is not easily achievable and larger meshes cause these value to be less accurate at the two end of the cohesive zone where the damage criteria are checked. The

Table 3.1: Material Properties for HTA6376/C [56], E and G values are in GPa

Property	E_{11}	E_{22}	E_{33}	G_{12}	G_{23}	G_{13}	ν_{12}	ν_{13}	ν_{23}	G_{Ic}	G_{IIc}
value	120	10.5	10.5	5.25	3.48	5.25	0.3	0.3	0.51	0.26	10.5

cohesive zone length from the simulation is less than half of the results from the analytical solution by Yang and Cox [150]. The analytical formulation is based on the assumption of infinite body and does not clearly states until what thickness is considered slender. [150] used a 0.2 mm thick laminate for the illustration. Harper and Hallett [56] mentioned the same problem in their paper in which they investigate the numerical implications of the issue since it has an important impact on deciding the mesh size for computations. In their work, they introduce a scale factor of $M = 0.5$ multiplied by the results of Eq. 3.69 and describe it as the correction due to the infinite depth assumption. It should be reminded that the formula 3.69 is for the case of using a cohesive law that does not start at zero traction when the displacement is zero [150, 137] and it will predict smaller cohesive zone, which might describe the reason why simulation result for the present work is slightly smaller.

The reason that in the present code there need to be more meshes in the cohesive zone is, in the author's opinion, the way the integration of stiffness matrix along the crack line is done, which only uses one point at the centre of the crack segment inside each element. This means that the cohesive zone has to be larger than the element size in the first place. The solver starts with the physical crack-tip and the numerical crack-tip placed very close to each other and more elements are added to the cohesive zone as the solver iterates (Fig. 3.16). The zone develops into a size several times larger than its initial length, which has to have at least one element to integrate the cohesive force at the starting point. In addition, since the crack is inside the element, as opposed to cohesive element approach, there is more approximation error due to the interpolations. The largest mesh with satisfactory result was $l_e = 0.14 \text{ mm}$ which resulted in $l_{cz} = 0.777 \text{ mm}$. Full cohesive zone for DCB specimen is depicted in Fig. 3.17. This test was done for a *HTA6376/C* specimen with properties in Table 3.1.

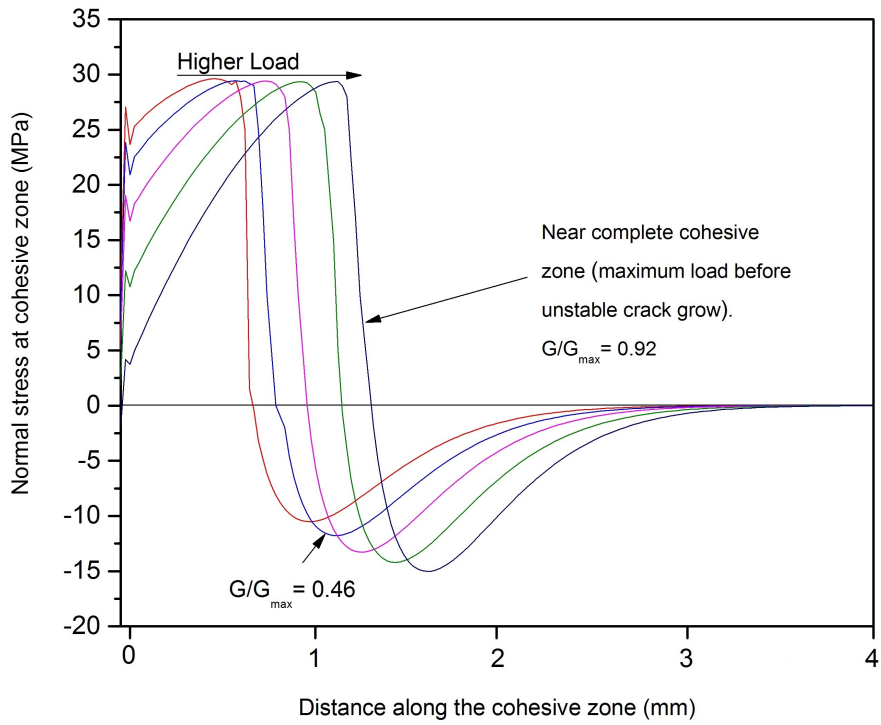


Figure 3.16: Normal stress evolution in the cohesive zone

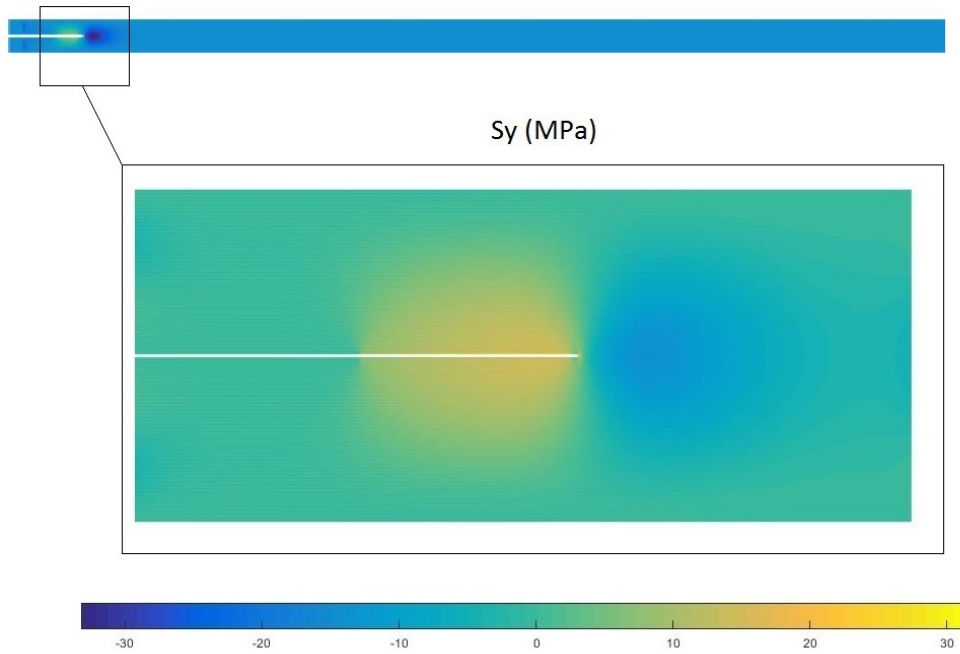


Figure 3.18: σ_y distribution under mode I opening load at $G_I = G_{Ic} = 0.26 kJ/m^2$ and initial $a = 4 mm$ for HTA6376/C, thickness=3.1 mm

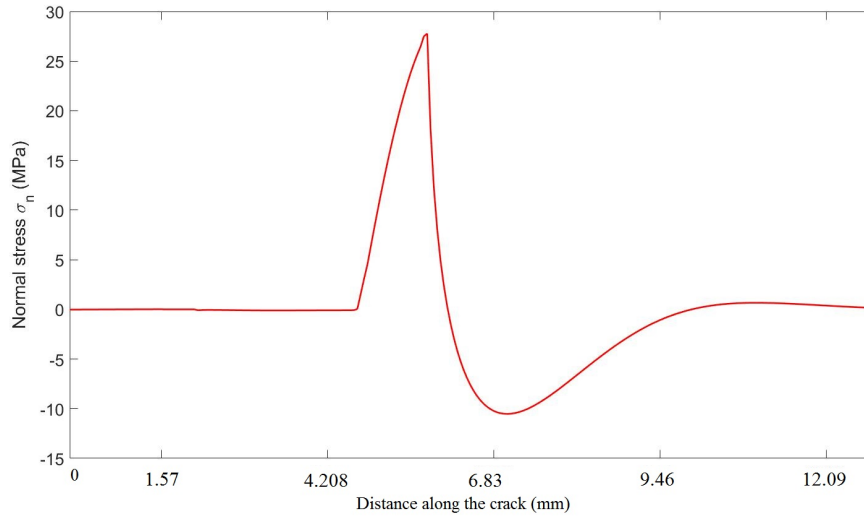


Figure 3.17: Full cohesive zone under mode I opening load at $G_I = G_{max} = 0.26 \text{ kJ/m}^2$. The length of the cohesive zone is approximately 0.87 mm.

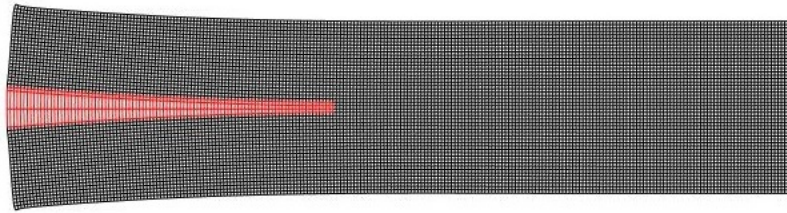


Figure 3.19: Crack opening deformation for full cohesive zone

3.6.2 Mode II test

By reversing the moment on the lower ply (see Fig. 3.14.), mode II crack opening can be simulated. It is reminded that the current code does not consider contact at the crack surfaces. This test is also done on a 3.1 mm thick HTA6376/C with the initial crack size of $a = 5 \text{ mm}$. Since the moment is created by means of a couple of two line forces, large horizontal forces were needed to create this opening as it can be seen from Fig. 3.21. In Fig. 3.21 maximum energy release rate for HTA6376/C laminate is 1.05 kJ/m^2 and the current plots show the case where the ERR is at about 0.75% of the critical value.

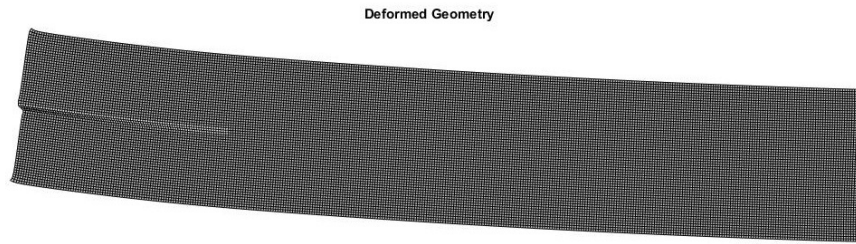


Figure 3.20: Crack opening deformation for $l_e = 1/17 \text{ mm}$

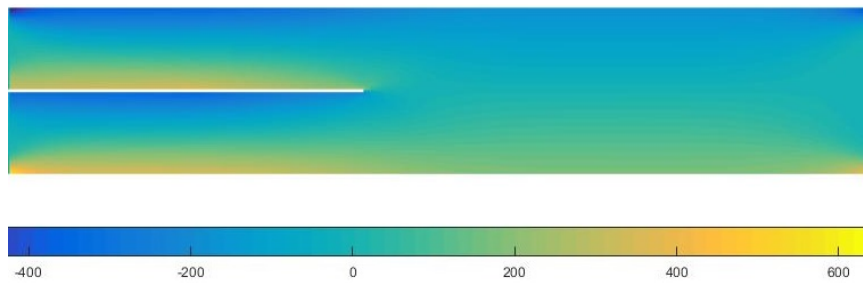


Figure 3.21: $G_{II} = 0.754 \text{ kJ/m}^2$ and $l_e = 1/17 \text{ mm}$

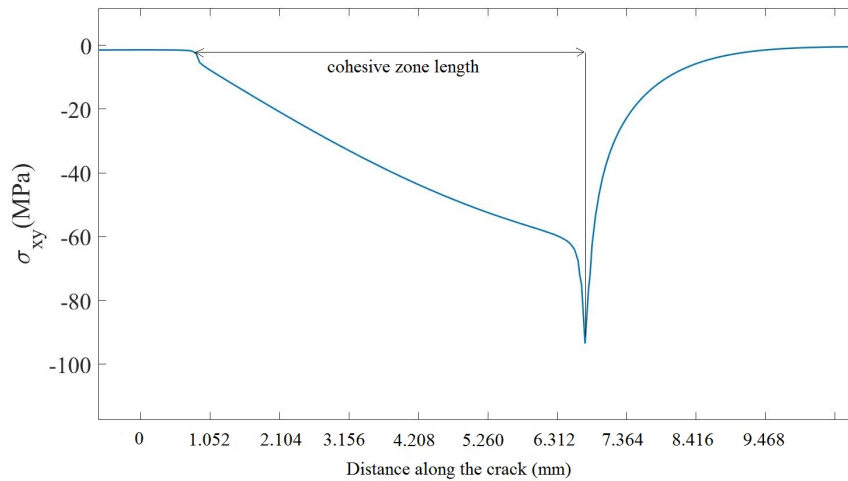


Figure 3.22: σ_{xy} for DCB $G_{II} = 1.07 \text{ kJ/m}^2$ (J-Integral) and $l_e = 1/19 \text{ mm}$ and $l_{cz} = 5.2 \text{ mm}$

The shear stress at the cohesive zone is plotted in Fig. 3.22 for a fully developed cohesive zone. Mode II cohesive zones are larger than mode one due to higher critical

ERR and traction. The cohesive zone length for the test in 3.22 is 5.2 mm . The shear stress at the crack-tip shows a jump on the last node. This is observed only in mode II and the reason can be that the crack-tip enrichment modification (Eq. 3.51) is only done in the direction of mode I opening.

3.6.3 Mixed mode case

The loading condition for 50% mixed mode is created by multiplying 0.0707 to one of the moments applied to the laminate [135] as depicted in Fig. 3.14. Same specimen setting is used for this test as mode I and II. The figures 3.23 and 3.24 show the response of the specimen for small loading about 0.1 time the critical ERR.

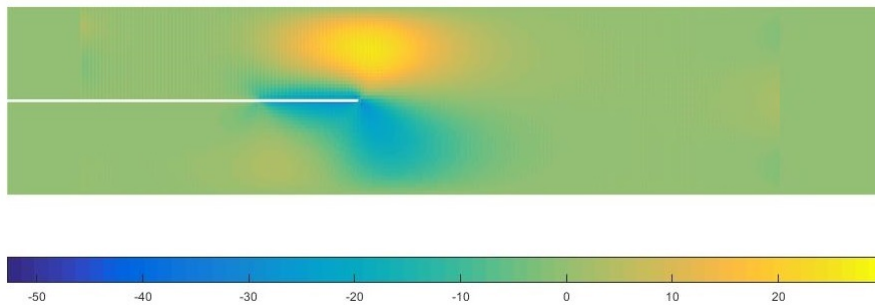


Figure 3.23: σ_{xy} at $G = 0.1\text{kJ}/\text{m}^2$ load and $l_e = 1/21\text{mm}$

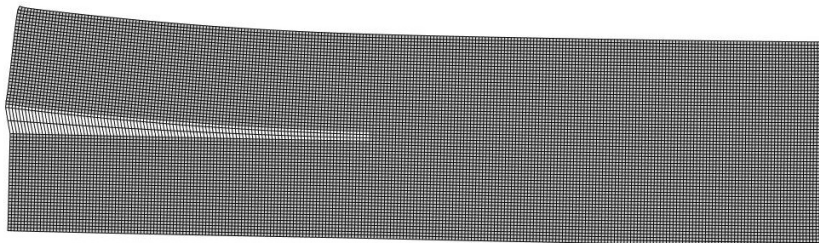


Figure 3.24: Deformation for 50% mixed model loading. The results are exaggerated.

When a 50% mixed mode loading is applied, the normal and tangential forces become equal. At the crack-tip, the maximum force from the numerical results in each direction is about 25.3 MPa . The resultant traction is:

$$\tau_{50\%} = \sqrt{\tau_n^2 + \tau_s^2} = 35.77\text{ MPa} \quad (3.71)$$

Since the displacements at the tip is zero, the damage must be close to zero and the equivalent traction force for mix mode condition is calculated using Eq. 3.16 which is almost the same as the numerical results:

$$\tau_0 = \sqrt{30^2 + (60^2 - 30^2)0.5^{2.7}} = 36MPa \quad (3.72)$$

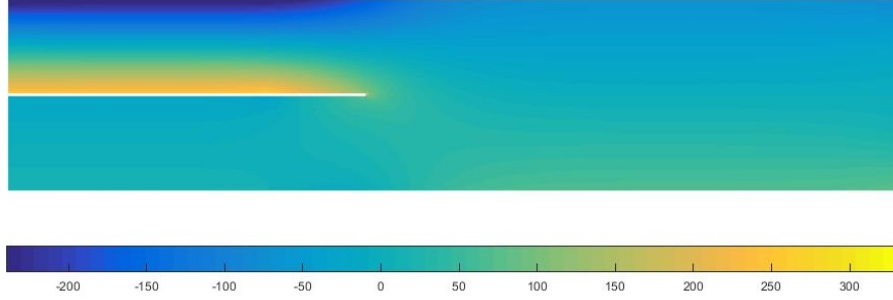


Figure 3.25: σ_{xx} for $G = 0.1kJ/m^2$ and $l_e = 1/21mm$

3.6.4 Simulation of double cantilever beam delamination (displacement controlled)

A load-displacement test is also carried out for the code verification. The solver is modified to run in displacement-control mode. In this case, there is no external forces applied and the internal forces (adding the cohesive forces) have to become zero on each iteration in order to cancel the forces caused by the applied displacement:

$$[\mathbf{r}] = [\mathbf{f}_{f_{DOF}}^{int}] - [\mathbf{K}_{\mathbf{f}_{DOF}, l_{DOF}}][\mathbf{U}_{l_{DOF}}] - [\mathbf{f}_{c_{DOF}}] \quad (3.73)$$

$$[\Delta \mathbf{U}_{f_{DOF}}] = [\mathbf{K}_{f_{DOF}, \mathbf{f}_{DOF}}][\mathbf{r}]^{-1} \quad (3.74)$$

where

$$[\mathbf{f}_{f_{DOF}}^{int}] = [\mathbf{K}_{f_{DOF}, \mathbf{f}_{DOF}}][\mathbf{U}_{f_{DOF}}] \quad (3.75)$$

$[\mathbf{U}]$ includes both standard and enriched degrees of freedom. \mathbf{r} is the residual force vector, \mathbf{f}_{DOF} are free degrees of freedom, l_{DOF} are the degrees of freedom subjected to the displacement load, and c_{DOF} are the extra degrees of freedom subjected to cohesive forces. The Newton-Raphson iteration continues until the maximum of $\Delta \mathbf{U}$ is smaller than 10^{-5} . The displacement history does not need to be kept as the non-linear part is only the cohesive zone and the history is kept by the damage variable.

The dimensions of the specimen and the boundary conditions are presented in Fig. 3.26. This unidirectional DCB of T/300/977-2 carbon fibre reinforced epoxy laminate is considered with the following properties:

Table 3.2: Material properties for T300/977-2 laminate[53]

E_{11}	E_{22}, E_{33}	G_{12}, G_{13}	G_{23}	ν_{12}, ν_{13}	ν_{23}	τ_{0n}	G_{Ic}
150GPa	11GPa	6GPa	3.7GPa	0.25	0.45	60 MPa	0.35N/mm

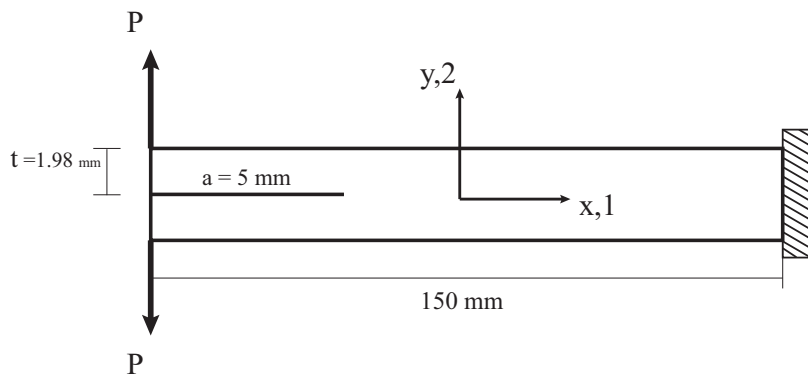


Figure 3.26: Double Cantilever Beam specimen.

The model consists of two orthotropic layers with the same orientation. As a result, there is no need for inclusion of an interface enrichment. Plane strain condition is assumed and mode I crack opening is considered for the load-displacement test. The test was run for several mesh refinements between 0.9 mm and 0.33 mm . Larger than 0.5 mm elements does not create enough elements in the cohesive zone and the results have high error.

The stress distribution in the cohesive zone and ahead of the numerical crack-tip is illustrated in Fig. 3.27 for high mesh intensity. There are 10 elements in the cohesive zone and the length of the cohesive zone is 0.9 mm . This length is consistent with the results from [137].

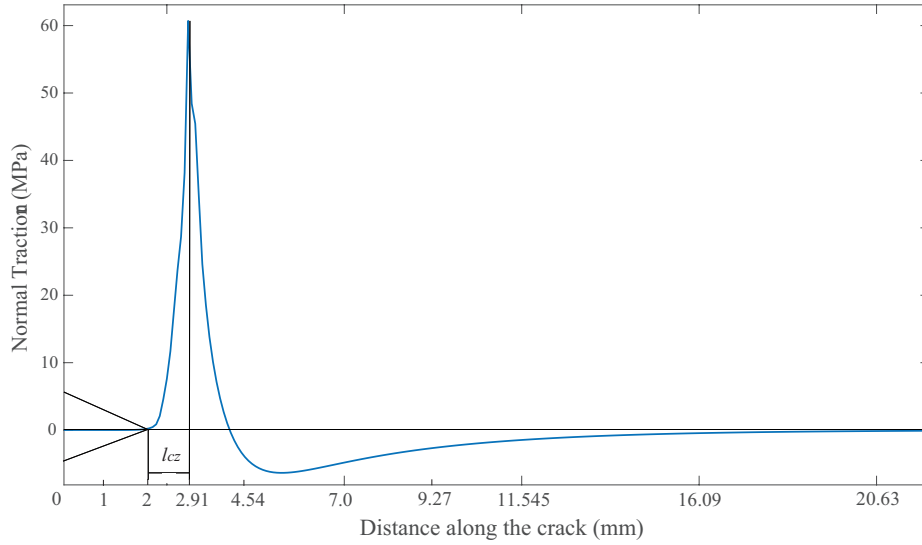


Figure 3.27: Stress distribution of the delamination crack in DCB specimen for intense mesh $l_e = 0.0909 \text{ mm}$

When the crack grows, higher ERRs are created and less load is needed to open the crack. To model the load-displacement response of the specimen, an algorithm was developed in order to control the crack opening displacement. The displacement needs to increase whenever the crack-tip stress is dropped below the critical value. On the other hand, when the stress at the crack-tip exceeds the material yield strength, the crack has to grow until the stress is dropped into a range close to the yield strength. It should be noted that the crack-tip stress check cannot be very restricted since it will cause a sharp rise and falls (vertical lines) in the load-displacement curve, especially for large meshes. This happens since large meshes underestimate the crack-tip stress. In that case, the loading keeps going up and when the critical stress is reached (at a load higher than what is really needed), the stress stays above the critical value for a while during the crack extension which causes a significant drop in the crack opening load. The delay in reaching the critical traction also causes an increase in damage which requires more crack growth do compensate. These vertical movements are visible in Fig. 3.28 for larger meshes and this is in-spite loosening the stress check at the crack-tip by $\pm 5 \text{ MPa}$.

The points on the plot 3.28 are taken from each time the Newton-Raphson solver has converged. It can be seen that for most of the element sizes, a linear load-displacement behaviour exist until about 5 mm crack opening. This segment is when

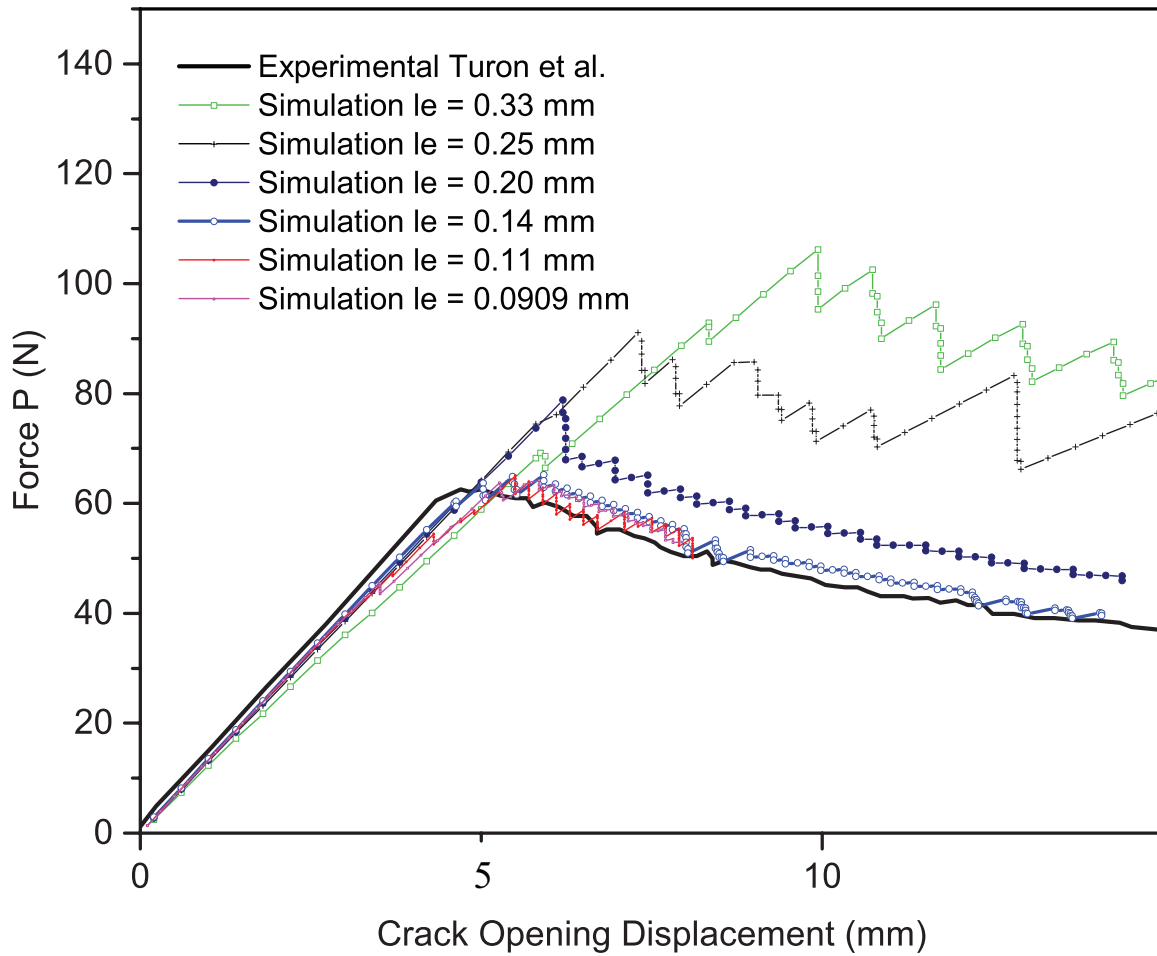


Figure 3.28: The load displacement test results for different mesh sizes. The experimental results are from Turon et al. [137]

the cohesive zone develops but the physical crack-tip has not moved yet. In other words, the damage at the physical crack-tip is below one. After about 5 mm crack opening displacement, the effect of mesh size is visible for meshes larger than 0.14 mm. This trend is similar to [56] and [137] results but the mesh size effect is more severe. There are two main reasons in the author’s opinion that causes this sensitivity to the mesh size; one is the fact that the crack is inside an element and there are errors added by the approximation in the cut element in XFEM. This is different from when the crack is explicitly defined on the edges of the elements. A four-node quadrilateral element cannot produce a smooth slope at the crack-tip with few meshes which has an impact on the cohesive forces and the cohesive length. Another reason is that the cohesive force is integrated only on one point on the cohesive segment inside the

element.

The errors triggered by the mesh size start after the cohesive zone is completed and the physical crack moves forward. The fact that coarse mesh leads to delayed physical crack-tip advance is caused by the underestimation of the stresses at the numerical crack-tip in coarse meshes. In this case, the displacement has to increase to create higher stress at the crack-tip. In the case of $l_e = 0.33 \text{ mm}$ there is only three elements in the cohesive zone. For a structure with non-proportionate dimensions such as a long thin laminate modelled here, the number of elements goes extremely high with mesh refinement and the tests for meshes smaller than 0.09 mm would take hours. Fig. 3.29 shows a zoomed figure of the specimen deformation with the smallest mesh (both plots are zoomed in).

For the vertical drops in the load, one way to avoid is to allow the displacement boundary to increase slightly during the crack growth. This was done to create a smoother graphs. However, this should be done carefully as a large increment in the displacement will cause stress fluctuation at the crack-tip.

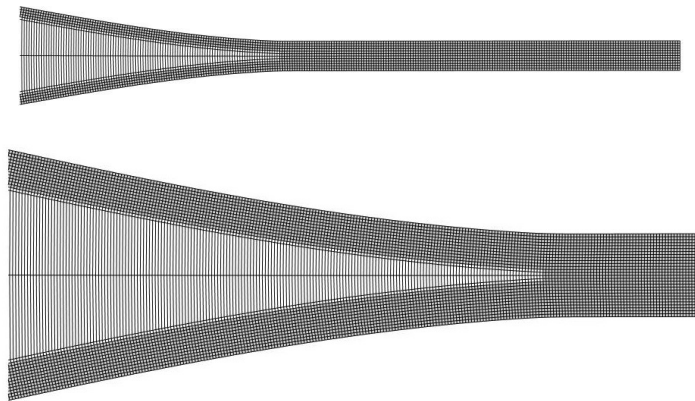


Figure 3.29: Crack opening for DCB test with high intensity mesh

It is possible to manipulate the stress threshold and/or the stiffness of the cohesive zone in order to adjust the load-displacement response for the coarse meshes [137] but since the model is used fatigue testing as well, it is preferred to use high mesh intensity instead of stiffness/stress manipulation to avoid any complications in the fatigue test. It should be reminded that the stiffness of the cohesive zone can be changed significantly and the solver will still converge but the problem arises when, for example, the cohesive zone is reaching its full size or the times when the cohesive

zone is too small. If the stiffness is too high, the maximum stress might even appear before the numerical crack-tip. On the other hand, too small stiffness matrix will cause instability when the cohesive zone is near its full size and the physical crack-tip traction drops to zero earlier.

3.7 Conclusion

In this chapter formulation and verification of the Newton-Raphson solver for the quasi-static CZ is described. In order to implement the cohesive zone in the XFEM code, the stiffness matrix was updated to include the cohesive stiffness which is integrated on the crack segment in each element. Two subroutines were developed for the damage and the cohesive force calculation on each node of the cohesive zone element. For the verification of the results, both load controlled and displacement controlled solvers were examined and the results are compared against other researchers works, including analytical solutions and experimental data.

The results of this chapter pave the way for the development of the fatigue solver since for fatigue, at each time step, the same quasi-static problem is solved. The optimum mesh size, minimum required meshes in the cohesive zone and selection of an appropriate range for the stiffness for the cohesive zone are important factors that have to be checked before fatigue simulation.

Chapter 4

Cyclic cohesive zone model in XFEM for high-cyclic delamination simulation

4.1 Introduction

Composite structures undergo gradual degradation by a various cracking mechanism under cyclic loading. One way of studying these degradation processes is to seclude the fracture mechanism and analyse the effect of the cyclic load on the evolution of the fault in the structure. Delamination is one of the most prevalent mechanisms of failure in composite structures that can occur at lower loading compared to other mechanisms [75] and this is no different in cyclic loading scenario. For the reasons described in chapters two and three, Cohesive Zone Model approach was chosen for quasi-static and fatigue analysis of the composite structures since it can handle the heterogeneity better when it comes to ERR calculation. In this chapter, a cyclic cohesive zone model for fatigue fracture is developed. This model degrades the material over a predefined number of cycles by linking the damage evolution to a variant of Paris law that uses ERR for calculation of the crack growth rate. In other words, this approach is translating the crack growth rate into cyclic damage growth in the cohesive zone.

4.2 Background

The test methods used for fatigue in composites are similar to those used for metals which have also led to the interpretation of the test results from a metallic fatigue

failure [58]. Paris law [105] is perhaps the most important theory on fatigue crack analysis which is used to relate the rate of the change in the crack size to a fracture parameter such as ERR. The crack growth can easily be calculated from XFEM results as long as the FM parameters are available. When it comes to composite fracture analysis, these methods suffer from difficulties caused by the material heterogeneity. A localized method is preferable to reduce the effect of the global structure on the fatigue model.

The damage mechanics approach, on the other hand, deals with the initiation and propagation of the fracture by introducing one or more damage variables that describe the degradation of the material stiffness [130]. In metals, cyclic loading creates micro-cracks which later merge together and form a macro-crack. In polymers and concretes, micro-decohesions and debondings act similar to the micro-cracking in metals and these faults result in degradation of the macro-scale mechanical properties of the structure [81]. The continuum damage mechanics can be used to model fatigue and unlike fracture mechanics, the crack propagates by means of damage growth and stress redistribution which is a localized approach[107]. Many damage-based fatigue models use cohesive zone framework for numerical implementation, which is due to its capabilities in evolving the crack automatically and that it does not need crack initiation[109](for the CZM that do not model the undamaged material the numerical crack does not grow automatically and new crack segments have to be added to the last segment).

Combining Paris law fatigue with CZM damage model for high-cyclic fatigue was proposed by Turon et al. [136] in 2007. They implemented the model in ABAQUS using cohesive elements. Later, Pirondi et al.[109] used the same method to evaluate fatigue fracture in bonded joints and they developed an automated process for the calculation of the ERR by means of global strain energy output of the FE analysis. Harper and Hallett [57] further developed the cyclic cohesive law and used it for 3D cohesive surface elements. Kawashita and Hallett [75] tried to make the formulation fully independent of the CZ length by developing an algorithm to track the crack-tip for cyclic delamination crack and as a result, the mesh and geometrical dependency was reduced. The cohesive law in [75] degrade the traction-separation curve smoothly from its original bi-linear form which is the source of the change in the cohesive zone length. Bak et al [14] argued that the results of various CZM models are not sensitive

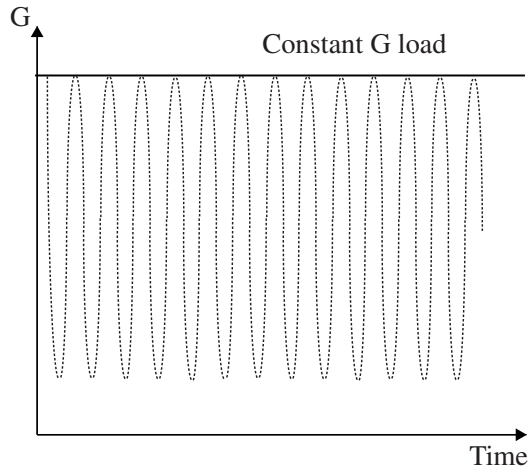


Figure 4.1: Envelope load model considers an equivalent static load over a known period of time for each time step of the quasi-static solution

to the shape of the cohesive traction-separation curve and proposed a new CZM in which the shape of the traction-separation locus is unchanged during the process.

The models mentioned in the previous paragraph are mostly implemented in FE solvers using cohesive or interface elements which generally pre-define the path of the crack. To the knowledge of the author, in spite of great potentials of XFEM in composite fracture simulation, there is no implementation of high-cyclic CZM in XFEM. The approach used here to develop the model in this study is based on the model of [14]. The cohesive law was modified to fit the XFEM platform. In this chapter, the derivation of the modified cyclic cohesive law is presented, followed by the algorithm and the time integration scheme for the fatigue damage evolution. The kinematics, discretization, element enrichments and J-Integral evaluation are not described here since they are similar to the quasi-static case described in the previous chapter.

4.3 Cohesive Zone Model

The two dimensional equivalent cohesive law described in chapter three is used here for the derivation of the cyclic cohesive zone model. An envelope load model [107] is used to replace several load cycles by an equivalent quasi-static load over a pseudo time. The maximum crack loading during the cycles should be used to allow the fatigue model to be solved as a quasi-static problem under a constant load while the number of cycles is considered continuous and a differentiable variable [14]. For

a double cantilever beam (DCB) the energy release rate can be kept constant by applying moment at the two crack lips (Fig. 3.14).

4.3.1 Cyclic damage law

The cyclic load affects the cohesive zone by updating the damage variable at each point based on the number of cycles, energy release rate and the crack growth rate from Paris law. Since there is no undamaged part in the cohesive law, any point governed by the cohesive law has already passed the damage threshold stress τ_0 . The cyclic damage evolution is a function of the cohesive law parameters and the crack growth rate ($dD^e/dN = f(G_c, G, \tau_0, \lambda)$). Applying chain rule, dD/dN can be calculated:

$$\frac{\partial D}{\partial N} = \frac{\partial D}{\partial G_c} \frac{\partial G_c}{\partial N} + \frac{\partial D}{\partial \tau_0} \frac{\partial \tau_0}{\partial N} + \frac{\partial D}{\partial \lambda} \frac{\partial \lambda}{\partial N} \quad (4.1)$$

The derivatives are calculated using the relations of the CZM in section 3.4.1:

$$\frac{\partial G_c}{\partial N} = \frac{\partial G_c}{\partial B} \frac{\partial B}{\partial \beta} \frac{\partial \beta}{\partial a} \frac{\partial a}{\partial N}, \quad \frac{\partial \tau_0}{\partial N} = \frac{\partial \tau_0}{\partial B} \frac{\partial B}{\partial \beta} \frac{\partial \beta}{\partial a} \frac{\partial a}{\partial N}, \quad \frac{\partial \lambda}{\partial N} = \frac{\partial \lambda}{\partial a} \frac{\partial a}{\partial N} \quad (4.2)$$

$$\frac{\partial D}{\partial G_c} = -\frac{\lambda \tau_0}{G_c^2}, \quad \frac{\partial D}{\partial \tau_0} = \frac{\lambda}{2G_c}, \quad \frac{\partial D}{\partial \lambda} = -\frac{\tau_0}{2G_c} \quad (4.3)$$

$$\frac{\partial B}{\partial \beta} = 2B(\beta - B(2\beta - 1))\beta^{-2} \quad (4.4)$$

$$\frac{\partial G_c}{\partial B} = \alpha(G_{cII} - G_{cI})B^{\alpha-1}, \quad \frac{\partial \tau_0}{\partial B} = \frac{\alpha(\tau_{0II}^2 - \tau_{0I}^2)B^{\alpha-1}}{2\tau_0} \quad (4.5)$$

Putting the derived relations into Eq. 4.1 the cyclic damage formula reads:

$$\frac{dD^e}{dN} = \frac{1}{2G_c} \frac{\partial a}{\partial N} \left[\left(\frac{\tau_0}{G_c} \frac{\partial G_c}{\partial B} + \frac{\partial \tau_0}{\partial B} \right) \lambda \frac{\partial B}{\partial \beta} \frac{\partial \beta}{\partial a} + \tau_0 \frac{\partial \lambda}{\partial a} \right] \quad (4.6)$$

In equation 4.6, only two terms are left to be calculated; $\partial \lambda / \partial a$ and $\partial \beta / \partial a$. Both of these values are calculated from the numerical solution for displacement. The derivative of λ and β in the direction of the crack growth is same as the derivative with regards to x direction at the crack coordinate system.

4.4 Numerical Implementation

Before fatigue calculation, the problem has to be solved for static loading in order to allow the cohesive zone to extend until the crack-tip stress equals the critical traction. A mixed mode criterion used here to calculate the mixed mode critical traction τ_0 from formula 3.16. After the CZM expanded, the displacement field, tractions and the ERR are used to calculate the fatigue damage at every node. As described in the previous chapter, the static damage is calculated at each node from the displacement of the extra degree of freedom which represents the contribution of that node to the crack opening. For the partial derivatives of β and λ , however, the values are calculated on the crack surface for the integration point of the cohesive stiffness since the derivatives are taken along the crack direction. The values of β and λ from two consecutive elements are used for the derivative calculation. The new damage after ΔN cycles is calculated using Eq. 4.6 result:

$$D_{N+\Delta N} = D_N + \int_N^{N+\Delta N} \frac{dD}{dN} dN \quad (4.7)$$

This damage does not include the static damage added during the quasi-static solution and the crack growth. The energy release rate from the quasi-static solver is set to be the maximum load value for the fatigue test G_0 which is kept constant during the whole fatigue simulation. It is suggested to use Paris law and the element length in order to define an approximate ΔN for the cyclic load envelope size.

$$\Delta N \approx \frac{l_e}{4c \left(\frac{G_c}{G_0}\right)^m} \quad (4.8)$$

The degradation of the material reduces the J-Integral value calculated from the CZ below the critical value. At this point, the quasi-static solver is responsible to grow the crack to return to the critical value G_0 . To propagate the crack, new crack segments are added to the cohesive zone. When the cohesive forces are reduced due to the fatigue degradation, the crack opening increases furthermore which adds to the static damage. Also, an addition of a new crack segments increases the static damage.

To overcome these issue, a correction scheme is proposed. In this scheme, when the crack is grown statically by incrementing Δa , the static damage growth is added only if the stress at the tip is lowered to the maximum allowed level, otherwise, the damage is rolled back to its previous state. The process is repeated by adding another

Δa until the stress criterion is reached and this damage is accepted and added. In this way, the self-triggered static damage during iterations is eliminated. However, this newly added static damage still has to be defined in terms of fatigue cyclic degradation. This is done by considering if the crack is growing only by fatigue and the extra damage calculated in the previous step is used to find an equivalent number of cycles that would cause the same amount of damage. The equivalent number of cycles can be calculated when the cyclic crack growth rate is known:

$$\Delta N_s = \frac{dD_s}{\frac{dD}{dN}} \quad (4.9)$$

It should be noted that this number is different on each element in the cohesive zone and in the present simulation, the damage of the node at the physical crack-tip is selected since that is the node that goes through the maximum cyclic load alteration. The algorithm is summarized in the box below for the solution after the quasi-static solver is finished and the system is in equilibrium. The flowchart for the solver is presented in Fig. 4.2.

Algorithm 1: Cyclic CZM

- 1 Read the results of the quasi-static solution (ERR (G), maximum damage, displacement)
- 2 Calculate $\frac{dD}{dN}$ from Eq. 4.6, update total damage
- 3 Save the value of damage (damage T)
- 4 Add cycle number by cycle envelope ΔN ,
- 5 Iterate N-R. Calculate G after equilibrium reached
- 6 If G is dropped larger than 2%, role back the new damage (damageT+1) to damage T. Grow the crack, go to 5
- 7 If G is equal or larger than loading ERR (the constant G at which the fatigue is calculated) update the crack damage T=damage T+1, find the damage growth at the physical crack tip
- 8 Calculate the equivalent number of cycles due δD_{static} (ΔN_{eq}), cycle = cycle+ ΔN_{eq} , $\Delta a = crackgrowth$, $\frac{da}{dN} = \frac{\Delta a}{cycle}$.
- 9 If number of cycle reached the maximum number of cycles end, else go to 2

4.5 Tests

Simulations for a double cantilever beam under constant fatigue loading G was conducted for mode I, II and 50% mixed mode for a carbon-epoxy fibre laminate with

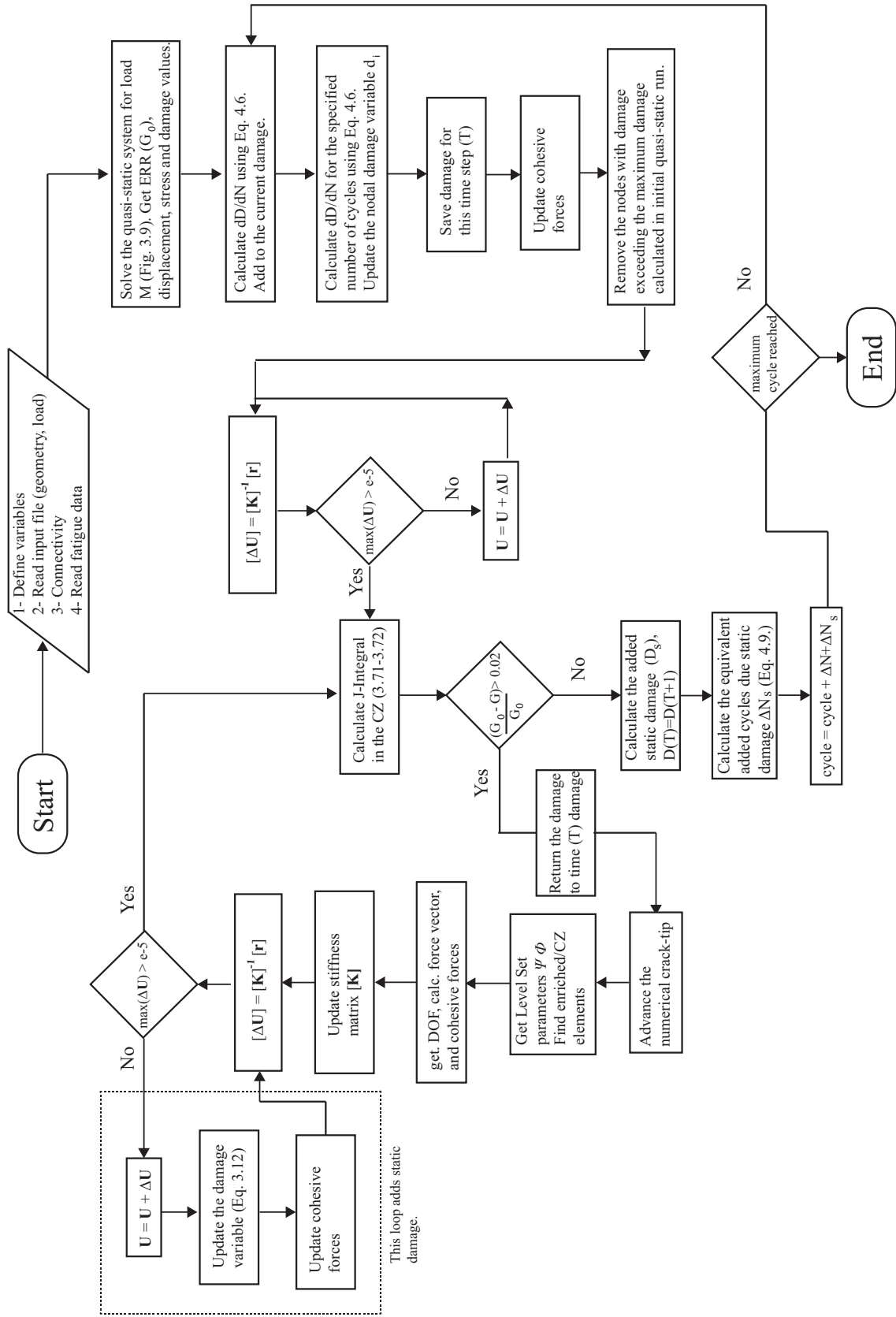


Figure 4.2: The flowchart for high-cyclic fatigue solver. This code is run after the quasi-static solver has converged initially so that the ERR and cohesive zone length are known for the load M. Here an energetic criterion is used rather than stress at the crack-tip.

the properties presented in the Table 4.1. Constant energy release rate was produced by moments applied on the plies as depicted in Fig. 3.14.

Table 4.1: Material properties and Paris law constants for HTA/6376C carbon/epoxy[10]

E_{11}	120	(GPa)	G_{Ic}	0.26	(kJ/m ²)
$E_{22}=E_{33}$	10.5	(GPa)	G_{IIc}	1.002	(kJ/m ²)
$G_{12}=G_{13}$	5.30	(GPa)	τ_{I0}	30	(MPa)
G_{23}	3.5	(GPa)	τ_{II0}	60	(MPa)
$\nu_{12}=\nu_{13}$	0.3	-	α	2.73	
ν_{23}	0.51	-			
C_I	0.0308	(mm/cycle)	m_I	5.4	
C_{II}	0.149	(mm/cycle)	m_{II}	4.5	
$C_{50\%}$	0.25	(mm/cycle)	$m_{50\%}$	6.3	

The beam consists of two laminae, both with E_{11} in x direction along the fibres and the crack and E_{22} in y direction. Each test is done for an initial crack length of $a = 10mm$. The thickness of each ply is $1.5mm$. The test is run for element sizes from $0.02mm$ to $0.09mm$. For small loads, the size of the cohesive zone is very small and high mesh intensity is needed to have enough elements in the cohesive zone. An envelope load size is chosen according to the magnitude of the load (equation 4.8) and the total number of cycles are selected such that the crack will advance one third to half the full cohesive zone size ($\approx 0.5mm$).

4.6 Results

The crack advances under cyclic loading are depicted in Fig. 4.3 for mode I crack opening. In this figure, the damage is plotted at each time the solver converged. When the system is at equilibrium, the cyclic damage for the next envelope of load is calculated and added to the current values of damage. Since the total damage has increased, the cohesive forces change and the system is no longer in equilibrium. Newton-Raphson solver is run again and a new ERR and damage (quasi-static solver adds static damage) are calculated. For the nodes at the physical crack-tip that exceed the maximum damage (in Fig. 4.3 it is about 0.35), the nodal damage is set to 1.1, which automatically makes the cohesive forces zero on that node. In order to

build up ERR again, the crack must grow. The physical tip is just before the point where the damage jumps to 1.1.

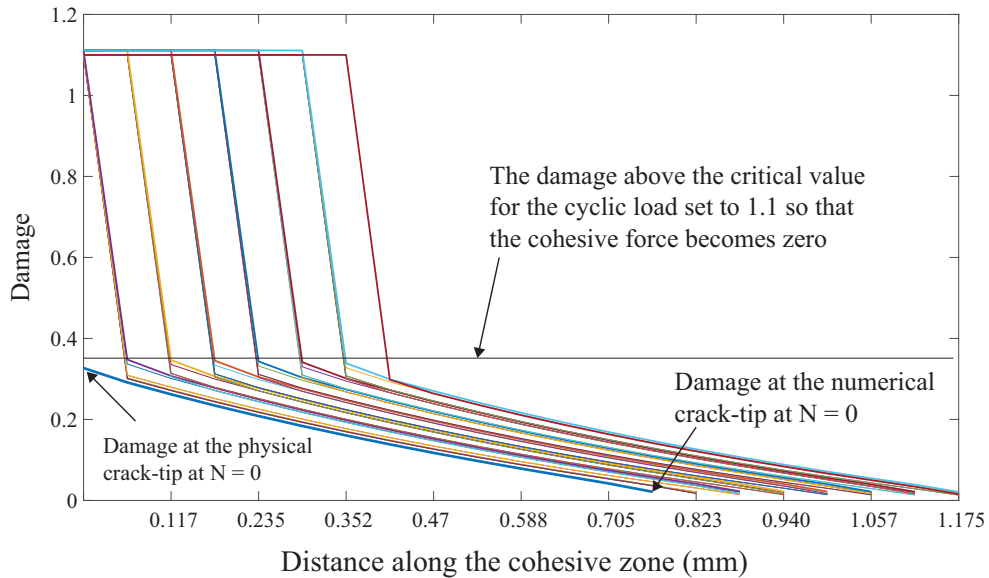


Figure 4.3: Mode I damage plots for 400 cycles with 10 cycles envelope loading. Applied load $G_I = 0.14kJ/m^2 = 0.538G_c$ and $l_e = 1/17mm$ mesh size. The crack has grown 7 elements which is $0.001029mm$ for each cycle.

The pattern in Fig. 4.3 shows a consistent and neat advance under cycles. This happens when an appropriate number of cycles per iteration is used. Apparently, very small load envelopes cannot be used since it will require hours of computer time to grow the crack slightly where on the other hand, too large load envelopes will cause a sudden increase of the damage and the solver struggles to develop a similar cohesive zone pattern with the same length. The length of the cohesive zone is a very important factor in the accuracy of the solver. As long as the length is consistent and the curvature of the crack surfaces are not changed significantly, the crack can grow in a self-similar way.

Fig. 4.4 is a plot of the cohesive traction taken from the cohesive force vector. Basically, this force is calculated from the damage which mirrors the effect; the damage is zero at the numerical crack-tip which has the maximum traction. Since the specimen is under-loaded, the cohesive zone is not fully developed and as it can be seen from 4.4 plot, the traction starts at about 20 MPa at the physical crack-tip and reaches 30 MPa at the numerical tip, which is the maximum traction the interface

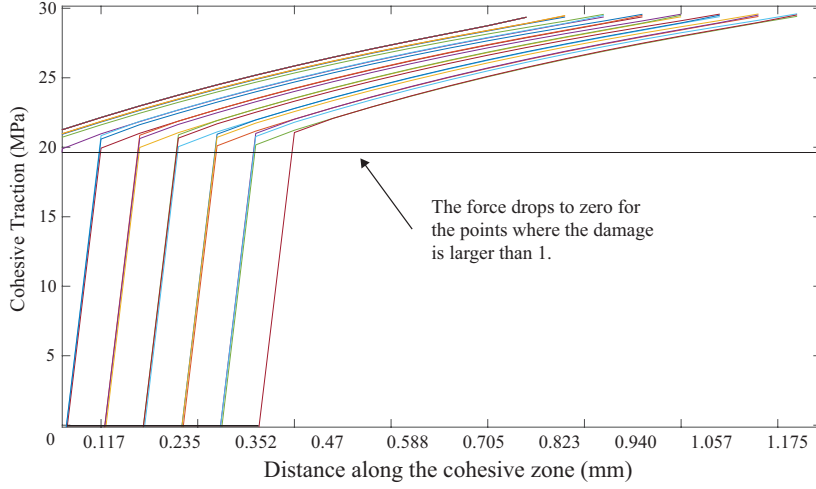


Figure 4.4: Mode I cohesive forces plots for loading $G_I = 0.14kJ/m^2 = 0.538G_c$ and for $l_e = 1/17mm$ mesh size.

can sustain. Fig. 4.5 is the cyclic crack growth rate plotted along Paris law results and experimental data [10] for the present specimen. High mesh intensity was used throughout all simulations to keep the consistency of the results. There are discrepancies for all data points in the graph and it is more visible when a larger cycle gap exist between runs.

Sources of error

The cyclic damage degradation formula 4.6 has parameters that are calculated from the crack opening displacement data; $\frac{\partial \beta}{\partial x}$ and $\frac{\partial \lambda}{\partial x}$. For mode I test the first derivative is zero but the second derivative is dependent on the cohesive zone crack surfaces curvature. This value is not constant along the cohesive zone. In other words, the crack surfaces in the cohesive zone are not straight lines and have curvature. The curvature is close to zero at the numerical crack-tip (smooth crack closure at the tip) and higher near the physical crack-tip. As a result, the cyclic fatigue damage is not constant along the cohesive zone. This curvature also governs the energy release rate calculation by J-Integral since it has the same terms. The points closer to the physical crack-tip degrade faster and as a result, those points are released earlier and the CZ gradually shrinks. On the other hand, the cohesive zone must stay in equilibrium with the external load so larger curvature compensates the energy release rate reduction.

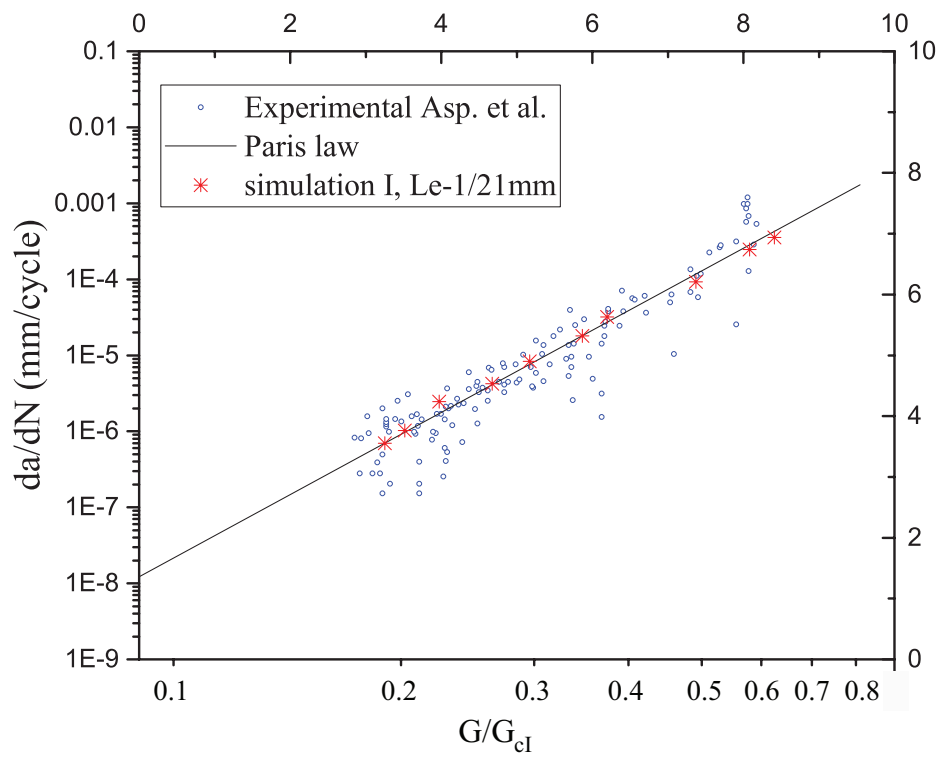


Figure 4.5: Mode I crack growth rate for experimental [10], Paris law and the simulation results.

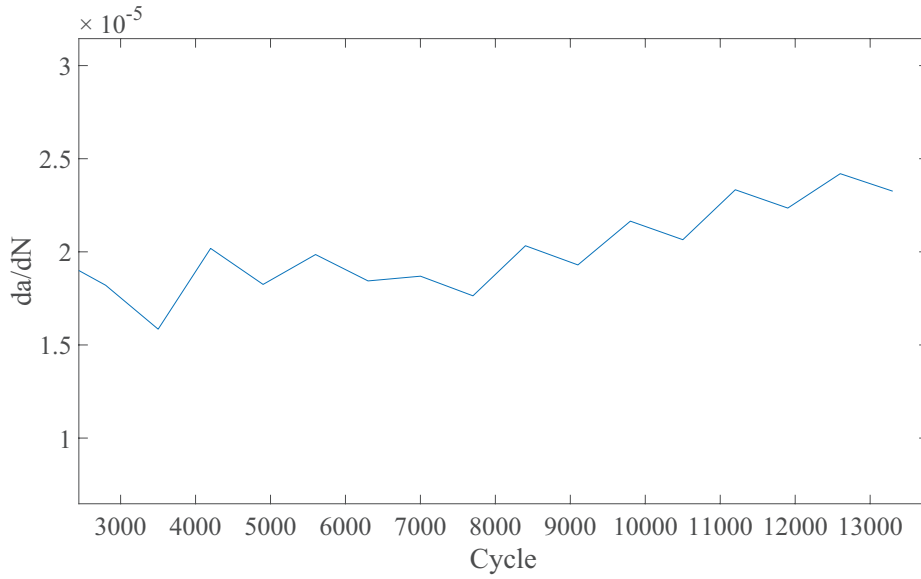


Figure 4.6: Mode I damage plots for 14000 cycles with 700 cycles envelope loading. Applied load $G_I/G_c = 0.38$ and for $l_e = 1/21mm$ mesh size

The cohesive zone shrinks and becomes more curved.

In order to illustrate the effect, large load envelopes were chosen for the simulation. In Fig. 4.6, the value of the crack growth rate for a large number of cycles is shown. Although the magnitude of the changes is of order 10^{-5} , it can be seen that the crack growth rate gradually increases. The oscillations in the results are probably stemming from the way the nodes at the physical tip are released during iterations. To be more precise, the growth of the numerical tip (which is explicitly added to the crack) and the growth of the physical tip (which is the release of the nodes automatically when the damage exceeds the maximum value) are not synchronous. Figure 4.7 shows the distribution of the fatigue damage along the cohesive zone over one iteration. The closer to the physical crack-tip, the larger the cyclic damage becomes.

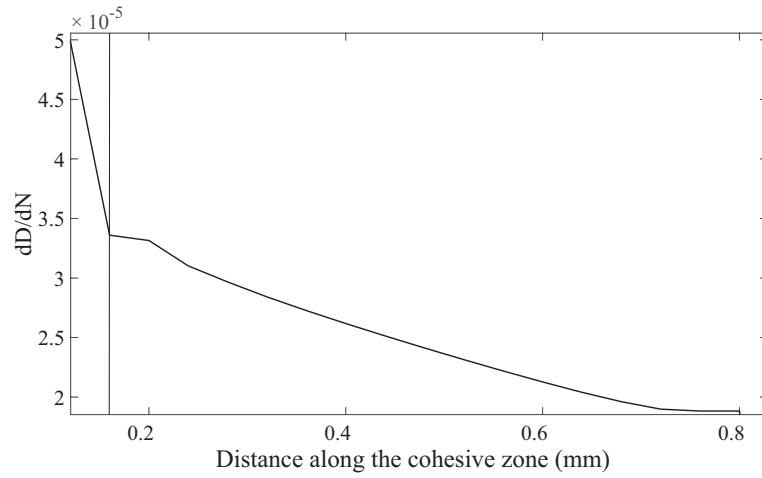


Figure 4.7: Mode I rate of fatigue damage per 100 cycles. Applied load $G_I/G_c = 0.452$ and for $l_e = 1/25mm$ mesh size.

Mode II results

Mode two test showed a similar pattern to the first mode crack opening. Since the growth rates are higher than mode one case, in mode two smaller number of cycles in each time step is recommended. Same mesh densities are used for this test as well.

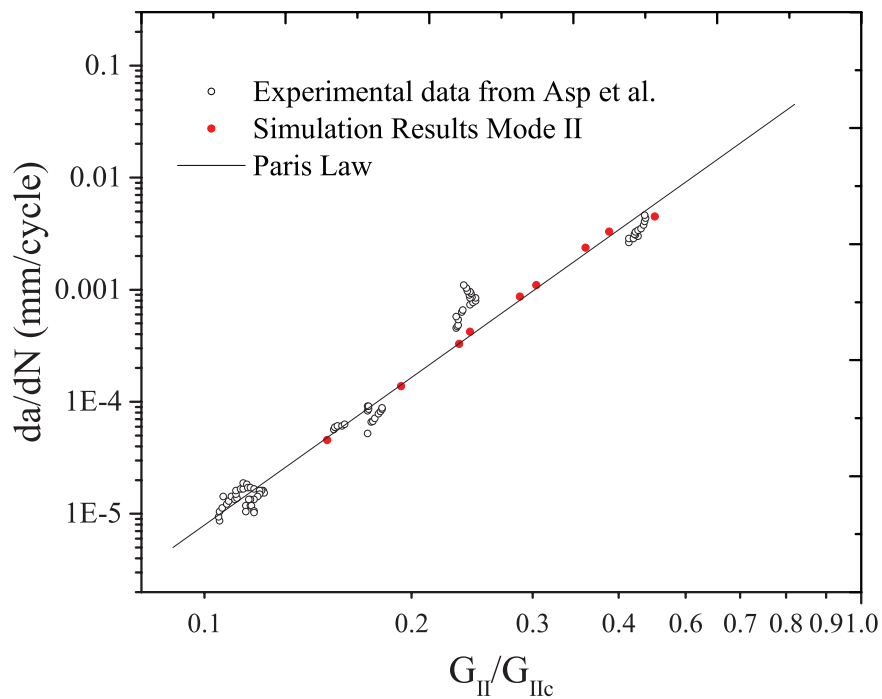


Figure 4.8: The results for Mode II simulation, Paris law and experimental data [10]

Mixed mode case

Mixed mode loading is again created by applying moment M on one ply and $0.0707M$ on the other one. Fig. 4.9 shows that this simulation has much more error than the other two.

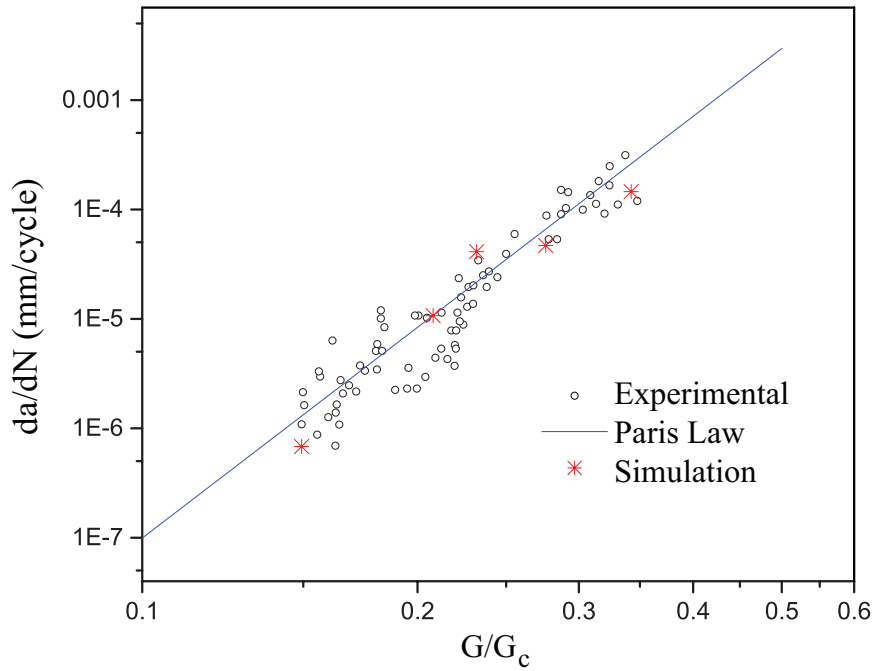


Figure 4.9: Mixed mode 50% crack growth rate for $l_e = 1/21$ mm mesh size

Not only the non-uniform fatigue damage along the CZ cause larger degradation closer to the physical crack-tip, now the mode mix ratio β is also affected by the change of slope along the cohesive zone. This trend is also illustrated in Fig. 4.10.

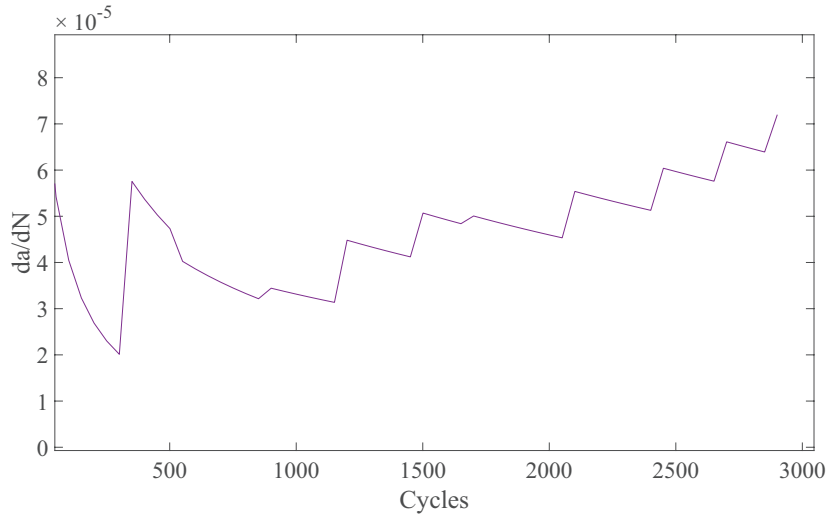


Figure 4.10: The crack growth rate under constant loading changes due cyclic loading

4.7 Conclusion

A new cyclic cohesive zone model was developed for XFEM implementation. The fatigue analysis revealed that the CZ base fatigue model does not predict uniform degradation rate along the CZ. This happens because the derivative of the crack opening and the mode mix ratio are not constant along the CZ. Also, it is obvious that different points in the CZ do not undergo same loading cycles and hence the assumption of similar degradation is not accurate. The partial derivative of the crack opening in x_1 direction increases away from the numerical crack-tip and toward the physical crack-tip. This ends in a higher prediction of the crack growth rate. Another factor in the excess prediction for fatigue crack growth is the unwanted static crack growth. An approach was proposed in order to correct the number of cycles by calculating an equivalent number of cycles that cause same static damage. The scheme increased the accuracy but the problem with the CZ size shrinkage still remains. Although the results show good conformance with experimental and Paris law, the results are transient.

Chapter 5

Conclusion

5.1 Contributions

The aim of this project was to address some of the analytical and computational aspects of composite fracture modelling in XFEM and to develop more efficient numerical tools. The literature review draws a map for the available analytical and computational methods and it highlighted that although XFEM has great potential for the simulation of structured materials, there has been no application of it for high-cyclic fatigue analysis. The study also emphasises the shortcomings of LEFM in addressing the composite fracture. This review guided the study first to the investigation of the fracture mechanics parameters and second to the application of a combined damage and fracture mechanics approach.

In the first modelling attempt, J-Integrals as the most prominent approach for crack characterisation in FEM and XFEM were investigated. The aspects and implication of using J-Integrals in the form of contour area integrals for the structured material are investigated for a $[0/90]$ CFRP laminate.

In the third chapter, the implementation of a cohesive zone model in XFEM is provided. To match the discontinuity definition of XFEM, a traction-separation law used in this implementation that does not govern the undamaged material. This turns out to be challenging in both quasi-static and fatigue simulations and necessary solutions are provided for the code implementation. Furthermore, the code is developed such that individual damage variable as well as the cohesive force are assigned to each node of the cut elements. The interpolation of these variables gives the damage and cohesive forces on the crack surfaces.

Another advantage of the CZM is that the J-Integral in a cohesive zone does not have to be integrated on a contour outside the cohesive zone and the problems of interaction with other discontinuities are avoided. CZM allows the crack characterisation with minimum interference with the structural details of the composites.

In the fourth chapter, a cyclic cohesive zone model is developed by linking the thermodynamic damage to the crack growth rate from a Paris law variant. This is the first implementation of a high-cyclic fatigue simulation by means of CZM in XFEM. The model is used to study the delamination of a DCB under cyclic loading for three different crack opening scenarios.

5.2 Conclusions

The study of the ERR for a transverse crack in a $[0/90]_s$ CFRP laminate (Chapter2) was carried out for displacement loading in 90° ply fibre direction in FEM and XFEM solvers. The conclusions can be summarized as follows:

- The energy release rate for a transversal crack in a $[0/90]_s$ laminate under unidirectional loading increases until about 80% of the specimen thickness and the ERR drops sharply until it reaches zero at the interface. This can mean the crack will arrest before reaching the interface however, the normal stresses at the interface caused by the transversal crack can be high enough to trigger delamination.
- It became clear that the area integrals should not be used unless the displacement field in the contour not disturbed by another discontinuity. The results for the current area J-Integrals are reliable as long as there is an analytical solution for the crack which is not always easy when interfaces and inclusions exist. The alternative is to refine the mesh whenever possible to avoid overlap of contour in the interfaces. For the $[0/90]_s$ laminate test in both FEM and XFEM, extremely fine mesh was required to capture the ERR near the interface. Considering the components scale in the composite structures, conventional contour and area integrals for ERR evaluation struggle for many crack settings.

- The techniques for the crack-tip stress field corrections such as quarter-point element or crack-tip enrichments in XFEM does not improve the results of J-Integrals and in fact, causing more complications when it comes to analysis of layered materials.

For the cohesive zone model implementation for the quasi-static test, two sets of Newton-Raphson iterative scheme were implemented in MATLAB for load-controlled and displacement-controlled simulations of Double Cantilever Beam delamination tests. The DCB tests for Mode I, Mode II and 50% Mixed mode crack opening were tried and the following conclusions can be made:

- The displacement of the extra degrees of freedom on each node on an enriched element shows the contribution of that node on the crack opening and can be used to define the damage on each node.
- By partially enriching the crack-tip element, the stress distribution can be corrected at the crack-tip. A technique for partially enriching the element is developed and the result show less stress oscillation at the tip.
- A wide range of stiffness can be used for the cohesive crack when using Newton-Raphson solution. The choice for the stiffness can affect the convergence speed. First, the slope of the traction separation locus was used for the stiffness. Although faster convergence might be achieved, this negative value causes instability for cohesive zones close to maximum size. On the other hand, a penalty stiffness matrix or a degraded form of it can be used. It should be noted that very high stiffness causes the maximum traction stay before the numerical crack and the cohesive zone becomes like the case where undamaged material exist ahead of the crack-tip.
- In the load-controlled DCB test, the size of the cohesive zone was checked against the analytical solutions for slim bodies. The results only conform to an order of magnitude. This was observed by several other numerical implementations [56, 137].
- For the displacement controlled test, the outcome shows that for the current implementation of the CZM in XFEM, the results are accurate for mesh almost

twice as intense as similar FE implementations. This shows that using one integration point for cohesive stiffness calculation might not be sufficient.

The Newton-Raphson solver was used for fatigue solution in the last chapter for high-cyclic loading. Again, DCB tests for high-cycle fatigue are used and the results are compared to experimental results. The outcome shows conformance only in a transient way. It was also observed that the choice of the load envelope size has an impact on the results. Following conclusions can be made for the last study:

- Using Paris law to build a cyclic cohesive zone degradation model is not without problems. The LEFM based approaches see the crack-tip as a point which goes through a cyclic load. In CZ, a number of the points in the CZ go through different load magnitudes and different rates of damage evolution is observed.
- For high cyclic fatigue, a pocket of several load cycles has to be defined. When implemented numerically, this method causes non-smooth change of the damage variable. To grow the crack in this way, a lot of static damage is produced during the quasi-static solution which is undesirable. A correction scheme was proposed that uses the added static damage to calculate an equivalent number of cycles that can produce that much damage if they were created by fatigue.
- Both the crack opening and the mode mix ratio partial derivatives are not constant in the cohesive zone. In the mix mode case, modelling did not succeed because of severe non-linearities caused by these inconsistencies.
- Using cycle correction schemes, such as the one used in this study, or using different cycles on different points in the cohesive zone [14] can improve the results for the final crack growth rate but it does not consider the cohesive zone as a real entity ahead of the crack.

5.3 Suggestions for future studies

The code developed here was primarily implemented for delamination modelling. The program can be expanded to more diverse combinations of discontinuities and cracks in composites. The present study is limited to the condition that the crack travels in a straight line. This was decided because of the available researches on cyclic CZM

that could be used for verification. In addition, the subject of fatigue crack growth in composites still lacking a dedicated theory and an analytical tool regarding both the distribution, direction and growth rate for the cracks.

Another reason for choosing delamination for CZM model is that it is a distinct discontinuity (regarding the scale it happens) in a composite structure. This allows the fracture theories be applied in a conventional way. To be more accurate, the fatigue loading triggers many more degradation processes in the material and depending on the scale of the observation, a more specialized fatigue model for composites are needed. XFEM ability to include numerous discontinuities -such as the model proposed by [114]- is an excellent opportunity for development of a fatigue model that is more relevant to the composite structures. Instead of singling out one crack, a distribution of small cracks can be considered based on experimental results on fatigue crack density in the material in a more damage based approach.

As it is mentioned already, linking the CZM with the fatigue laws are not completely accurate since the mapping of the degradation of different points in the cohesive zone to the Paris law results in different degradation rates across the CZ. There is a good opportunity for an experimental study to find out the effect of fatigue loading on the cohesive zone shape and to see if the size of the cohesive zone shrinks as it is predicted by the model or not.

Appendix A

Simulation of microcracks in 3D printed parts built by selective laser sintering (SLS) using XFEM

A.1 introduction

Voids and inclusion modelling in XFEM is quite straight forward using powerful level set method. In order to demonstrate the flexibility and applications of XFEM, in this appendix an analysis of microcracking in SLS 3D printed parts is provided which involves modelling of both strong and weak discontinuities. The weak discontinuities in these parts are caused by un-melted particles which affect the onset and propagation of microcracks. Different particle density and different patterns of particle distribution in the material are modelled using circular inclusions in order to characterise the effect of them on the crack behaviour. The numerical implementation and code preparation for this study was carried out by the author and the outcomes are published in [68]. The results are included with the consent of the authors of the paper.

A.2 Background

In 3D printing process, the part is built layer by layer, according to a CAD drawing's sliced model. In SLS, the initial material (Nylon 12 in this case) is spread in a powder bed while a laser beam melts the pattern of each slice (CAD cross section) onto the powder bed. When the material is solidified, one layer is created which is bonded

to the previous layer. This process repeats until the part is created. This process is disrupted by several factors causing inhomogeneity in the final product. Incomplete melting of the material results in the inclusion of un-melted particles in the layer. The existence of these particles can cause stress concentrations and crack initiation. There are several printing process factors that influence the density of the melted particles.

A.2.1 Degree of Particle Melt (DPM)

When the powder is exposed to laser beam, depending on the scanning speed and the energy of the laser, some parts of the powder do not melt completely and un-melted cores remain inside the scanned area. By scanning the printed part and measuring the areas and the temperatures of different crystallines in the part, the ratio between the un-melted cores and melted/re-crystallised material is achieved. [153]. These data are used to calculate the DPM which along the laser power parameter can be used for mechanical behaviour characterisation [88]. The higher the DPM the less un-melted cores which initially increases the strength but after an optimum value, when the material becomes almost single phase, the strength drops.

A.2.2 Part orientation factor

Since the part is built layer by layer, the material develops anisotropic properties in build direction than the powder bed plane. Also, the scanning pattern on each slice can cause directional properties and loss of the isotropic properties. There are studies on the anisotropic properties of SLS parts such as [3, 31]. Normally the parts are weaker in the build direction which is the result of inter-layer bonding mechanism. In this study, the inter-layer strength is not involved and the 2D test is done for isotropic surface for a printed layer.

Material properties

To be able to model the material, the two phase's mechanical properties are needed. The properties for Nylon-12 is taken from 3D System company presented in Table A.1. The Young's modulus for the un-melted part of the material is considered to be 10% higher than the melted material.

Table A.1: Nylon-12 properties from [134]

Mechanical property	value
Tensile Strength (MPa)	44
Tensile Modulus (MPa)	1600
Tensile Elongation at Break(%)	9
Part Melting Point(°C) (MPa)	184
Particle Size, average (μm)	58
Particle Size, range 90% (μm)	25-92
Part Moisture Absorption, 23°C(%)	0.41

A.3 Numerical implementation

The same *in-house* code as previous chapters is used for this study in isotropic mode. The code uses XFEM shifted enrichments for cracks and the weak discontinuities as described in chapter two section 2.6.1. The cores are defined as circular inclusions for simplicity using level set method. This level set is defined by the distance to the interface of the inclusion by measuring each node distance (and Gauss point distance for the enriched nodes) to the centre of the circle and subtracting the radius from it. The level set is negative inside the circle, zero on the circle and positive outside the circle.

$$\Phi_c = \sqrt{x_c^2 + y_c^2} - r \quad (\text{A.1})$$

x_c and y_c are coordinates of the nodes according to the inclusion's local coordinate system. For the integration of the stiffness matrix over the elements that contain the interface, the shape functions are multiplied by Φ_c . This will create a change of slope in the interpolation which will become a strong discontinuity when derivatives are calculated. In other words, the stiffness matrix is allowed to have a different strain on each side of the crack.

A.4 Tests

A.4.1 The effect of inclusion proximity on the crack behaviour

An inclusion disrupts the stress/strain field in its proximity. When it comes to the crack propagation, the properties and location of the particle can influence the crack direction, opening displacement/mode and other characteristics. The first test is

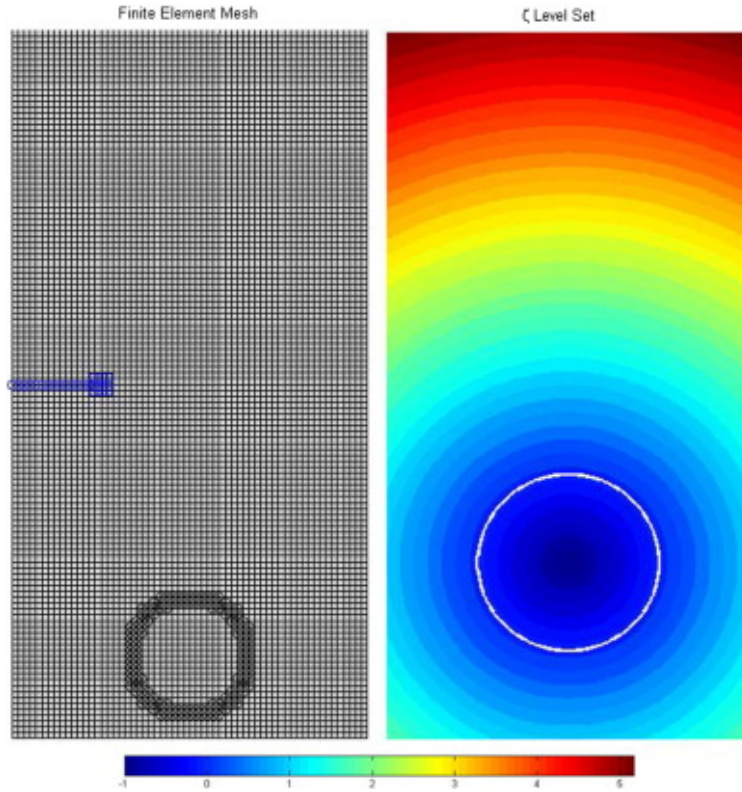


Figure A.1: The crack and the inclusion in the element domain and the level set value for the inclusion (right)

designed to investigate the impact of the inclusion location and its stiffness on the crack propagation under plane strain state. Fig. A.1 shows how the un-melted particle is defined as an inclusion. The size of the particle is used as a characteristic length for the specimen and all dimensions are described using the diameter of the inclusion. The height is 6 times, width 3 times and the element side length is 1/20 times the inclusion diameter. The initial crack length was set 0.75 and grown by length of 0.1 on each step (ten runs for the crack extension were used). The results show that the crack growth direction significantly affected by the proximity of the inclusion. The crack tries to get away from the inclusion and this pattern is hastened when the inclusion is moved closer to the crack initial place (Figs. A.2 to A.4).

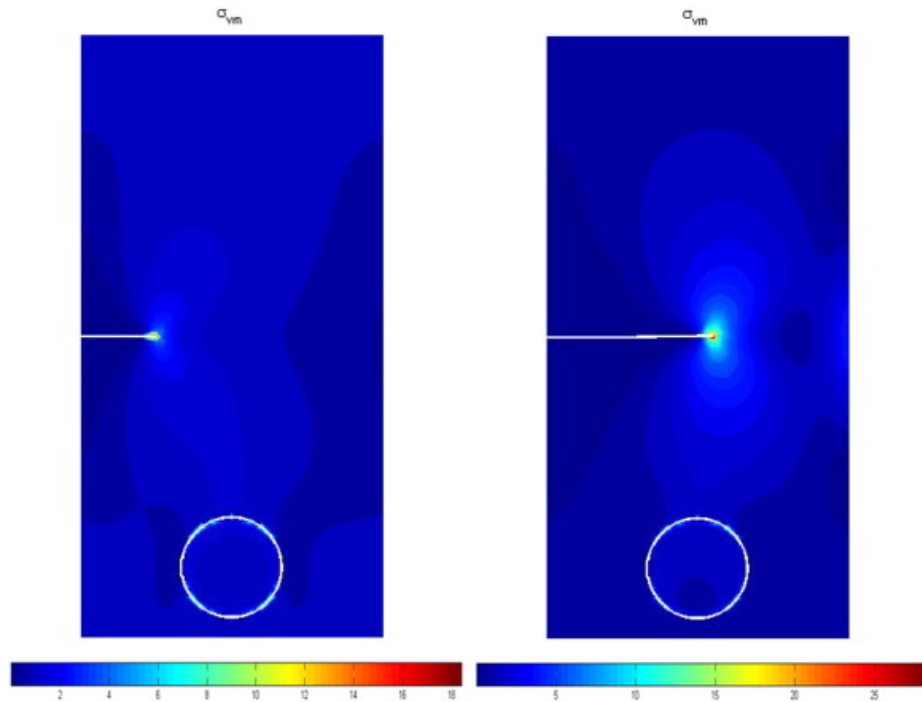


Figure A.2: Von-Mises stress (MPa) and crack evolution for inclusion far from the initial crack

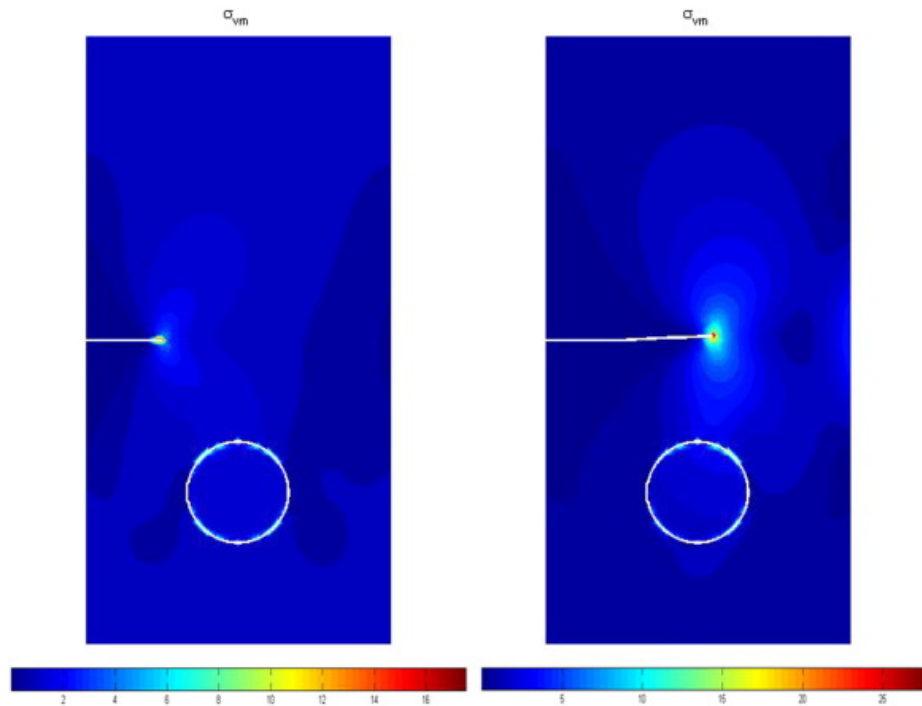


Figure A.3: Von-Mises stresses (MPa) for un-melted particles at (1.5, 1.5), radius=0.5

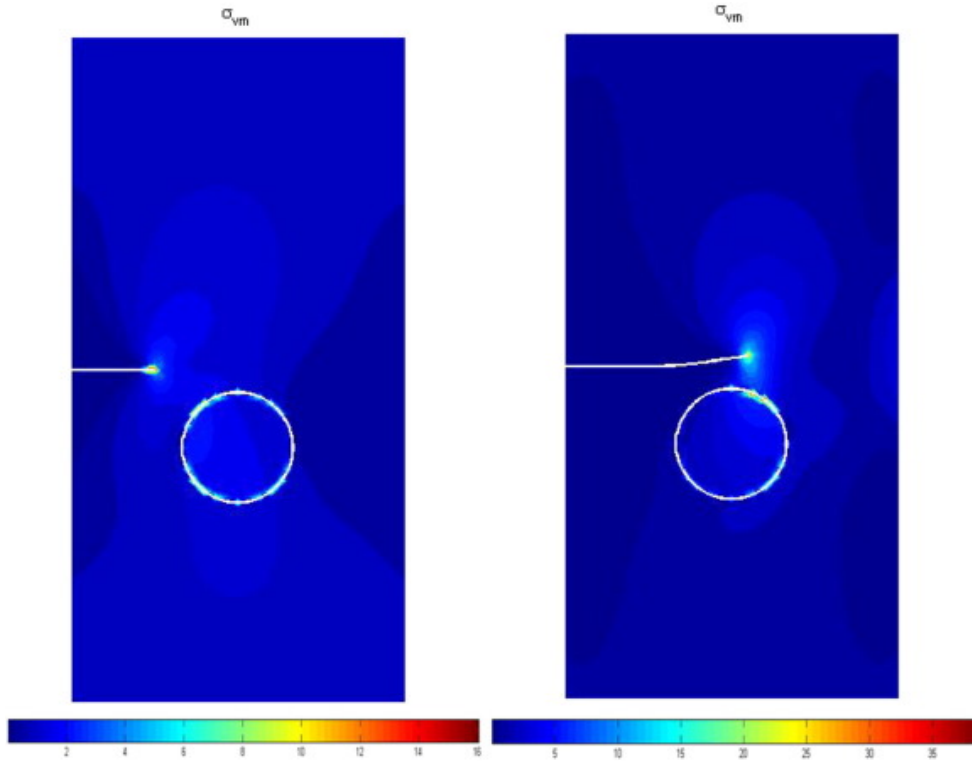


Figure A.4: Von-Mises stresses (MPs) for Un-melted particles at (1.5, 2.3), radius=0.5. The crack tries to avoid the inclusion with higher Young's modulus

Another observation that can be made from this test is that the interface stresses at the particle interface tend to increase when the crack nears the inclusion.

A.4.2 The crack behaviour between two adjacent inclusions

The second scenario is when the crack approaches two particles at a close distance to each other. The initial crack is again 0.1 times the size of the inclusion diameter and this time it passes through the gap between the two particles. This test is designed to find out if the two adjacent inclusions act as stress concentrators and guide the crack through the gap. This time, height=8, width = 4 and element size is 1/40 times the particle diameter. One element cannot have both crack and inclusion enrichments and for this reason and the proximity of the two inclusions the mesh size had to be decreased to allow enough elements for clear stress distribution evaluation. Also, a smaller crack increment size ($\Delta a = 0.05$) is used to allow tracking fine changes in the crack pattern. The test results show that the crack leans toward the gap and passes through the corridor between the two inclusions Fig. A.5. This effect of two adjacent

Part Bed set-point	Scan speed	Scan spacing	Laser power
149°C	5000 mm/s	0.15 mm	11 W

Part Bed set-point	Scan speed	Scan spacing	Laser power
148°C	6300 mm/s	0.15 mm	9.5 W

particles can be interpreted as a weakening parameter for the material as it would accelerate the crack growth.

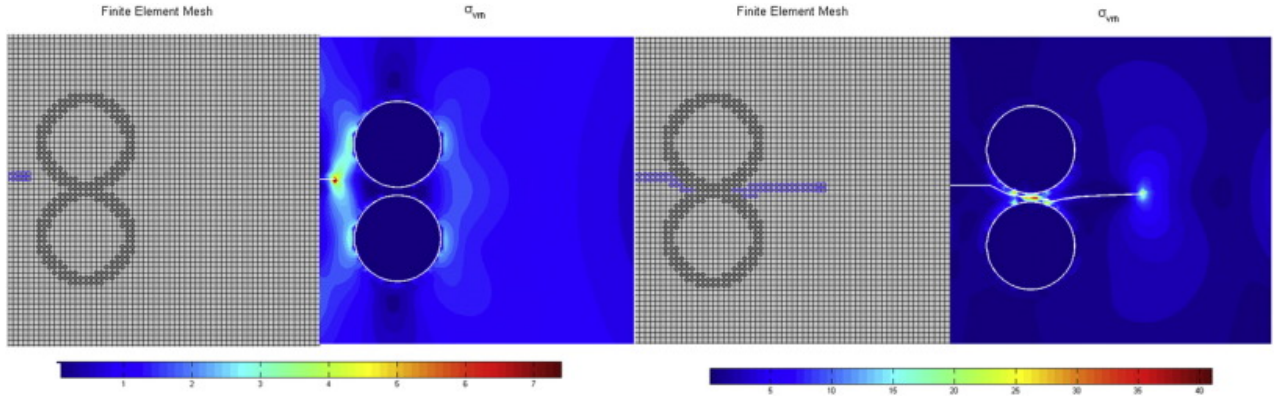


Figure A.5: The enrichment of finite element and Von-Mises stresses (MPa) for initial crack (left) and the grown crack after 40 iterations (right)

A.4.3 Simulation of the cross section of SLS print

In this simulation the real structure of an SLS part is tried based on the same test setting this time by using the parameters and the inclusion pattern from experiments [62]. The test is done for two specimens that are printed with different build parameters. The specimen in Fig. A.6 is printed using settings in Table A.2.

In Fig. A.7, same test is carried out with different printing setting provided in Table A.3. Different build parameters results in different density/size of un-melt particles.

The crack in the specimens in Fig. A.6 and A.7 were allowed to grow until the part failure when the crack reaches the specimen edge. It can be seen in both figures, the crack initiates where the particles are closest to each other. For the first case, 25 iteration led to failure while in the case of Fig. A.7, 27 iterations occur before failure. Since the crack advance is set constant, less iteration to failure means the

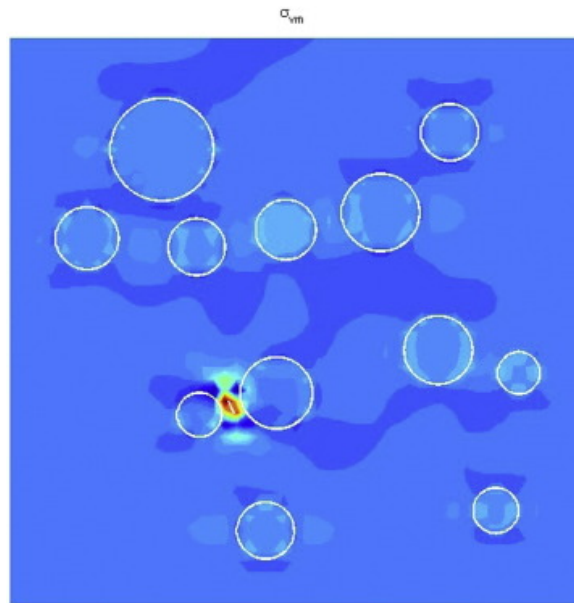


Figure A.6: Crack initiation in SLS printed Nylon-12 specimen based on table [A.2](#) setting

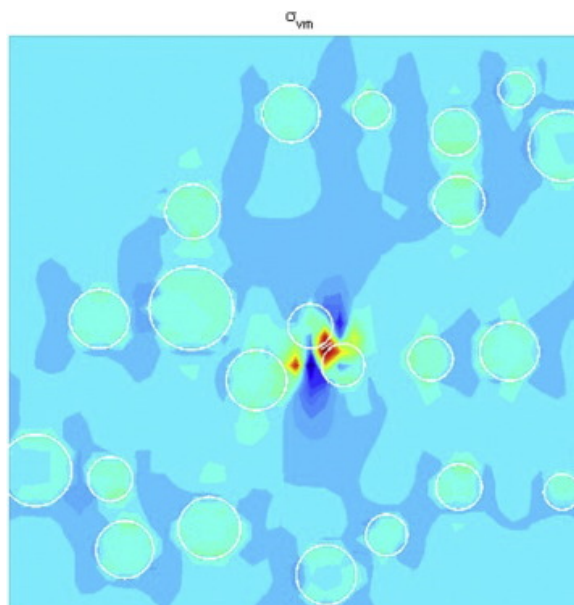


Figure A.7: Crack initiation in SLS printed Nylon-12 specimen based on table [A.3](#) setting

crack has travelled a shorter distance in the material. The unbalanced distribution of the inclusions in Fig. A.8 has resulted in the crack to travel downward faster and large particles on the upper side have prevented the crack grow to the edge. 9 plots of different crack growth state during crack initiation until the total failure is depicted in Figures A.8 and A.9. Figure A.8 shows that when the particles are larger, they cause more curvature in the crack path and in Figure A.9 one can see that the crack tends to travel more in straight line although it starts in a less vertical direction but it quickly align itself vertically normal to the loading direction.

Considering the scan speed of the two cases, it seems that higher speed scanning creates smaller particles with spread in the specimen but in larger number. From the crack growth pattern, it seems that larger particles tend to impede the crack more and in Fig.A.8, the crack has reached the lower edge much faster than the upper edge. This unbalanced condition caused this specimen to fail earlier. On the other hand, the larger particles seem to cause more curvature in the crack path which means they have a more magnifying effect. This might increase the probability of crack initiation near large particles and cause reduction of load bearing capacity.

A.5 Conclusion

Here, the effect of the particle on the crack propagation and the stress field is studied. The simulation showed that the existence of un-melted particles in Nylon-12 parts created by SLS 3D printing cause significant changes in the crack behaviour. It seems that when a particle with higher Young's modulus exists in the domain, it tends to push away the crack. The crack proximity to the inclusion amplifies this trend. When the crack is close to a particle, high stresses are experienced on the interface of the particle.

Uneven distribution of the particles sizes and locations can cause faster crack growth in one direction and earlier failure. Although larger particles might impede the crack growth, they cause more stress gradients near their boundaries and might ease crack onset. In addition, the stress analysis showed that the onset of crack is more probable between very close particles.

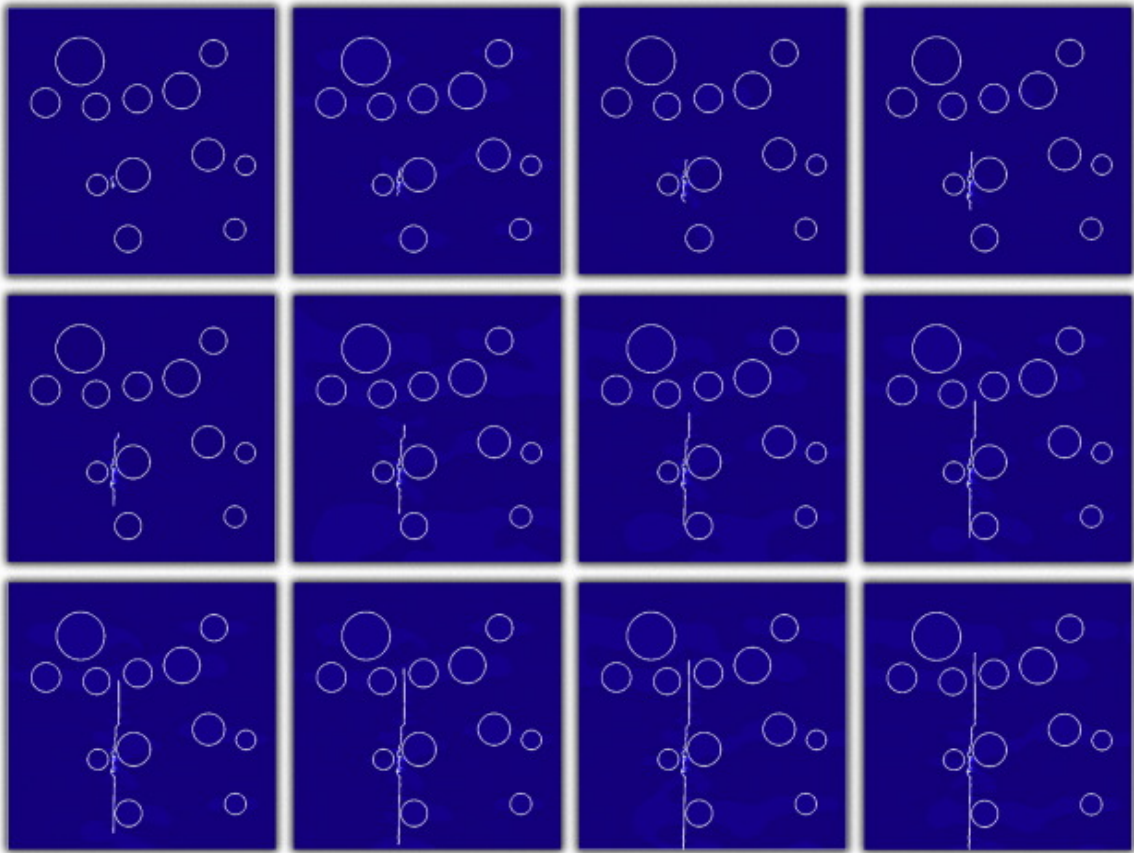


Figure A.8: Crack progression in SLS printed Nylon-12 using scan variables in table [A.2](#)

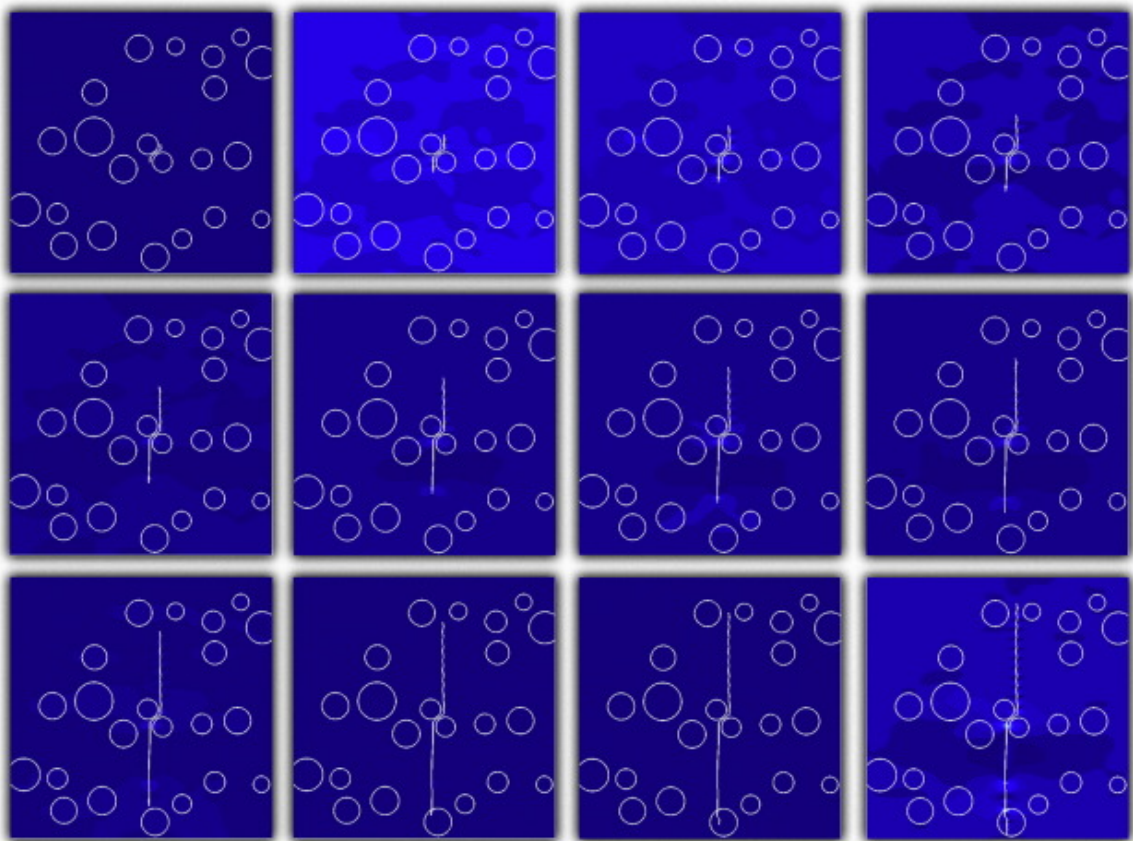


Figure A.9: Crack progression in SLS printed Nylon-12 using scan variables in table [A.2](#).

Bibliography

- [1] Composites in the airframe and primary structure
. <http://www.boeing.com/commercial/aeromagazine/articles/qtr-4-06/article-04-2.html>.
Accessed: 2017-12-24.
- [2] Hexcel composites, “hexply 8552,” february 2013. [online].
- [3] Uzoma Ajoku, Naguib Saleh, Neil Hopkinson, R Hague, and Poonjolai Erasenthiran. Investigating mechanical anisotropy and end-of-vector effect in laser-sintered nylon parts. *Proceedings of the Institution of Mechanical Engineers, Part B: Journal of Engineering Manufacture*, 220(7):1077–1086, 2006.
- [4] G Alfano and M_A Crisfield. Finite element interface models for the delamination analysis of laminated composites: mechanical and computational issues. *International journal for numerical methods in engineering*, 50(7):1701–1736, 2001.
- [5] MH Aliabadi. Boundary element formulations in fracture mechanics. *Applied Mechanics Reviews*, 50:83–96, 1997.
- [6] Olivier Allix and Alberto Corigliano. Modeling and simulation of crack propagation in mixed-modes interlaminar fracture specimens. *International Journal of Fracture*, 77(2):111–140, 1996.
- [7] Ted L Anderson. *Fracture mechanics: fundamentals and applications*. CRC press, 2017.
- [8] A Asadpoure and S Mohammadi. Developing new enrichment functions for crack simulation in orthotropic media by the extended finite element method. *International Journal for Numerical Methods in Engineering*, 69(10):2150–2172, 2007.

- [9] S Ashari and S Mohammadi. Delamination analysis of composites by new orthotropic bimaterial extended finite element method. *International Journal for numerical methods in engineering*, 86(13):1507–1543, 2011.
- [10] Leif E Asp, Anders Sjögren, and Emile S Greenhalgh. Delamination growth and thresholds in a carbon/epoxy composite under fatigue loading. *Journal of Composites, Technology and Research*, 23(2):55–68, 2001.
- [11] Satya N Atluri, Albert S Kobayashi, and Michihiko Nakagaki. An assumed displacement hybrid finite element model for linear fracture mechanics. *International Journal of Fracture*, 11(2):257–271, 1975.
- [12] I Babuška and Jens M Melenk. The partition of unity finite element method. Technical report, Maryland Univ. College Park Inst. for Physical Science and Technology, 1995.
- [13] Marie-Christine Baietto, Emilien Pierres, Anthony Gravouil, Bruno Berthel, Siegfried Fouvry, and Benoit Trolle. Fretting fatigue crack growth simulation based on a combined experimental and xfem strategy. *International Journal of Fatigue*, 47:31–43, 2013.
- [14] Brian LV Bak, Albert Turon, Esben Lindgaard, and Erik Lund. A simulation method for high-cycle fatigue-driven delamination using a cohesive zone model. *International Journal for Numerical Methods in Engineering*, 106(3):163–191, 2016.
- [15] Grigory Isaakovich Barenblatt. The mathematical theory of equilibrium cracks in brittle fracture. *Advances in applied mechanics*, 7:55–129, 1962.
- [16] Roshdy S Barsoum. Triangular quarter-point elements as elastic and perfectly-plastic crack tip elements. *International Journal for numerical Methods in engineering*, 11(1):85–98, 1977.
- [17] Z.P. Bažant and J. Planas. *Fracture and Size Effect in Concrete and Other Quasibrittle Materials*. New Directions in Civil Engineering. Taylor & Francis, 1997.

- [18] Ted Belytschko and Tom Black. Elastic crack growth in finite elements with minimal remeshing. *International journal for numerical methods in engineering*, 45(5):601–620, 1999.
- [19] Ted Belytschko, Yun Yun Lu, and Lei Gu. Element-free galerkin methods. *International journal for numerical methods in engineering*, 37(2):229–256, 1994.
- [20] Ted Belytschko, D Organ, and Y Krongauz. A coupled finite element-element-free galerkin method. *Computational Mechanics*, 17(3):186–195, 1995.
- [21] ML Benzeggagh and M Kenane. Measurement of mixed-mode delamination fracture toughness of unidirectional glass/epoxy composites with mixed-mode bending apparatus. *Composites science and technology*, 56(4):439–449, 1996.
- [22] Jean-Marie Berthelot. Transverse cracking and delamination in cross-ply glass-fiber and carbon-fiber reinforced plastic laminates: static and fatigue loading. *Applied Mechanics Reviews*, 56(1):111–147, 2003.
- [23] Sunil Bhat and Vijay G Ukadgaonker. Dugdale cohesive zone modeling to evaluate j integral at the interface of strength mismatched steels: A simplified numerical approach. *Finite Elements in Analysis and Design*, 46(7):601–610, 2010.
- [24] S Bhattacharya, IV Singh, BK Mishra, and TQ Bui. Fatigue crack growth simulations of interfacial cracks in bi-layered FGMs using XFEM. *Computational Mechanics*, 52(4):799–814, 2013.
- [25] A. Blázquez, V. Mantič, F. París, and L.N. McCartney. Stress state characterization of delamination cracks in [0/90] symmetric laminates by bem. *International Journal of Solids and Structures*, 45(6):1632 – 1662, 2008.
- [26] David Broek. *Elementary engineering fracture mechanics*. Springer Science & Business Media, 2012.
- [27] David Broek. *The practical use of fracture mechanics*. Springer Science & Business Media, 2012.

- [28] Pedro Ponces Camanho, CG Davila, and MF De Moura. Numerical simulation of mixed-mode progressive delamination in composite materials. *Journal of composite materials*, 37(16):1415–1438, 2003.
- [29] Alireza Chadegani, Chihdar Yang, and Stanley S Smeltzer III. Adhesive-bonded composite joint analysis with delaminated surface ply using strain-energy release rate. *Journal of Aircraft*, 49(2):503–520, 2012.
- [30] DL Chopp and N Sukumar. Fatigue crack propagation of multiple coplanar cracks with the coupled extended finite element/fast marching method. *International journal of engineering science*, 41(8):845–869, 2003.
- [31] William Cooke, Rachel Anne Tomlinson, Richard Burguete, Daniel Johns, and Gaëlle Vanard. Anisotropy, homogeneity and ageing in an sls polymer. *Rapid Prototyping Journal*, 17(4):269–279, 2011.
- [32] Michelle Leali Costa, SFM Almeida, and Mirabel Cerqueira Rezende. Critical void content for polymer composite laminates. *AIAA journal*, 43(6):1336–1341, 2005.
- [33] Brian Cox and Qingda Yang. In quest of virtual tests for structural composites. *science*, 314(5802):1102–1107, 2006.
- [34] M Doblare, F Espiga, L Gracia, and M Alcantud. Study of crack propagation in orthotropic materials by using the boundary element method. *Engineering fracture mechanics*, 37(5):953–967, 1990.
- [35] Abaqus Documentation and User Manual. Version 6.10. *Dassault Systemes*, 2010.
- [36] JOHN Dolbow and Ted Belytschko. A finite element method for crack growth without remeshing. *International journal for numerical methods in engineering*, 46(1):131–150, 1999.
- [37] John Dolbow, Nicolas Moës, and Ted Belytschko. Modeling fracture in mindlin–reissner plates with the extended finite element method. *International journal of solids and structures*, 37(48):7161–7183, 2000.

- [38] J.ST. Doltsinis, H. Knapp, P. Streiner, and H Wüstenberg. PERMAS-FM, Fracture Mechanics. *INTES GmbH, Stuttgart, User Manual, Publication*, (226).
- [39] C Armando Duarte and J Tinsley Oden. Hp clouds- A meshless method to solve boundary-value problem. *Texas Institute for Computational and Applied Mathematics, University of Texas at Austin, Technical Report*, pages 95–05, 1995.
- [40] Donald S Dugdale. Yielding of steel sheets containing slits. *Journal of the Mechanics and Physics of Solids*, 8(2):100–104, 1960.
- [41] Thomas Elguedj, Anthony Gravouil, and Alain Combescure. A mixed augmented lagrangian-extended finite element method for modelling elastic–plastic fatigue crack growth with unilateral contact. *International Journal for Numerical Methods in Engineering*, 71(13):1569–1597, 2007.
- [42] Fazil Erdogan. Stress distribution in a nonhomogeneous elastic plane with cracks. *Journal of Applied Mechanics*, 30(2):232–236, 1963.
- [43] Fazil Erdogan and GC Sih. On the crack extension in plates under plane loading and transverse shear. *Journal of basic engineering*, 85(4):519–527, 1963.
- [44] Fo Erdogan. Stress distribution in bonded dissimilar materials with cracks. *Journal of Applied Mechanics*, 32(2):403–410, 1965.
- [45] JD Eshelby. The continuum theory of lattice defects. In *Solid state physics*, volume 3, pages 79–144. Elsevier, 1956.
- [46] Michael L Falk, Alan Needleman, and J.R. Rice. A critical evaluation of cohesive zone models of dynamic fracture. In *Proceedings of the 5th European mechanics of materials conference on scale transitions from atomistics to continuum plasticity*, pages 43–50, 2001.
- [47] AJ Fawkes, DRJ Owen, and AR Luxmoore. An assessment of crack tip singularity models for use with isoparametric elements. *Engineering Fracture Mechanics*, 11(1):143–159, 1979.

- [48] M Fleming, YA Chu, B Moran, T Belytschko, YY Lu, and L Gu. Enriched element-free galerkin methods for crack tip fields. *International journal for numerical methods in engineering*, 40(8):1483–1504, 1997.
- [49] Thomas-Peter Fries and Malak Baydoun. Crack propagation with the extended finite element method and a hybrid explicit–implicit crack description. *International Journal for numerical methods in engineering*, 89(12):1527–1558, 2012.
- [50] Thomas-Peter Fries and Ted Belytschko. The extended/generalized finite element method: an overview of the method and its applications. *International Journal for Numerical Methods in Engineering*, 84(3):253–304, 2010.
- [51] F Garcia-Sanchez, R Rojas-Diaz, A Sáez, and Ch Zhang. Fracture of magneto-electroelastic composite materials using boundary element method (BEM). *Theoretical and Applied Fracture Mechanics*, 47(3):192–204, 2007.
- [52] Seyed Shahram Ghorashi, Navid Valizadeh, and Soheil Mohammadi. Extended isogeometric analysis for simulation of stationary and propagating cracks. *International Journal for Numerical Methods in Engineering*, 89(9):1069–1101, 2012.
- [53] Vinay K Goyal, Eric R Johnson, and Carlos G Davila. Irreversible constitutive law for modeling the delamination process using interfacial surface discontinuities. *Composite Structures*, 65(3):289–305, 2004.
- [54] Michael Griebel and Marc Alexander Schweitzer. A particle-partition of unity method for the solution of elliptic, parabolic, and hyperbolic pdes. *SIAM Journal on Scientific Computing*, 22(3):853–890, 2000.
- [55] A. A. Griffith. The phenomena of rupture and flow in solids. *Philosophical Transactions of the Royal Society of London. Series A, Containing Papers of a Mathematical or Physical Character*, 221:163–198, 1921.
- [56] Paul W Harper and Stephen R Hallett. Cohesive zone length in numerical simulations of composite delamination. *Engineering Fracture Mechanics*, 75(16):4774–4792, 2008.

- [57] Paul W Harper and Stephen R Hallett. A fatigue degradation law for cohesive interface elements—development and application to composite materials. *International Journal of Fatigue*, 32(11):1774–1787, 2010.
- [58] B. Harris. *Fatigue in Composites: Science and Technology of the Fatigue Response of Fibre-Reinforced Plastics*. Woodhead Publishing Series in Composites Science and Engineering. Elsevier Science, 2003.
- [59] TK Hellen. On the method of virtual crack extensions. *International Journal for numerical methods in engineering*, 9(1):187–207, 1975.
- [60] D Hemanth, KS Shivakumar Aradhya, TS Rama Murthy, and N Govinda Raju. Strain energy release rates for an interface crack in orthotropic media—a finite element investigation. *Engineering fracture mechanics*, 72(5):759–772, 2005.
- [61] Arne Hillerborg, Mats Modéer, and P-E Petersson. Analysis of crack formation and crack growth in concrete by means of fracture mechanics and finite elements. *Cement and concrete research*, 6(6):773–781, 1976.
- [62] N Hopkinson, CE Majewski, and H Zarringhalam. Quantifying the degree of particle melt in selective laser sintering®. *CIRP Annals-Manufacturing Technology*, 58(1):197–200, 2009.
- [63] O Huber, J Nickel, and G Kuhn. On the decomposition of the j-integral for 3d crack problems. *International Journal of Fracture*, 64(4):339–348, 1993.
- [64] Thomas JR Hughes, John A Cottrell, and Yuri Bazilevs. Isogeometric analysis: CAD, finite elements, NURBS, exact geometry and mesh refinement. *Computer methods in applied mechanics and engineering*, 194(39):4135–4195, 2005.
- [65] C-Y Hui, A Jagota, SJ Bennison, and JD Londono. Crack blunting and the strength of soft elastic solids. In *Proceedings of the Royal Society of London A: Mathematical, Physical and Engineering Sciences*, volume 459, pages 1489–1516. The Royal Society, 2003.
- [66] JW Hutchinson. Plastic stress and strain fields at a crack tip. *Journal of the Mechanics and Physics of Solids*, 16(5):337–342, 1968.

- [67] CG Hwang, PA Wawrzynek, AK Tayebi, and AR Ingraffea. On the virtual crack extension method for calculation of the rates of energy release rate. *Engineering Fracture Mechanics*, 59(4):521–542, 1998.
- [68] J Ibbett, B Tafazzolimoghaddam, H Hernandez Delgadillo, and JL Curiel-Sosa. What triggers a microcrack in printed engineering parts produced by selective laser sintering on the first place? *Materials & Design*, 88:588–597, 2015.
- [69] G. R. Irwin. Analysis of stresses and strains near the end of a crack traversing a plate. *Journal of Applied Mechanics*, 24:361–364, 1957.
- [70] George R Irwin. Fracture. In *Elasticity and Plasticity/Elastizität und Plastizität*, pages 551–590. Springer, 1958.
- [71] GR Irwin. Plastic zone near a crack and fracture toughness. 1997.
- [72] R.M. Jones. *Mechanics of Composite Materials*. Taylor & Francis, 1999.
- [73] L. Kachanov. *Introduction to continuum damage mechanics*. Mechanics of Elastic Stability. Springer Netherlands, 1986.
- [74] L. M. Kachanov. Time of the rupture process under creep conditions, izy akad. *Nank SSR Otd Tech Nauk*, 8:26–31, 1958.
- [75] Luiz F. Kawashita and Stephen R. Hallett. A crack tip tracking algorithm for cohesive interface element analysis of fatigue delamination propagation in composite materials. *International Journal of Solids and Structures*, 49(21):2898 – 2913, 2012.
- [76] M Kenane and ML Benzeggagh. Mixed-mode delamination fracture toughness of unidirectional glass/epoxy composites under fatigue loading. *Composites Science and Technology*, 57(5):597–605, 1997.
- [77] Amir R Khoei. *Extended finite element method: theory and applications*. John Wiley & Sons, 2014.
- [78] JungHoon Kim, Goangseup Zi, Son-Nguyen Van, MinChul Jeong, JungSik Kong, and Minsung Kim. Fatigue life prediction of multiple site damage based

- on probabilistic equivalent initial flaw model. *Structural Engineering and Mechanics*, 38(4):443, 2011.
- [79] László P. Kollár and George S. Springer. *Mechanics of Composite Structures*. Cambridge University Press, 2003.
- [80] Ronald Krueger. Virtual crack closure technique: history, approach, and applications. *Applied Mechanics Reviews*, 57(2):109–143, 2004.
- [81] J. Lemaitre and R. Desmorat. *Engineering Damage Mechanics: Ductile, Creep, Fatigue and Brittle Failures*. Springer Berlin Heidelberg, 2005.
- [82] Jean Lemaitre and Jean-Louis Chaboche. *Mechanics of solid materials*. Cambridge university press, 1994.
- [83] Jean Lemaitre and Rodrigue Desmorat. *Engineering damage mechanics: ductile, creep, fatigue and brittle failures*. Springer Science & Business Media, 2005.
- [84] Fang Zhong Li, C Fong Shih, and A Needleman. A comparison of methods for calculating energy release rates. *Engineering Fracture Mechanics*, 21(2):405–421, 1985.
- [85] H Li and H Yuan. Cohesive zone modelling of low cycle fatigue cracks in cracked and notched specimens. *Fatigue & Fracture of Engineering Materials & Structures*, 36(12):1246–1257, 2013.
- [86] Szu-Hui Lim and Shuguang Li. Energy release rates for transverse cracking and delaminations induced by transverse cracks in laminated composites. *Composites Part A: Applied Science and Manufacturing*, 36(11):1467–1476, 2005.
- [87] Won-Kyun Lim, Seung-Yong Choi, and Bhavani V Sankar. Biaxial load effects on crack extension in anisotropic solids. *Engineering Fracture Mechanics*, 68(4):403–416, 2001.
- [88] CE Majewski, H Zarringhalam, and N Hopkinson. Effects of degree of particle melt and crystallinity in sls nylon-12 parts. In *19th Solid Freeform Fabrication Symposium*, 2008.

- [89] Stefano Mariani and Umberto Perego. Extended finite element method for quasi-brittle fracture. *International Journal for numerical methods in engineering*, 58(1):103–126, 2003.
- [90] F.L. Matthews. *Finite Element Modelling of Composite Materials and Structures*. Taylor & Francis, 2000.
- [91] Jens M Melenk and Ivo Babuška. The partition of unity finite element method: basic theory and applications. *Computer methods in applied mechanics and engineering*, 139(1-4):289–314, 1996.
- [92] Julia Mergheim, Ellen Kuhl, and Paul Steinmann. A finite element method for the computational modelling of cohesive cracks. *International Journal for Numerical Methods in Engineering*, 63(2):276–289, 2005.
- [93] Nicolas Moës and Ted Belytschko. Extended finite element method for cohesive crack growth. *Engineering fracture mechanics*, 69(7):813–833, 2002.
- [94] Nicolas Moës, Mathieu Cloirec, Patrice Cartraud, and J-F Remacle. A computational approach to handle complex microstructure geometries. *Computer methods in applied mechanics and engineering*, 192(28):3163–3177, 2003.
- [95] S. Mohammadi. *XFEM Fracture Analysis of Composites*. Wiley, 2012.
- [96] Soheil Mohammadi. *Extended finite element method: for fracture analysis of structures*. John Wiley & Sons, 2008.
- [97] B Moran and CF Shih. Crack tip and associated domain integrals from momentum and energy balance. *Engineering fracture mechanics*, 27(6):615–642, 1987.
- [98] A Mubashar, IA Ashcroft, and AD Crocombe. Modelling damage and failure in adhesive joints using a combined xfem-cohesive element methodology. *The Journal of Adhesion*, 90(8):682–697, 2014.
- [99] JJ Munoz, U Galvanetto, and P Robinson. On the numerical simulation of fatigue driven delamination with interface elements. *International journal of fatigue*, 28(10):1136–1146, 2006.

- [100] N. I Muskhelishvili. *Some basic problems of the mathematical theory of elasticity : fundamental equations, plane theory of elasticity, torsion and bending*. Noordhoff, Groningen, 4th corrected and augmented ed. [i.e. 2nd English ed., based on the 4th Russian ed.]. edition, 1963.
- [101] J Tinsley Oden, Ted Belytschko, Ivo Babuška, and TJR Hughes. Research directions in computational mechanics. *Computer Methods in Applied Mechanics and Engineering*, 192(7):913–922, 2003.
- [102] Stanley Osher and James A Sethian. Fronts propagating with curvature-dependent speed: algorithms based on Hamilton-Jacobi formulations. *Journal of computational physics*, 79(1):12–49, 1988.
- [103] M. Pais. MATLAB Extended Finite Element (MXFEM) Code v1.3, www.matthewpais.com, 2011.
- [104] F París, A Blázquez, LN McCartney, and V Mantič. Characterization and evolution of matrix and interface related damage in [0/90]s laminates under tension. Part I: Numerical predictions. *Composites Science and Technology*, 70(7):1168–1175, 2010.
- [105] Paul C Paris, Mario P Gomez, and William E Anderson. A rational analytic theory of fatigue. *The trend in engineering*, 13(1):9–14, 1961.
- [106] Paul Croce Paris and Fazil Erdogan. A critical analysis of crack propagation laws. ASME, 1963.
- [107] RHJ Peerlings, WAM Brekelmans, R De Borst, and MGD Geers. Gradient-enhanced damage modelling of high-cycle fatigue. *International Journal for Numerical Methods in Engineering*, 49(12):1547–1569, 2000.
- [108] TP Philippidis and VA Passipoularidis. Residual strength after fatigue in composites: Theory vs. experiment. *International Journal of Fatigue*, 29(12):2104–2116, 2007.
- [109] A. Pironi and F. Moroni. A progressive damage model for the prediction of fatigue crack growth in bonded joints. *The Journal of Adhesion*, 86(5-6):501–521, 2010.

- [110] J Planas and M Elices. Asymptotic analysis of a cohesive crack: 1. theoretical background. *International Journal of Fracture*, 55(2):153–177, 1992.
- [111] IS Raju, JH Crews, and MA Aminpour. Convergence of strain energy release rate components for edge-delaminated composite laminates. *Engineering fracture mechanics*, 30(3):383–396, 1988.
- [112] IS Raju and KN Shivakumar. An equivalent domain integral method in the two-dimensional analysis of mixed mode crack problems. *Engineering Fracture Mechanics*, 37(4):707–725, 1990.
- [113] Kenneth L Reifsnider. *Fatigue of composite materials*, volume 4. Elsevier, 2012.
- [114] JJC Remmers, Rene de Borst, and A Needleman. A cohesive segments method for the simulation of crack growth. *Computational mechanics*, 31(1-2):69–77, 2003.
- [115] J.R. Rice. A path independent integral and the approximate analysis of strain concentration by notches and cracks. *Journal of Applied Mechanics*, 35(2), 1968.
- [116] J.R. Rice. A path independent integral and the approximate analysis of strain concentration by notches and cracks. *Journal of applied mechanics*, 35(2):379–386, 1968.
- [117] J.R. Rice. *The mechanics of earthquake rupture*. Division of Engineering, Brown University, 1979.
- [118] J.R. Rice and G.F. Rosengren. Plane strain deformation near a crack tip in a power-law hardening material. 16(1):1–12, 1968.
- [119] J.R. Rice and George C Sih. Plane problems of cracks in dissimilar media. *Journal of Applied Mechanics*, 32(2):418–423, 1965.
- [120] Paul Robinson, Ugo Galvanetto, Davide Tumino, Giordano Bellucci, and David Violeau. Numerical simulation of fatigue-driven delamination using interface elements. *International Journal for Numerical Methods in Engineering*, 63(13):1824–1848, 2005.

- [121] KL Roe and Th Siegmund. An irreversible cohesive zone model for interface fatigue crack growth simulation. *Engineering fracture mechanics*, 70(2):209–232, 2003.
- [122] M.H. Sadd. *Elasticity: Theory, Applications, and Numerics*. Elsevier Science, 2010.
- [123] CF Shih and RJ Asaro. Elastic-plastic analysis of cracks on bimaterial interfaces: Part I - small scale yielding. *Journal of Applied Mechanics*, 55(2):299–316, 1988.
- [124] CF Shih, B Moran, and T Nakamura. Energy release rate along a three-dimensional crack front in a thermally stressed body. *International Journal of fracture*, 30(2):79–102, 1986.
- [125] G. C. Sih, P. C. Paris, and G. R. Irwin. On cracks in rectilinearly anisotropic bodies. *International Journal of Fracture Mechanics*, 1(3):189–203, Sep 1965.
- [126] JC Simo and JW Ju. Strain-and stress-based continuum damage models. Formulation. *Mathematical and Computer Modelling*, 12(3):378, 1989.
- [127] IV Singh, BK Mishra, S Bhattacharya, and RU Patil. The numerical simulation of fatigue crack growth using extended finite element method. *International Journal of Fatigue*, 36(1):109–119, 2012.
- [128] MD Snyder and TA Cruse. Boundary-integral equation analysis of cracked anisotropic plates. *International Journal of Fracture*, 11(2):315–328, 1975.
- [129] P Sollero and MH Aliabadi. Fracture mechanics analysis of anisotropic plates by the boundary element method. *International Journal of Fracture*, 64(4):269–284, 1993.
- [130] J.L. Curiel Sosa, N. Petrinic, and J. Wiegand. A three-dimensional progressive damage model for fibre-composite materials. *Mechanics Research Communications*, 35(4):219 – 221, 2008.

- [131] N= Sukumar, D. L. Chopp, N. Moës, and T. Belytschko. Modeling holes and inclusions by level sets in the extended finite-element method. *Computer methods in applied mechanics and engineering*, 190(46):6183–6200, 2001.
- [132] N Sukumar, DL Chopp, and B Moran. Extended finite element method and fast marching method for three-dimensional fatigue crack propagation. *Engineering Fracture Mechanics*, 70(1):29–48, 2003.
- [133] N Sukumar, ZY Huang, J-H Prévost, and Z Suo. Partition of unity enrichment for bimaterial interface cracks. *International Journal for Numerical Methods in Engineering*, 59(8):1075–1102, 2004.
- [134] 3D Systems. Data form duraform PA and GF, materials for SLS systems *website*. 2013.
- [135] A Turon, Pedro Ponces Camanho, J Costa, and CG Dávila. A damage model for the simulation of delamination in advanced composites under variable-mode loading. *Mechanics of Materials*, 38(11):1072–1089, 2006.
- [136] A Turon, J Costa, PP Camanho, and CG Dávila. Simulation of delamination in composites under high-cycle fatigue. *Composites Part A: applied science and manufacturing*, 38(11):2270–2282, 2007.
- [137] A Turon, Carlos G Davila, Pedro Ponces Camanho, and J Costa. An engineering solution for mesh size effects in the simulation of delamination using cohesive zone models. *Engineering fracture mechanics*, 74(10):1665–1682, 2007.
- [138] Viggo Tvergaard and John W Hutchinson. The relation between crack growth resistance and fracture process parameters in elastic-plastic solids. *Journal of the Mechanics and Physics of Solids*, 40(6):1377–1397, 1992.
- [139] I Varfolomeev, M Burdack, S Moroz, D Siegele, and K Kadau. Fatigue crack growth rates and paths in two planar specimens under mixed mode loading. *International Journal of Fatigue*, 58:12–19, 2014.
- [140] J.R. Vinson and R.L. Sierakowski. *The Behavior of Structures Composed of Composite Materials*. Solid Mechanics and Its Applications. Springer Netherlands, 2011.

- [141] MM Abdel Wahab, IA Ashcroft, AD Crocombe, and PA Smith. Finite element prediction of fatigue crack propagation lifetime in composite bonded joints. *Composites Part A: Applied Science and Manufacturing*, 35(2):213–222, 2004.
- [142] J Wang and BL Karihaloo. Matrix crack-induced delamination in composite laminates under transverse loading. *Composite structures*, 38(1-4):661–666, 1997.
- [143] GN Wells and LJ Sluys. A new method for modelling cohesive cracks using finite elements. *International Journal for Numerical Methods in Engineering*, 50(12):2667–2682, 2001.
- [144] Harold M Westergaard. Bearing pressures and cracks. *Journal of applied mechanics*, 6(2):A49–A53, 1939.
- [145] ML Williams. The stresses around a fault or crack in dissimilar media. *Bulletin of the seismological society of America*, 49(2):199–204, 1959.
- [146] De Xie, Anthony M Waas, Khaled W Shahwan, Jessica A Schroeder, and Raymond G Boeman. Computation of energy release rates for kinking cracks based on virtual crack closure technique. *Computer Modeling in Engineering & Sciences*, 6(6):515–524, 2004.
- [147] X-P Xu and A Needleman. Void nucleation by inclusion debonding in a crystal matrix. *Modelling and Simulation in Materials Science and Engineering*, 1(2):111, 1993.
- [148] Yangjian Xu and Huang Yuan. Computational analysis of mixed-mode fatigue crack growth in quasi-brittle materials using extended finite element methods. *Engineering Fracture Mechanics*, 76(2):165–181, 2009.
- [149] Yangjian Xu and Huang Yuan. On damage accumulations in the cyclic cohesive zone model for XFEM analysis of mixed-mode fatigue crack growth. *Computational Materials Science*, 46(3):579–585, 2009.
- [150] Qingda Yang and Brian Cox. Cohesive models for damage evolution in laminated composites. *International Journal of Fracture*, 133(2):107–137, 2005.

- [151] Chang Ye, Jay Shi, and Gary J Cheng. An extended finite element method (XFEM) study on the effect of reinforcing particles on the crack propagation behavior in a metal–matrix composite. *International Journal of Fatigue*, 44:151–156, 2012.
- [152] Arash Zamani, Robert Gracie, and M Reza Eslami. Cohesive and non-cohesive fracture by higher-order enrichment of XFEM. *International Journal for Numerical Methods in Engineering*, 90(4):452–483, 2012.
- [153] Hadi Zarringhalam. *Investigation into crystallinity and degree of particle melt in selective laser sintering*. PhD thesis, © Hadi Zarringhalam, 2007.
- [154] Junqian Zhang, Jinghong Fan, and KP Herrmann. Delaminations induced by constrained transverse cracking in symmetric composite laminates. *International Journal of Solids and Structures*, 36(6):813–846, 1999.
- [155] Goangseup Zi and Ted Belytschko. New crack-tip elements for xfem and applications to cohesive cracks. *International Journal for Numerical Methods in Engineering*, 57(15):2221–2240, 2003.
- [156] Z Zou, SR Reid, S Li, and PD Soden. General expressions for energy–release rates for delamination in composite laminates. In *Proceedings of the Royal Society of London A: Mathematical, Physical and Engineering Sciences*, volume 458, pages 645–667. The Royal Society, 2002.